Search for events with two displaced vertices from pair-produced neutral long-lived particles decaying to hadronic jets in the muon spectrometer of the ATLAS detector with full Run 2 data

---

Audrey Kvam

A dissertation submitted in partial
fulfillment of the requirements for
the degree of
Doctor of Philosophy

University of Washington

March 2022

Reading Committee:

Henry Lubatti, Chair

Stephen Sharpe

Gordon Watts

Program Authorized to Offer Degree:

Physics

University of Washington

Abstract

Search for events with two displaced vertices from pair-produced neutral long-lived particles decaying to hadronic jets in the muon spectrometer of the ATLAS detector with full Run 2 data

Audrey Kvam

Chair of the Supervisory Committee:
Henry Lubatti
Department of Physics

This analysis is a search for events with two displaced vertices reconstructed from the decay of pair-produced neutral, weakly-interacting, long-lived particles using the muon spectrometer of the ATLAS detector. The search uses a model-independent strategy, and employs a custom trigger for reconstructing displaced hadronic jets in the muon spectrometer with 139 fb^{-1} of pp collision data at $\sqrt{s} = 13$ TeV collected in Run 2 at the LHC. The results are interpreted in terms of a Higgs scalar portal model, which probes the existence of a hidden sector that weakly couples to the Standard Model. The search observed 0 events in the signal region, which is compatible with the expected background of 0.32 ± 0.05 events. Limits were set on long-lived particle lifetime for all simulated signal mass points. For the Higgs boson with a mass of 125 GeV, the analysis reports the first exclusion limits for branching fractions into neutral long-lived particles below 0.1%, while branching fractions above 10% are excluded at 95% confidence level for long-lived particle proper lifetimes ranging from 4 cm to 72.4 m. In addition, the analysis presents the first results for the decay of long-lived particles into $t\bar{t}$ in the ATLAS muon spectrometer.

To my parents

Acknowledgments

It has been wonderful to take time to consider and illuminate all the people who have made this achievement possible, both in my professional network and my personal support system.

The first and most obvious acknowledgments to make are that of my advisor, Henry Lubatti, and postdoc, Cristiano Alpigiani. Thank you so much for all of the help, support, and advice given over the years to mould me into a functioning physicist. I sincerely hope that our collaboration does not end here!

Another crucial acknowledgment goes to Catherine Provost for repeatedly saving me from myself and my inability to keep track of deadlines, and also for the steady supply of chocolate. I don't think I would've made it past the General Exam without you.

A huge thank you to my parents – for your full confidence, encouragement, and support from the very beginning, and for all of the opportunities you gave me that led me here.

Molly and Rachel – I am endlessly grateful that our friendship is a constant while everything else changes. I still hope we can form a commune in our retirement years.

Lesya – I feel so lucky that we've been at CERN for the exact same length of time, and have been friends for all of it. You give not only the best and wisest advice, but also the wittiest.

Mally – it is completely hilarious to me that we did not become friends in the 4 years we spent in Tacoma, and only got our act together in Switzerland. Glad we finally got it right! You have truly kept me sane for the past few years and I can never thank you enough.

Vivan and Sana – world's all-time best flatmates. Maybe I could've finished my PhD sooner if you two hadn't made coming home so fun! Thank you for all of the laughter, adventures, and amazing food.

A special shout-out and thank you to the friends who came to see me in Europe – Rachel, Becca, Jolene, and Josie – it meant so much to me. (Sorry again, Josie, for being sick the entire time you were here. Please come back!)

Finally, a heartfelt thank you to all my friends in Seattle, Geneva, and around the world for all the hikes, climbs, lake jumps, via ferratas, movie marathons, drinks, late night talks, and holidays – there are too many people to acknowledge everyone by name, but hopefully you all know who you are. Looking forward to more of all of it!

Contents

List of Figures

List of Tables

Chapter 1

Introduction

The quest to describe all natural phenomena with logical rules and mathematical structure has undergone a series of revolutions.

We know of various theories proposed, experiments performed, discoveries made by particularly curious individuals (Archimedes, Aristotle, Galileo, to name a few) since the dawn of recorded history, but the real kick-off for physics as we think of it in the modern day came from Isaac Newton in the late 1600s. Newton lived through the chaos, confusion, and forced isolation of a plague (which today's readers will surely identify with) and he took advantage of this time to invent calculus and the universal law of gravitation (which today's readers will probably *not* identify with). Though he authored a variety of seminal works, he is perhaps most famous today for his laws of motion, which consist of three assertions – (i) an object at rest will remain at rest unless acted on by an outside force, (ii) an object's acceleration is proportional to the net force applied on it, and (iii) every action has an equal and opposite reaction. The assertions are simple and concise, but so brilliant that they have remained a foundation of physical understanding up to the present day. Modern physics has moved beyond these laws, but only in the sense of recognizing their limitations rather than discarding them altogether. Newton dominated the landscape of physics so thoroughly, for so long, that in 1900 – still working within the Newtonian framework – Lord Kelvin allegedly commented that "There is nothing new to be discovered in physics now. All that remains is more and more precise measurement". The universe seems to have a sense of humor, because Max Planck's paper "On the Theory of the Energy Distribution Law of the Normal Spectrum," published in December of that same year, is commonly heralded as the advent of the next scientific revolution: quantum mechanics.

The development of quantum theory spanned decades. The work of Max Planck, Albert Einstein, Arthur Compton and others showed that certain fundamental values that were previously thought to be continuous, for example energy, are in fact discretized or *quantized*. It follows that light is not only a wave, but also a particle; Louis de Broglie then pushed the argument further and showed that particles are also waves. Werner Heisenberg and Erwin Schrödinger, working independently, formalized the mathematics of this new conception of the world.

The implications of a quantized universe are confusing and unintuitive, even to those who proposed it. Schrödinger famously described the quantum phenomena of superpositions in terms of a cat in a box that has a 50% chance of dying. Until you look inside the box, the cat is both alive and dead because both states exist simultaneously (in a superposition) until you force reality, through your observation, to collapse into one or the other. This goes against all understanding of how the world operates, and Schrödinger himself called the case "ridiculous." However, quantum superpositions have been proven to be quite real (though the reality of a cat being truly alive and dead simultaneously remains up to interpretation). Einstein was also troubled by the logical conclusions of some aspects of quantum mechanics, in particular that it is inherently a probabilistic theory. Even if all information about the initial system is known, experimental outcomes cannot be exactly predicted — instead, the statistical probability of an outcome occurring is calculated. This is unlike the deterministic Newtonian universe, where a known initial state would lead to a single, calculable final state. Einstein protested this by famously declaring that "God does not play dice with the universe." On the other hand, some argue that a probabilistic universe is what makes the concept of free will possible. Debates such as these – Can something like death rely on external observation? Can free will exist if and only if the universe is probabilistic? – have no easy answers through logical argument or scientific experimentation. In this sense, quantum mechanics has represented not only a scientific revolution but a philosophical one as well.

Despite the challenges of believing in such a wild theory, its predictive power is undeniable, and it has been thoroughly accepted by the scientific community. And while quantum mechanics was reforming our understanding of the universe at a subatomic scale, Einstein initiated another scientific revolution at the planetary scale with his theory of special relativity, followed closely by general relativity. Relativity is the idea that all reference frames are equally valid, and the laws of physics must only be adjusted from one frame to another according to the relative acceleration between them. It expanded our understanding of space and time from separate, fixed entities providing a passive backdrop of the universe into a dynamic *spacetime* that directly gives rise to gravity where it is warped by the presence of massive objects.

The twentieth century saw these two revolutions settling into place as the new foundation of humankind's physical knowledge, and their details being filled in. The union of quantum mechanics and special relativity created quantum field theory, which provides the mathematical structure for the Standard Model – the theoretical model that summarizes all known elementary particles and their interactions (other than gravitational). Elementary and composite particles were discovered by the handful, sometimes following from theoretical prediction and sometimes being observed before the theory was in place. The weak and strong forces were proposed along with the Higgs field, and all the puzzle pieces seemed to be falling into place. With the discovery of the Higgs boson in 2012, the Standard Model was considered complete.

When considering the history of physics, a pattern becomes clear: a theory is proposed, and is supported by evidence. Much effort goes into filling gaps, extending previous work, and laying out all the implications that this new theory provides. At some point the limitations and contradictions inherent to the theory become clear. A new or revised theory is required, and the procedure repeats. This is, of course, simply the scientific method on a grand scale.

We have found several limitations in the Standard Model. A new theory is required to extend it, to explain the phenomena that the Standard Model cannot. Dozens of theories have been proposed, and we are in the process of testing them to see which ones are supported by experimental evidence. So far, however, we have not found compelling evidence to support any particular proposed theory. So far, theories are only being constrained or ruled out. The analysis described in this thesis adds to this suite of constraints.

What form will our next scientific revolution take? The quest continues.

Chapter 2

Theory

Particle physics is a field that deals with extremely small things moving extremely fast: the building blocks of the universe moving with velocities approaching the speed of light. This microscopic, relativistic realm is sometimes more easily understood when *natural units* are employed, where $c = h = 1$. This means that mass, momentum, and energy all have units of GeV. It also means that velocity v is dimensionless, where massive particles have $0 \leq v < 1$ and massless particles have $v = 1$.

2.1 The Standard Model

The Standard Model (SM) of particle physics describes all known elementary particles in the universe and three forces – electromagnetic, weak, and strong – that govern their interactions. It is important to note that there is a fourth force left off of this list, though it is arguably the most famous: gravity. The SM does not provide any description of gravitational interactions; this is instead provided by Einstein's general theory of relativity. Theorists aspire to combine general relativity and the Standard Model into one unified theory, but so far none have been wholly successful.

There are 17 elementary particles in the SM, as shown in fig. 2.1. These can be subdivided into leptons, quarks, gauge bosons, and the Higgs boson. The leptons and quarks are *fermions*, meaning they have half-integer spin, and they are the building blocks of all matter in our universe. *Bosons* are particles with integer spin, and they act as force carriers mediating interactions between particles. While all elementary fermions have spin $\frac{1}{2}$, quarks can combine to form other, composite particles. Composite particles formed from an even number of quarks are called *mesons*, and their overall spin is an integer (0,1,2...), making them bosons. Particles formed from an odd number of quarks are called *baryons*, and their total spin is a half-integer $\left(\frac{1}{2}, \frac{3}{2}, \frac{5}{2}...\right)$, making them fermions.

All particles also have an associated *antiparticle*, which has the same spin but opposite charge. The antiparticle is usually denoted simply by putting "anti-" in front of the usual particle name; for example, the antiparticle of a muon is an antimuon. The exception is the antiparticle of an electron, which is traditionally referred to as a positron. Some particles, like the photon and the Z^0 boson, are their own antiparticle.

There are 6 leptons divided into three generations, each one comprised of a particle and its corresponding neutrino. These are arranged in terms of increasing mass of the charged particle; therefore, the electron and electron neutrino are the first generation, the muon and muon neutrino are the second, and the tau particle and tau neutrino are the third. Electrons, muons, and taus all have an electric charge of $1.6 \times 10^{-19}\,\mathrm{C} = 1e$. Neutrinos, true to their name, are electrically neutral.

There are 6 types, or *flavors*, of quarks: up, down, charm, strange, top, and bottom (or beauty). Like the leptons, these are organized into three generations of matter, ordered in terms of increasing mass. The up and down quarks are the lightest, belonging to the first generation, and as such are the only quarks that are generally stable (though they can decay into each other). They are a key component of all atoms in the universe, as they are the valence quarks in protons (uud) and neutrons (udd). The second generation is composed of the charm and strange quarks, and the top and bottom quarks make up the third. Each generation has one quark with a charge of $\frac{2}{3}e$ (the up quark, in the first generation) and one with $-\frac{1}{3}e$ (the down quark, in the first generation). Charm and top quarks will sometimes be referred to as "up-like" as they are the positively-charged quarks of their generations; similarly, strange and bottom quarks are sometimes called "down-like". Quarks also have *color charge*. This is not a statement on what a quark looks like, or what kind of electromagnetic wavelengths quarks absorb and emit, but rather a fundamental property of the particle. It is confusingly named, as Richard Feynman pointed out rather scathingly in his book *QED: The Strange Theory of Light and Matter*: "The idiot physicists, unable to come up with any wonderful Greek words anymore, call this type of polarization by the unfortunate name of 'color,' which has nothing to do with color in the normal sense." Regardless, quarks can have red, green, or blue color charge while antiquarks can be antired, antigreen, or antiblue. The study of color-charged particles is called *quantum chromodynamics*, or QCD.

There is a phenomenon in QCD called *color confinement*, which means that particles can only exist in a colorless state. This means that a quark can never be found on its own, but can only be observed as a meson (where, for example, a red quark is in a bound state with an antired antiquark, leading to an overall colorless composite particle) or a baryon (where, for example, a red quark is in a bound state with a blue quark and a green quark, again leading to an overall colorless particle). Most mesons and baryons have two and three quarks respectively, but some other, exotic states can also exist as long as they are colorless – for example tetraquarks ($qq\overline{q}\overline{q}$) and pentaquarks ($q\overline{q}q\overline{q}q$). Color confinement is due to the nature of the strong force; as quarks are separated, the strong force between them actually increases linearly with distance (as opposed to a force like electromagnetism, which decreases as the inverse of distance squared). As a result, at some point it becomes energetically favorable to create a quark-antiquark pair from the vacuum rather than separating the two original quarks any farther, leading to two resultant $q\overline{q}$ pairs.

As stated before, the elementary particles that are not fermions are instead *bosons*, meaning they have integer spin, and they are force carriers that mediate the interactions between particles. Photons, usually represented by γ, mediate the electromagnetic force. They are massless, chargeless, and colorless. Gluons, g, mediate the strong force and are massless and chargeless like the photon, however they carry both color and anticolor charge. Three particles mediate the weak force, all of which are massive: two W bosons, which are antiparticles of each other, and the Z boson. The Z boson is neutral while one W boson has $+1e$ charge and the other has $-1e$ charge. All of these mediators – γ, g, $W^{\pm}$, and Z – are vector bosons, meaning they have spin 1. The final particle contained in the SM is the Higgs boson: a particle with no electric charge, color charge, or spin (making it a scalar boson). It is massive and extremely unstable, decaying with an average lifetime on the order of 10^{-22} s.

So far this has been a description of the elementary particles, with no insight as to their mathematical formulation within the SM or the implications of their properties. This is an immensely complex topic and a full description requires the length and detail of a textbook; an extremely abridged version will be given here, and the reader is encouraged to fill in the gaps elsewhere [1, 2].

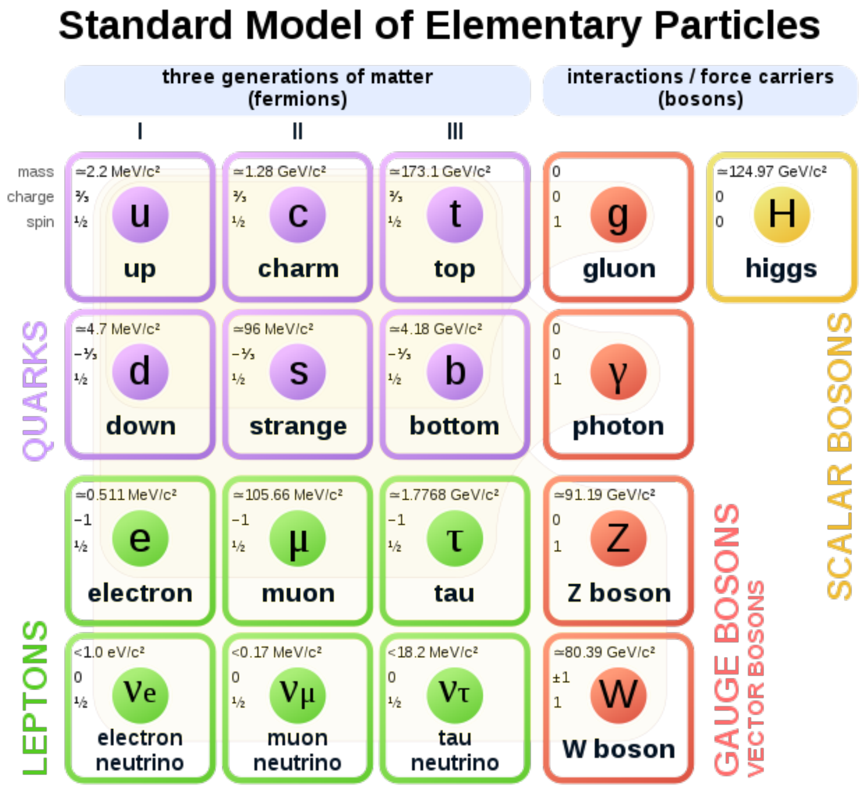

Figure 2.1: The elementary particles in the SM.

The SM is a *gauge quantum field theory.* A quantum field theory describes the interactions of fields with matter while incorporating the principles of quantum mechanics and special relativity (note it only incorporates *special* relativity; as mentioned before, the SM cannot yet be reconciled with *general* relativity). Gauge refers to the fact that the Lagrangian of the theory remains invariant under a particular set of transformations, called a symmetry group. The symmetry group, or gauge group, of the SM is

$$G = SU(3)_C \times SU(2)_L \times U(1)_Y \tag{2.1}$$

where $SU(n)$ is the special unitary group of order n and $U(1)$ is the unitary group of order 1. $SU(3)_C$ denotes the three-fold symmetry of the strong force and its color field, where the subscript C stands for color. Meanwhile $SU(2)_L \times U(1)_Y$ is the symmetry of the electroweak interaction, since at high energy (much greater than the mass scale of the W and Z bosons) electromagnetism and the weak interaction can be unified into a single mathematical description. All terms that enter into the SM Lagrangian must be invariant

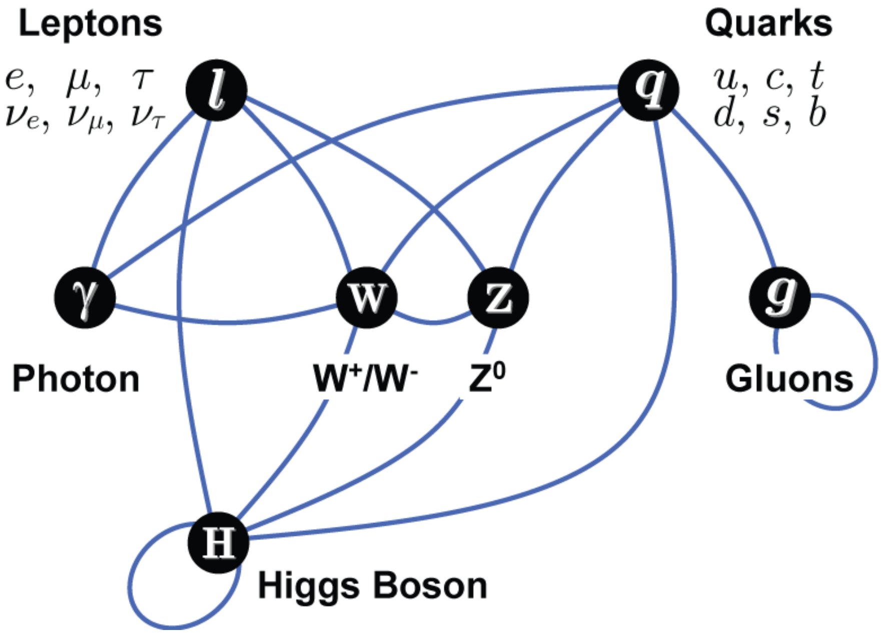

Figure 2.2: Diagram linking the elementary particles that are able to interact with each other within the SM. Note that gluons and the Higgs boson self-interact.

under these symmetry groups in order to preserve the overall invariance.

The unification of electromagnetism and the weak force is very non-intuitive, since they are expressed differently at low energies – this is clear to see from the fact that unlike the photon, the W and Z bosons have mass. The underlying reason for the W and Z bosons to be massive was one of the main mysteries in particle physics in the 20th century; it is not so simple as to add mass terms into the Lagrangian, because those terms would violate gauge invariance. How, then, do the gauge bosons gain mass?

The answer comes in the form of the Higgs boson. At low energies the Higgs potential takes the shape of a "Mexican hat," meaning the minimum of the potential corresponds to a non-zero vacuum expectation value for the Higgs field (which turns out to be 246 GeV). This breaks the symmetry of the system, known as *spontaneous symmetry breaking*, and is illustrated in fig. 2.3. All gauge bosons that interact with the Higgs boson gain mass as a consequence of this broken symmetry, which is referred to as the Higgs mechanism.

2.2 Open Questions in Particle Physics

The SM is self-consistent and has excellent predictive power, but it is not able to explain all physical phenomena, and there are many open questions currently under investigation.

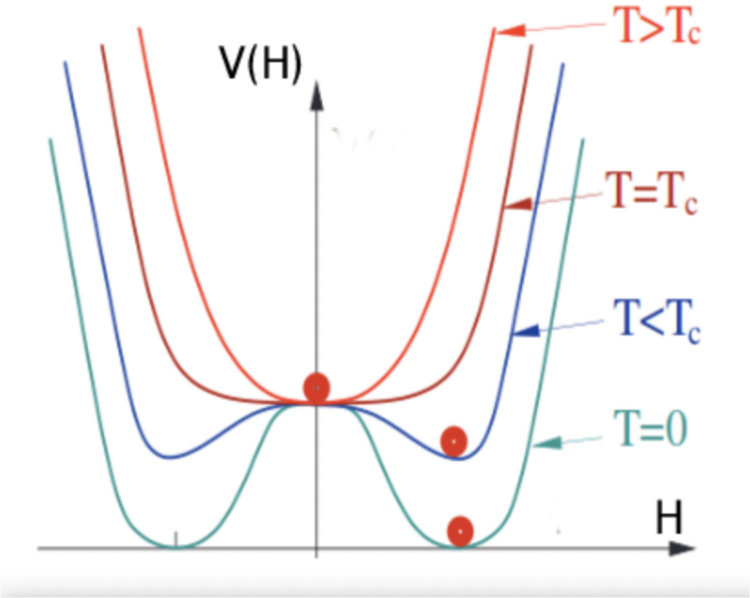

Figure 2.3: The Higgs potential at various energies, demonstrating how symmetry is broken as temperature T falls below the critical temperature T_C [3].

In some cases, the questions arise from suspected discrepancies between SM predictions and measured results. Combined measurements of the anomalous magnetic moment of the muon from Brookhaven and Fermilab currently show a 4.2σ deviation from the SM prediction [4]. The LHCb experiment has presented a deviation from SM predictions in the angular distribution of $B^0 \to K^{*0}\mu^+\mu^-$ decays, with 3.3σ significance [5]. While 5σ is the accepted threshold for claiming a discovery, these results strongly hint that the SM is not a perfect description of our universe. This does not necessarily mean that the SM is wrong in its formulation; more likely there is something it does not take into account.

In the cases just described, the SM offers a prediction that is close to experimental measurement. However, in other cases its prediction has a large discrepancy or no prediction is given at all. To list just a few examples:

- *The strong CP problem.* Charge symmetry implies that the physics of a system remains unchanged when a particle is replaced by its antiparticle (i.e. the charge is flipped), while parity symmetry implies the same for when spatial coordinates are inverted (i.e. the parity is flipped). Charge-parity (CP) symmetry implies that the physics is unchanged when both of these inversions are performed in combination. Experimental results seem to show that CP symmetry is conserved in QCD interactions, but the

SM offers no explanation for why this would be true – theoretically, CP violations are allowed, and it is a generally accepted rule of nature that anything that can happen will happen.

- *Matter-antimatter asymmetry.* It is not understood why there is significantly more matter in the universe than antimatter. An antimatter particle is, after all, fundamentally the same as its corresponding matter particle except that it has opposite charge. Why would the production of one be suppressed compared to the other? The Sakharov conditions outline three criteria that must be fulfilled in order for such an asymmetry to occur: 1) baryon number violation, 2) C and CP violation, and 3) interactions out of thermal equilibrium [6]. While the first two conditions are fulfilled by the SM, it was determined in the 1980s that any intuitive calculation falls short of the observed asymmetry by several orders of magnitude [7, 8].

- *Dark matter.* The velocity with which stars orbit the center of their galaxies does not conform to astrophysicists' predictions, which are based on the gravitational forces from all visible matter in the galaxy in question. There are two potential explanations for the observed discrepancy: either there is extra, non-visible matter present and its gravitational pull needs to be added into the calculation, or our theory of gravity is wrong. It is generally considered far more likely that the former is true, and there is some non-visible or "dark" matter in our universe waiting to be characterized. This is supported by observations of the Bullet Cluster [9], which was formed when two clusters of galaxies collided with high velocities. An image of this cluster is shown in fig. 2.4, where the pink color indicates where the visible matter is located (mostly in the form of hot gas) and the blue color shows where most of the mass is located according to gravitational lensing. The separation between the two can be clearly explained with the presence of dark matter: when the clusters collided, the visible matter was slowed down by a drag force that the dark matter did not experience, since it only interacts gravitationally. This phenomenon cannot, however, be explained with a modification to the current theory of gravity.

- *The hierarchy problem.* The hierarchy problem is the issue of why gravity is so much weaker than the other fundamental forces. The discrepancy can be seen when comparing the dimensionless coupling constants for each force, as shown in table 2.1. This

Figure 2.4: The Bullet Cluster. Image credit: X-ray: NASA/CXC/CfA/M.Markevitch et al.; Optical: NASA/STScI; Magellan/U.Arizona/D.Clowe et al.; Lensing Map: NASA/STScI; ESO WFI; Magellan/U.Arizona/D.Clowe et al.

Coupling constants		
Strong	α_S	1
Electromagnetic	α	$^1/_{137}$
Weak	α_W	10^{-6}
Gravity	α_g	10^{-39}

Table 2.1: Coupling constants for each of the fundamental forces.

raises the issue of "naturalness"; when the strength of one force is so remarkably different from the other three it feels instinctively unnatural, that is there must be some underlying reason for it to become such an outlier. The problem can also be formulated in a more mathematical way, concerning the mass of the Higgs boson. The mass term of the Higgs in the SM Lagrangian is subject to quantum corrections from interactions with virtual particles, primarily virtual top quarks, with momenta up to the scale of the Planck mass, $m_{\text{Planck}} = 1.22 \times 10^{19}$ GeV (which is the scale below which the SM is considered valid, because gravity becomes strong). Experimentally, however, we know that the mass of the Higgs boson is just 125 GeV. How can this be possible? Either the correction factors on the order of 10^{19} GeV almost perfectly cancel, which seems unnatural to the extreme, or there is a deeper explanation that we have thus far missed.

Many of the analyses performed at the LHC test theoretical models proposed to answer open questions like the ones posed above. One of the most famous of these models is supersymmetry, often called SUSY, which offers a neat solution to the hierarchy problem. It postulates that every SM boson has an associated fermion particle, called a superpartner, and every SM fermion has a boson superpartner. These superpartners would share all the same quantum numbers but differ by a half-integer in spin. In the context of the hierarchy problem, the quantum correction to the mass of the Higgs boson from one particle would be almost exactly canceled by the correction from that particle's superpartner.

A boson superpartner is indicated by adding an "s" to the fermion particle name – so the theoretical superpartner of an electron is called a "selectron" – and a fermion superpartner is indicated by adding "ino" as a suffix – the partner of a gluon is a "gluino". In its most basic formulation, the superpartners would have the same mass as their SM counterparts; however, this is clearly not the case in nature as they would have been observed already. Instead, any superpartner must have significantly higher mass so that it wouldn't be produced in any standard interaction on earth. Therefore, the LHC is a natural place to probe the existence of such particles. A spontaneously broken symmetry, analagous to that of the Higgs field, would explain the mass discrepancy.

The experiments at the LHC were designed primarily to find the Higgs boson and perform precision measurements on various SM processes, but also to search for evidence of new physics beyond the SM. SUSY is an elegant and compelling theoretical model, so it has dominated in directing BSM searches at the LHC for the past 10 years. Dozens of analyses have been performed searching for SUSY, but so far they have all turned up nothing. Enthusiasm for SUSY is waning, and physicists are beginning to shift their attention elsewhere. Since the energy frontier – i.e., probing higher masses – has been unsuccessful thus far, and extending to even higher energy would require a new machine, another idea has emerged: it's time to explore the lifetime frontier instead.

2.3 The Lifetime Frontier

Particles within the SM have a wide range of lifetimes, as represented in fig. 2.5. Some, like the electron, are stable and never decay. Proton decay has never been observed but is theoretically possible, and its half-life is measured to be greater than 1.67×10^{34} years (while the universe is about 10^{10} years old). Other particles decay so quickly that they can never be directly observed; the lifetimes of the Higgs boson and the Z boson are 1.56×10^{-22} s and 3×10^{-25} s respectively. Most lie somewhere between these two extremes. It is reasonable to assume, then, that BSM particles could have a similar variation in lifetimes.

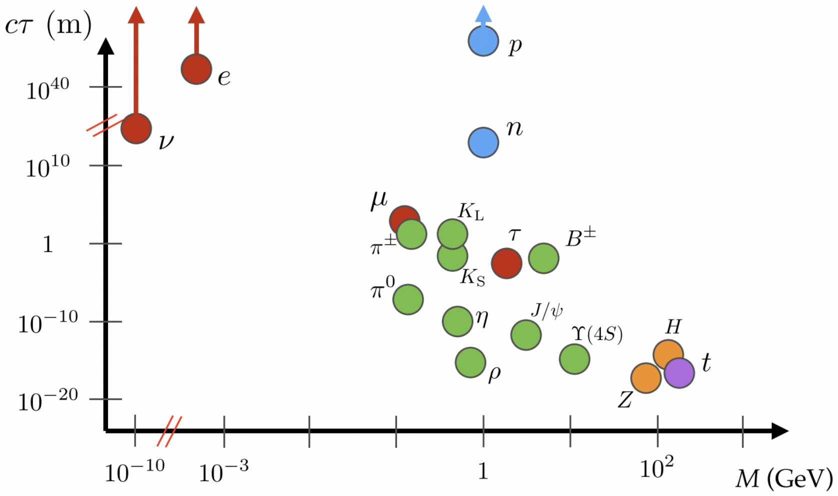

Figure 2.5: Lifetimes of various particles in the SM as a function of mass. Leptons are shown in red, baryons in blue, mesons in green, gauge bosons in orange, and quarks in purple [10].

If BSM particles had electric or color charge, they likely would have been observed already (unless their mass is so large that they still can't be produced at the LHC, or so light that they can effective hide in the middle of jets). But how can a neutral, colorless BSM particle produced in a *pp* collision be detected? One possibility is to search for missing transverse energy (MET), where the vector sum of all transverse momenta measured in the event is non-zero, indicating the existence of one or more invisible particles. Another possibility, more relevant for this thesis, is for it to decay back into observable SM particles. Traditional detectors are designed to reconstruct SM particles originating from the interaction point, but what if the BSM particle is *long-lived*, implying that it travels a macroscopic distance before decaying? In this kind of *displaced decay*, the observed SM decay products wouldn't be originating from the interaction point at all.

Neutral, weakly-coupled, long-lived particles (LLPs) arise in many proposed BSM theories, which can be non-exhaustively classified as supersymmetry-like [11, 12, 13], Higgs-portal [14, 15, 16, 17], gauge-mediated [18, 19], dark matter [20, 21], and heavy neutrino [22, 23] theories. Big Bang Nucleosynthesis (BBN) provides a general upper bound on lifetime for LLPs at

$0.1-1$ s, since the decay of LLPs during or after BBN would disrupt the process and modify known cosmological observables that are compatible with SM prediction. Other than that, the parameter space where long-lived particles could be hiding is largely unconstrained.

2.3.1 HSS Model

Some theoretical models known as hidden sector models extend the SM gauge group by a non-abelian group G_{HS}. SM particles would be uncharged under G_{HS}, but some new particles would be uncharged under the SM and charged under G_{HS}. The Higgs to two scalar model, or HSS model [24], is an example of such a theory and is used as a benchmark model for the analysis described in this thesis. An example of a Feynman diagram leading to the production and decay of LLPs in this model is shown in fig. 2.6.

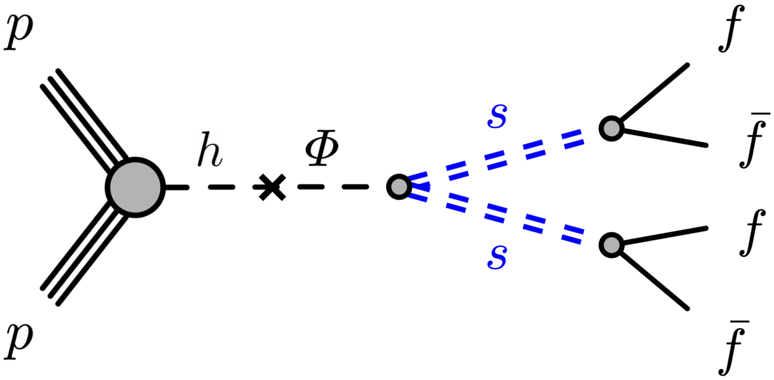

Figure 2.6: An example of a Feynman diagram leading to the production and decay of LLPs in the HSS model [24].

In the HSS model, the hidden sector couples very weakly to the SM. A Higgs boson produced in a pp collision can mix with some hidden-sector scalar field with the associated mediator Φ, which can be SM Higgs-like with a mass of 125 GeV or have lower or higher mass. The decay of Φ results in the pair-production of hidden-sector scalar or pseudoscalar particles s. The lifetime of s is unconstrained, so it can naturally be long-lived. These in turn are able to decay back into SM particles; the search described in this thesis focuses on $f\bar{f}$ final states where f is any SM fermion. While s is produced at the interaction point, its long lifetime means that these decay products can be highly displaced.

The details of s decay are highly model-dependent. For the HSS model as considered in this analysis, s is unstable because it weakly mixes with the Higgs boson and its branching ratios are therefore determined by the Higgs Yukawa coupling. Table 2.2 shows the branching ratios of each scalar decay channel in this analysis, rounded to the nearest percent. As m_s increases they approach the approximately constant values of 88% $b\bar{b}$, 8% $c\bar{c}$, and 4% $\tau^+\tau^-$. This holds true until a $t\bar{t}$ decay becomes kinematically available, at which point it becomes the dominant decay mode. This is clearly seen in the last row of table 2.2. In all cases, however, the s decay results in a hadronic jet of SM particles.

Table 2.2: Branching ratios of each scalar decay channel for the different mass scenarios considered in the analysis.

$\boldsymbol{m_s}$ [GeV]	$\boldsymbol{s \to \tau\bar{\tau}}$	$\boldsymbol{s \to c\bar{c}}$	$\boldsymbol{s \to b\bar{b}}$	$\boldsymbol{s \to t\bar{t}}$
5	25%	75%	-	-
15	7%	15%	78%	-
35	5%	9%	86%	-
50	4%	8%	87%	-
55	4%	8%	87%	-
100	4%	8%	87%	-
150	4%	8%	88%	-
275	4%	8%	88%	-
475	0%	0%	0%	100%

Chapter 3

The LHC and the ATLAS Experiment

3.1 The Large Hadron Collider

The Large Hadron Collider (LHC) is the largest particle accelerator in the world, and the most powerful with a maximum design center-of-mass energy of $\sqrt{s} = 14$ TeV. The LHC is housed in a circular tunnel measuring 26.7 km in circumference at the Conseil Européen pour la Recherche Nucléaire (CERN), or European Council for Nuclear Research. This is located near Geneva, Switzerland, straddling the border of Switzerland and France. The tunnel is underground, at a depth of between 50 and 175 m depending on the topography of the terrain above. Two beams of protons, traveling opposite directions, are accelerated to near the speed of light around the ring and made to collide at four distinct points, each known as an interaction point (IP). Each of the four main detectors at the LHC – ATLAS, CMS, LHCb, and ALICE – is based around a different IP with the goal of studying the physics processes that emerge from proton-proton (pp) and heavy ion collisions. Since heavy ion collisions are not relevant for this thesis, they will not be further elaborated on.

The tunnel currently being used for the LHC was originally built for the Large Electron-Positron (LEP) collider, which recorded data from electron-positron collisions from 1989 to 2000 with a maximum energy of 209 GeV. The experiments were enormously successful in their precision studies of the electroweak interaction, in particular by tuning the center-of-mass energy of its collisions to produce Z and W bosons with high statistics. Since the discovery of the Z and W bosons (at the Super Proton-Antiproton Synchrotron at CERN in 1983), the final particle predicted by the SM and yet to be observed was the Higgs boson.

At the end of the LEP experiment, there were some hints of a Higgs measurement at around 115 GeV, but with only 1.7σ significance (while 5σ is considered a discovery). An extension of LEP was discussed to pursue this measurement with higher statistics, but in the end LEP was deconstructed as planned in order to clear the way for the LHC. When the LHC finally became fully operational in 2010, the ATLAS and CMS experiments quickly observed the Higgs boson at 125 GeV and officially announced its discovery in a joint press conference on July 4, 2012.

The operational phases of the LHC may be separated into four stages: Run 1, Run 2, Run 3, and the High-Luminosity LHC (HL-LHC). In the first stage Run 1, which ran from 2009 to 2013, the nominal collision energy was 7 TeV, meaning each proton beam was accelerated to 3.5 TeV. In 2012, however, the energy of each beam was increased to 4 TeV and data was collected with center-of-mass energy of 8 TeV, exceeding original design parameters. Operation ceased in 2013 for the Long Shutdown 1 (LS1), which was used for maintenance and upgrades to the accelerator complex and the detectors themselves. These upgrades were intended to increase the nominal collision energy of the LHC from 7 to 14 TeV – however, the bending magnets were only designed to handle up to 13 TeV, thus in Run 2, beginning in 2015 and ending in 2018, each proton beam had an energy of 6.5 TeV. Luminosity was greatly increased in Run 2, such that by 2016 more data had been collected than in all of Run 1. Luminosity continued to increase in 2017 and 2018, until operation was ceased again for the transition into the Long Shutdown 2 (LS2). LS2, which is ongoing as of the writing of this thesis, has been used for further maintenance and upgrade to the LHC accelerator complex and detectors and is projected to end in spring of 2022. When operations resume it will be the start of Run 3, which projects to accrue a total integrated luminosity greater than Runs 1 and 2 combined over the course of its data-taking from 2022 to 2025. Beginning in 2025, the Long Shutdown 3 (LS3) will be used for preparations for the HL-LHC, which aims to increase luminosity more than a factor of 10 above the LHC's nominal design value. Due to the magnitude of necessary modifications, some initial preparations for the HL-LHC have already begun in LS2.

Section 3.1.1 details the accelerator complex used to provide protons to the LHC ring at the desired energy. Section 3.1.2 and section 3.1.3 define luminosity and pileup respectively. Section 3.2 describes the ATLAS detector, and section 3.3 describes the ATLAS trigger system.

3.1.1 The Accelerator Complex

The protons destined to collide at the heart of ATLAS, or any other detector spaced around the LHC ring, begin as hydrogen atoms. The hydrogen atoms are stripped of their electrons by an electric field and then accelerated to 50 MeV by the Linac 2. The protons are then injected into the Proton Synchrotron Booster, followed by the Proton Synchrotron, then the Super Proton Synchrotron, which accelerate the particles to 1.4 GeV, 25 GeV, and 450 GeV respectively. Finally the protons are injected into the LHC via two beam pipes, where the two protons beams are accelerated to their final energy of 6.5 TeV. The protons in one beam pipe travel clockwise around the LHC while the protons in the other travel counterclockwise; then when they collide head-on at an interaction point, the total energy of the collision is the sum of the two beam energies. This acceleration chain can be seen in fig. 3.1.

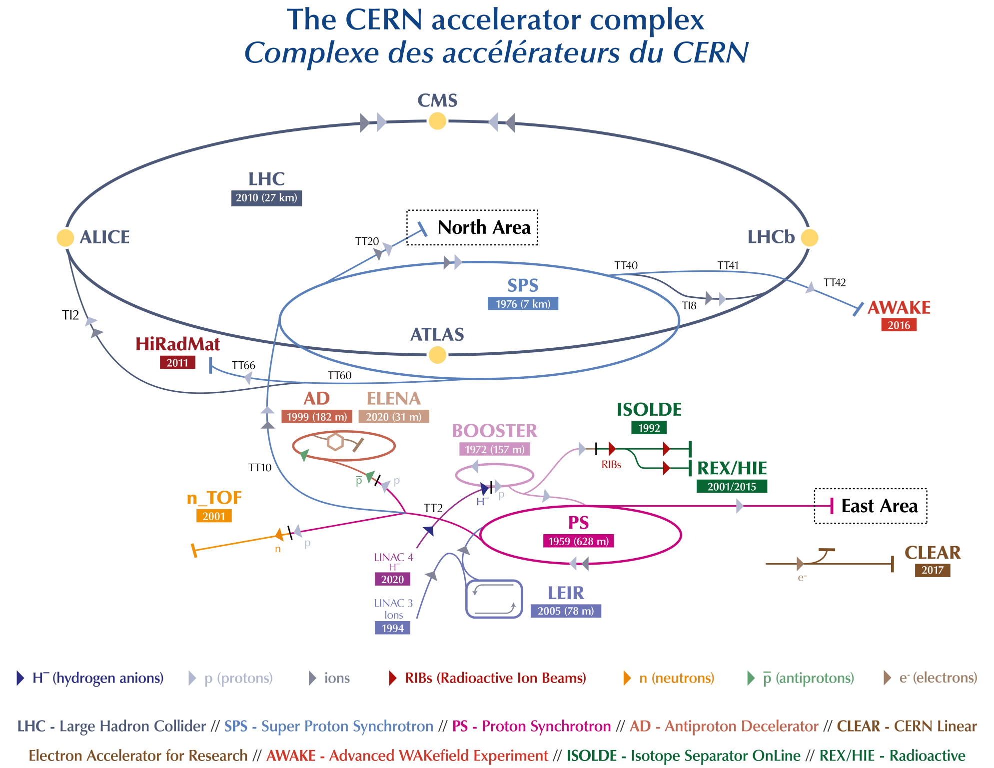

[redacted]

Figure 3.1: The LHC accelerator complex [25].

The proton beam experiences a longitudinally oscillating voltage generated by RF cavities as it travels around each accelerator ring. As a result, the protons end up clumped into *bunches* in RF potential wells called *buckets*. An LHC filling scheme refers to a certain pattern for which buckets are filled with protons and which are left empty. Those that are left empty are called empty bunches.

The nominal filling scheme for *pp* collisions is called the 25 ns scheme. The protons are captured in six bunches in the PS, where they are split into 18 bunches in 21 buckets (so 3 buckets are left empty). At that point they are accelerated to 25 GeV, after which they are split again to create 84 buckets, 72 of which are filled. For injection into the LHC, the protons are delivered in 39 batches of 72 bunches in each of the beams, where each bunch is separated by 25 ns within the batch, and each batch is separated by longer gaps to account for the powering cycle of the SPS and LHC magnetic elements. Thus, in total, the filling scheme of the LHC has 2808 filled bunches.

The filling scheme leads to a specific pattern of collisions in the detectors located on the LHC ring. A *bunch crossing*, when a bunch from each beam crosses in the middle of the detector, can be *paired*, *unpaired*, or *empty*. A paired bunch crossing means that the bunches in each beam are filled, and therefore a collision can occur. An unpaired bunch crossing means that one bunch is filled while the other is empty, and an empty bunch crossing has two empty bunches.

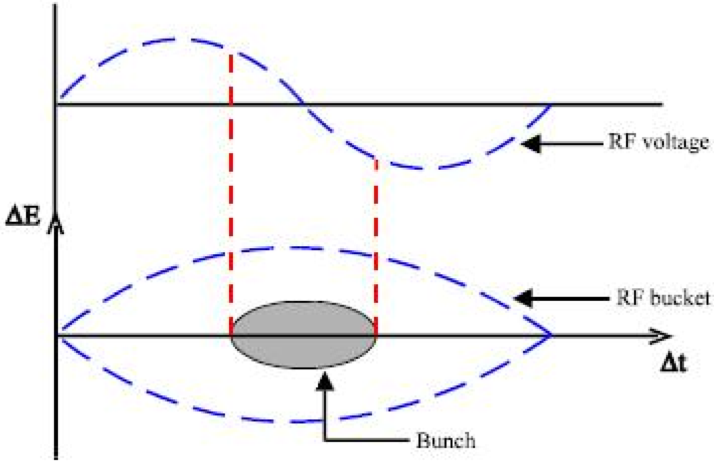

Figure 3.2: Representation of the voltage generated by RF cavities, and the corresponding proton bunch in an LHC bucket [26].

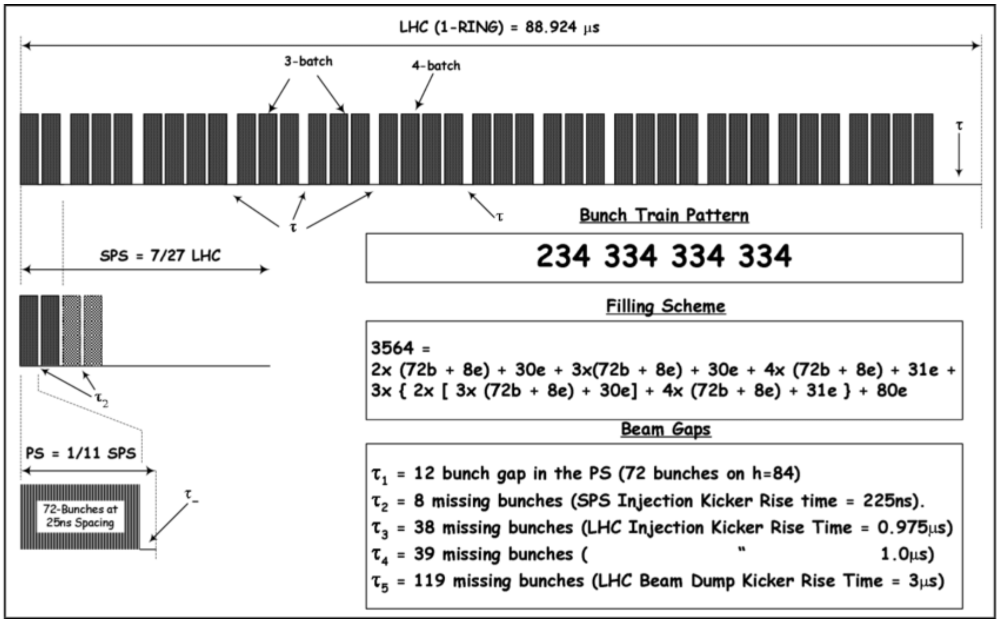

Figure 3.3: Schematic for a standard LHC filling scheme where proton bunches are separated by 25 ns [27].

3.1.2 Luminosity

Luminosity is a measure of how often protons can collide in a paired bunch crossing as determined by the parameters of the accelerator, and is expressed as collisions per per unit area squared per unit time. In the case of pp collisions at the LHC it can be written as the ratio of the rate of inelastic collisions, R_{inel}, to the inelastic pp collision cross-section, σ_{inel}:

$$\mathcal{L} = \frac{R_{inel}}{\sigma_{inel}}. \tag{3.1}$$

The rate R_{inel} can be further expressed in terms of parameters associated with the collider,

$$\mathcal{L} = \frac{\mu n_b f_r}{\sigma_{inel}}, \tag{3.2}$$

where μ is the average number of inelastic interactions per bunch crossing, n_b is the number of bunches crossing the interaction point, and f_r is the revolution frequency of the collider. It is possible to break this down even further by expressing μ and σ_{inel} in terms of parameters associated with the bunch itself:

$$\mathcal{L} = \frac{n_b f_r n_1 n_2}{2\pi \Sigma_x \Sigma_y} F \tag{3.3}$$

where n_1 and n_2 are the number of protons in the incoming bunches, and Σ_x and Σ_y are the horizontal and vertical widths of the beam profiles. The factor F contains geometric factors, as the beam does not cross exactly head-on but rather at an angle. The general form of the equation makes intuitive sense; as the number of protons in either bunch increases, the probability of a collision increases. Similarly, as the protons in each beam are focused into a smaller cross-sectional area the density increases and again the probability of collision increases. From eq. (3.3) it is seen that the units of luminosity are $\mathrm{cm}^{-2}\mathrm{s}^{-1}$. Total integrated luminosity is a measure of luminosity delivered over time, and it is convenient to express in terms of inverse femtobarns, fb^{-1}, where 1 barn $= 10^{-24}$ cm^2 and 1 fb $= 10^{-15}$ barn. The total integrated luminosity for Run 2 is shown as a function of time in fig. 3.4.

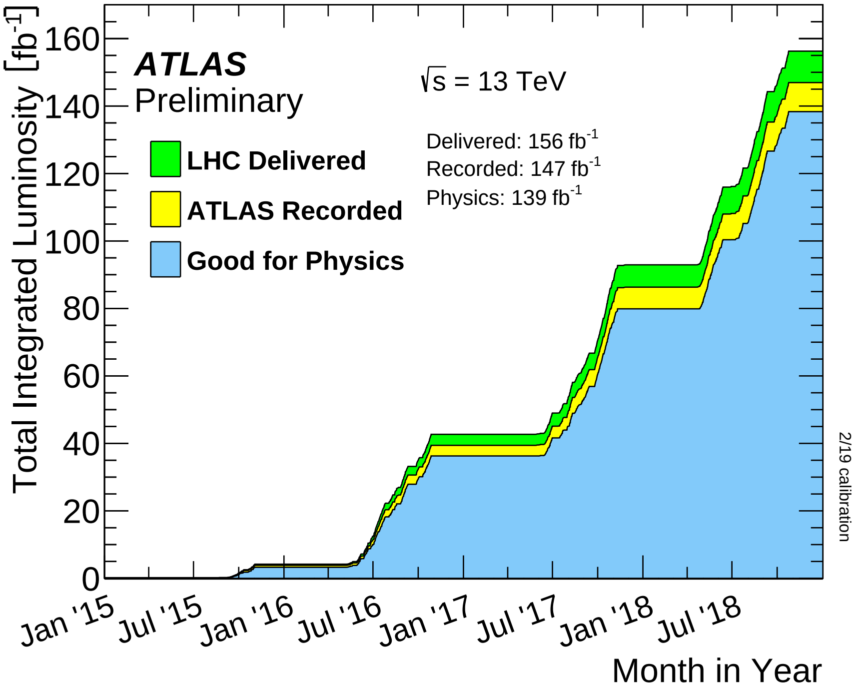

Figure 3.4: Total integrated luminosity for data from pp collisions that was delivered to the LHC, recorded by ATLAS, and passed data quality critera over the course of Run 2.

3.1.3 Pileup

Pileup is when multiple inelastic interactions occur in a single bunch crossing. This is closely related to the value μ in eq. (3.2), signifying average inelastic interactions per bunch crossing, and indeed the term pileup will often be used in that context as well. As luminosity

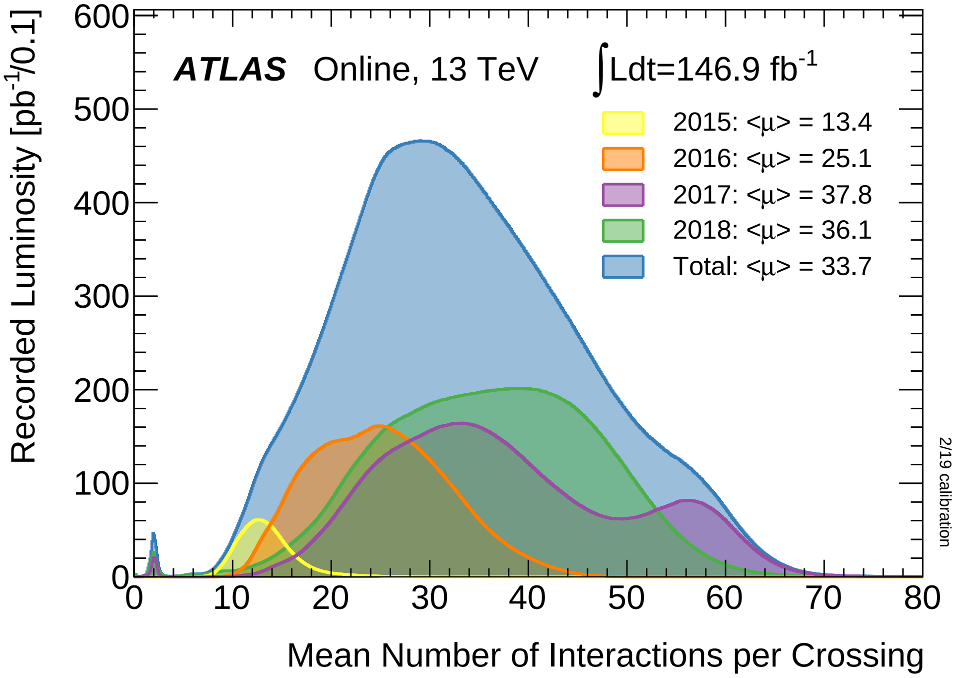

Figure 3.5: Distributions of average interactions per bunch crossing for Run 2 and its constituent years.

increases, the probability of having several collisions in a bunch crossing does too; therefore as luminosity varied over each data-taking year in Run 2 so did pileup, as can be seen in fig. 3.5. Over the course of Run 2, the average pileup value was 33.7 interactions per bunch crossing. The pileup distribution in data is essential to understand so that MC samples can be appropriately generated and their events reweighted to match the data distribution.

3.2 The ATLAS Detector

The ATLAS detector, seen in fig. 3.6, is an incredible feat of technological innovation and engineering, measuring 44 m long and 25 m in diameter with a weight of 7000 tons.

Several coordinate systems are defined for the ATLAS detector, as shown in fig. 3.7, and all share the nominal interaction point as the origin. In a rectangular coordinate system, the x-axis is defined to be pointing from the interaction point in towards the center of the LHC ring (parallel to the surface of the earth), the y-axis to be pointing directly upwards towards the surface, and the z-axis to be along the beamline (counterclockwise along the LHC ring as seen from above). In a cylindrical coordinate system, the x and y coordinates

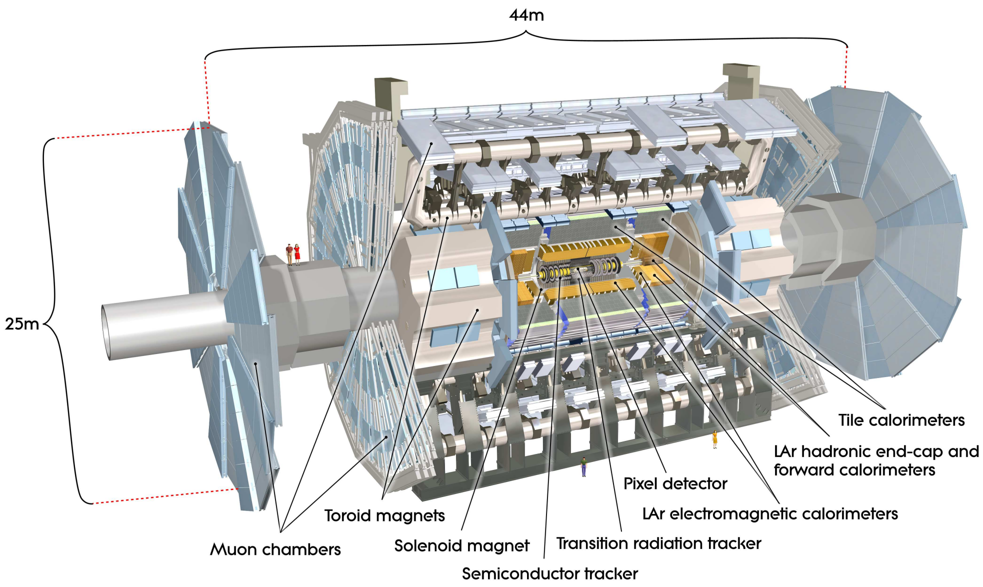

Figure 3.6: The ATLAS detector with all subdetectors labeled. [28]

are replaced with the azimuthal angle $\phi \in [-\pi, \pi]$ and polar angle $\theta \in [0, \pi]$, where $\phi = 0$ coincides with the x-axis and $\theta = 0$ corresponds to the z-axis.

The most common and convenient coordinate system, however, further replaces the θ coordinate with the pseudorapidity $\eta = -\ln\left[\tan\left(\frac{\theta}{2}\right)\right]$, which describes angles with respect to the colliding beams; $\eta = 0$ is perpendicular to the beamline and tends towards $\pm\infty$ as the angle approaches co-linearity with the beamline, with η negative on the C-side of the detector and positive on the A-side. This has the advantage that differences in η are Lorentz boost-invariant. Radial distance from the beamline, $r = \sqrt{x^2 + y^2}$, and angular distance $\Delta R = \sqrt{\phi^2 + \eta^2}$ are also useful quantities that are frequently used.

The main cylindrical body of the ATLAS is referred to as the *barrel*, while circular disk layers on each end of the detector as known as the *endcaps*. The transition from the barrel region to the endcaps region is usually defined in terms of η. The half of the detector with $z > 0$ is called A-side, and with $z < 0$ is called C-side.

The detector is composed of three main subdetectors, which form concentric cylindrical layers around the collision point. Closest to the beamline is the inner detector (ID), followed by the calorimeters, with the muon spectrometer (MS) on the outside. The particular ordering of these subdetectors is crucial to particle identification and accurate energy measurement.

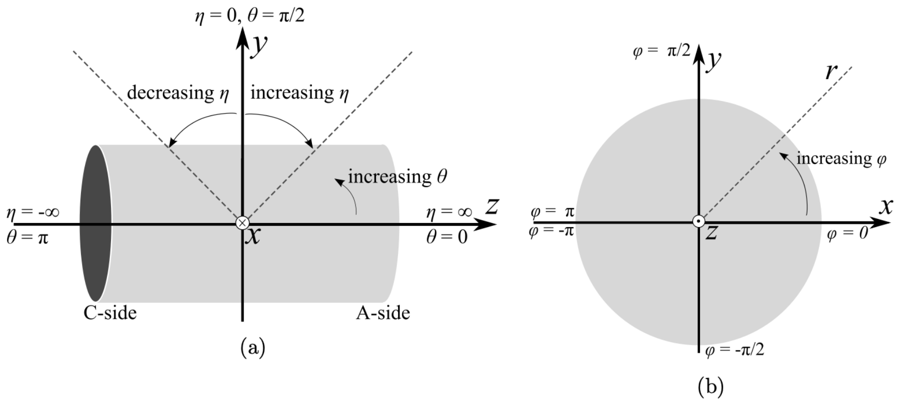

(a) (b)

Figure 3.7: Coordinate systems defined for the ATLAS detector. [29]

3.2.1 Inner Detector

The ID records the trajectories of all charged particles that are produced in a collision, thereby giving information on charge and momentum. It is composed of three subdetectors, each implementing a different type of technology as seen in fig. 3.8. The innermost layer is the silicon pixel detector. Moving outwards, we find the SemiConductor Tracker (SCT), followed by the Transition Radiation Tracker (TRT). The silicon pixels and SCT provide tracking with extremely high granularity at small radii, and the addition of the lower-granularity TRT information at larger radii results in excellent pattern recognition. In total the ID has a radius of 2.3 m and a length of 7 m, and it is immersed in a 2 T uniform magnetic field from a superconducting solenoid magnet. A strong magnetic field is crucial as it must produce sufficient bending of ultra-relativistic particles, as compared with the precision of the tracking instruments, that a reliable momentum measurement can be calculated. The precision tracking layers – the pixel detector and the SCT – together cover up to $|\eta| < 2.5$, and the TRT adds additional tracking up to $|\eta| < 2.0$.

Figure 3.9 shows a cut-away view of one-quarter of the ATLAS ID, including the cylindrical orientation of detector elements in the barrel region and the disk-like orientation of components in the endcaps region.

Silicon Pixel Detector

The silicon pixel detector has three primary cylindrical layers in the barrel and three disks on each side in the endcaps. The cylindrical layers are set at a radius of 50.5, 88.5, and 122.5

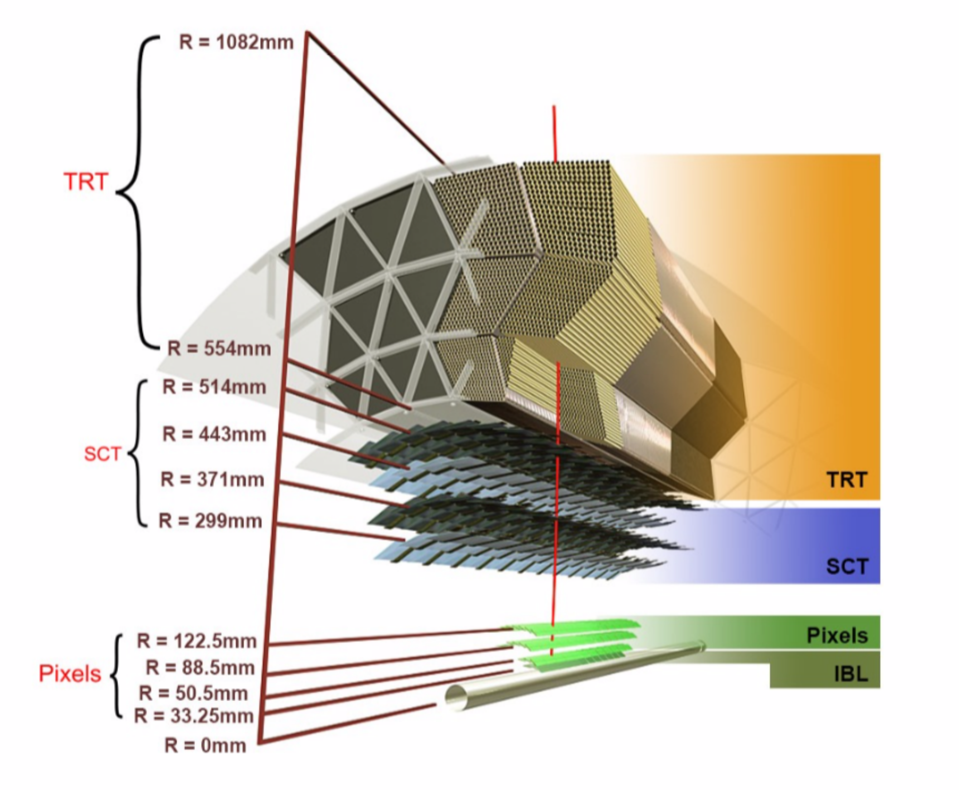

Figure 3.8: Schematic of the ATLAS inner tracker.

mm from the center of the beam line, and the disks are placed at $z \pm 495, 580$, and 650 mm. The design therefore provides a minimum of three points with which to perform tracking over the active region of the pixel detector.

A single pixel is 50 μm in the ϕ direction by 400 μm in the z direction in the barrel (or in the r direction in the endcaps). A module is composed of a sensor, front-end electronics, and flex-hybrids with control sensors, and each sensor has 46080 pixels for an area of 16.4 × 60.8 mm. There are about 67 million pixels in the barrel and 13 million in the endcaps, which corresponds to an active area of about 1.7 m^2.

For luminosities above 2×10^{34} cm^{-2}s^{-1}, which were expected (and achieved) in Run 2 data-taking, the read-out efficiency of the pixel layers was predicted to deteriorate. A fourth cylindrical layer, called the Insertable b-layer (IBL), was therefore installed during LS1 and was fully operational for Run 2 data-taking to maintain the performance of the pixel layers. The modules in the IBL are composed of pixels with size 50 × 250 μm, set at a radius of 33.5 mm from the center of the beam line. For the IBL to be installed so close, the beam

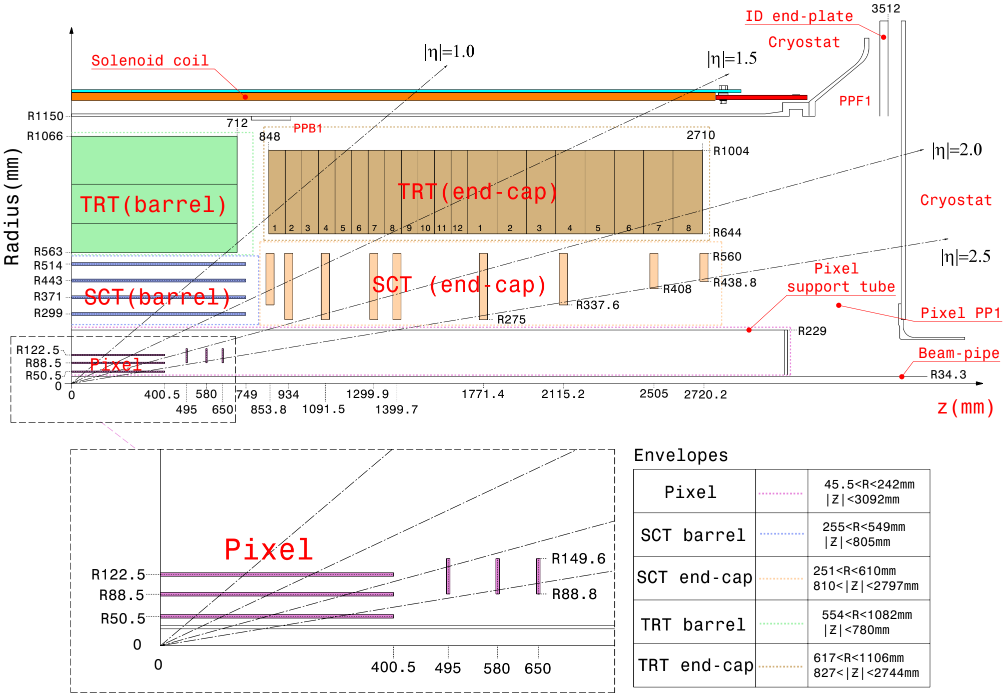

Figure 3.9: A cut-away view of one quarter of the ATLAS inner detector.

pipe was replaced to have a smaller diameter with an inner radius of 23.5 mm.

SemiConductor Tracker

The pixel detector is surrounded by the SCT, a precise silicon microstrip tracker. The SCT has silicon-strip sensors arrayed in 4 cylindrical layers in the barrel and 9 disks in the endcaps. The radial position of the barrel layers and longitudinal position of the endcap layers can be found in table 3.1. The barrel layers are composed of 12 rings of modules extending a total of 1.492 m along the z axis, symmetric about A-side and C-side, with a total of 2112 modules. The endcap disks have a more complicated layout, with 4 types of modules and 5 types of sensors. Each disk has either one, two, or three layers of modules which are distinguished as Inner, Middle, or Outer layers. Cumulatively there are 988 modules in the endcaps. The position resolution in $r\phi$ is 17 μm in the barrel and 16 μm in the endcaps.

Transition Radiation Tracker

The TRT is composed of cylindrical drift tubes, known as straws. The straws are 4 mm in diameter, filled with a gas mixture of xenon (70%), CO_2 (27%), and O_2 (3%), and have a gold-plated tungsten wire at their center. This wire acts as the anode, held at ground

Barrel layer	**Radius** [m]	**Number of modules**
Barrel 3	299	384
Barrel 4	371	480
Barrel 5	443	576
Barrel 6	514	672
Endcaps layer	**Position** [m]	**Number of modules**
Disk 1	±853.8	92
Disk 2	±934	132
Disk 3	±1091.5	132
Disk 4	±1299.9	132
Disk 5	±1399.7	132
Disk 6	±1771.4	132
Disk 7	±2115.2	92
Disk 8	±2505	92
Disk 9	±2720.2	52

Table 3.1: SCT layout.

potential, and the straw acts as a cathode with a high voltage of 1530 V which corresponds to a gas gain of 2.5×10^4.

Like the pixel detector and the SCT, the TRT can be separated into its barrel and endcaps components. The barrel component has three layers of planes where the straws are aligned parallel to the beamline, and the endcaps arranged into wheels with eight-fold symmetry where straws extend radially at a given z position. A module has an array of straws interspersed with radiators, namely polypropylene fibers, all of which is encased in a carbon-fiber composite shell. The straws are arranged with hexagonal tesselation, such that neighboring straws have about 6.6 mm between their centers. A particle with transverse momentum (p_T) above 500 MeV and $|\eta| < 2.0$ is expected to cross about 35 drift tubes as it traverses through the TRT. Between the barrel and endcaps modules, there are 370,000 drift tubes in total.

3.2.2 Calorimeters

The ID is surrounded by the calorimeters, which are designed to absorb all the energy of an incoming particle; this allows for measurement of particle energy as well as the spatial location for that energy deposit. There are two kinds of calorimeters in the ATLAS detector.

Immediately outside of the ID is the electromagnetic calorimeter (ECal), which absorbs and measures the energy from electromagnetic showers covering $|\eta| < 3.2$. Further electromagnetic coverage is provided for $3.1 < |\eta| < 4.9$ by the forward calorimeter (FCal). Outside of the ECal is the hadronic calorimeter (HCal), which absorbs and measures the energy from hadronic showers. A cross-section of the arrangement can be seen in fig. 3.10.

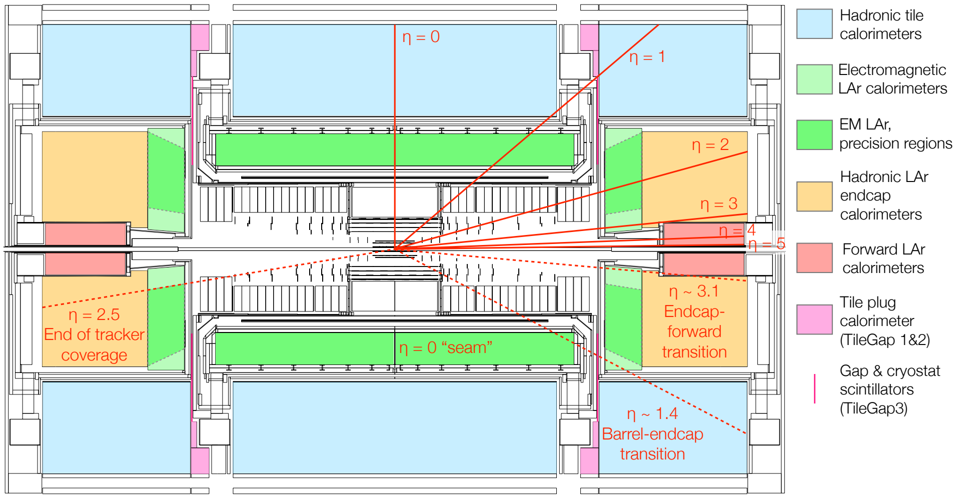

Figure 3.10: Calorimeters in the ATLAS detector.

Both the electromagnetic and hadronic calorimeters are sampling calorimeters, meaning that active detector layers are alternated with passive absorber layers. This means that only part of the shower's energy is sampled, so a correction factor must be applied to calculate the total energy. In the barrel, the ECal is housed in a cryostat. In the endcaps, the ECal, HCal, and FCal are all contained within cryostats as they are all located close to the beamline.

Electromagnetic Calorimeter

The ECal is a lead-liquid argon calorimeter, where lead acts as the passive absorber and liquid argon (LAr) is the active detector layer. Liquid argon was chosen for its linear behavior, stability of response over time and radiation-hardness, while the thickness of the lead was optimized for performance in energy resolution. The ECal has an accordian structure, segmented into three layers for $|\eta| < 2.5$ and two layers for $2.5 < |\eta| < 3.2$, which allows for complete coverage in ϕ with no azimuthal cracks. The modules are arranged cylindrically in the barrel and into coaxial wheels in the endcaps. There is a presampler in front of the

ECal, made of a separate liquid-argon layer split into 64 and 32 azimuthal sectors in the barrel and endcaps respectively. This is used to provide a correction for the energy lost by electrons and photons before reaching the calorimeters.

The detector has a thickness of 22−33 radiation lengths (X_0) in the barrel and 24−38/, X_0 in the endcaps, shown more precisely in fig. 3.11.

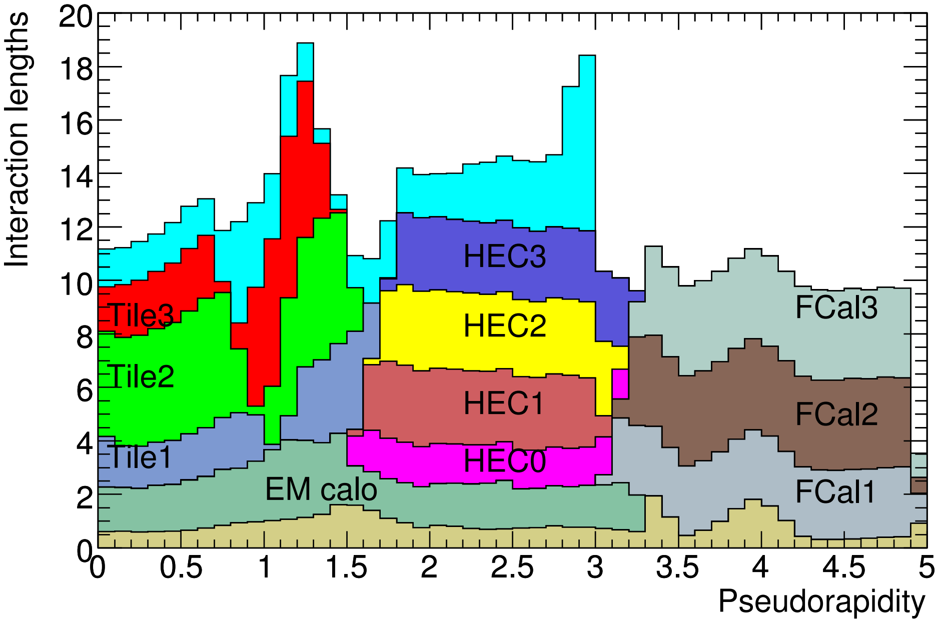

Figure 3.11: The depth of the ATLAS calorimeters, in radiation lengths.

Hadronic Calorimeter

The HCal is more complex than ECal, and can be separated into three regions: the tile calorimeter, hadronic endcap calorimeter (HEC), and forward calorimeter (FCal).

The tile calorimeter is located in the barrel, surrounding the barrel ECal. Its barrel region covers $|\eta| < 1.0$, and the extended barrel components are at $0.8 < |\eta| < 1.7$ on either side. It uses steel as its absorbing material and scintillating tiles as the active detector material. It has three layers ranging from 2.28 m to 2.45 m in r, each azimuthally segmented into 64 modules.

The HEC is split into two wheels of two layers each, placed outside of the endcap ECal detectors, and covers the range $1.5 < |\eta| < 3.2$. Like the ECal it uses LAr as its active medium, but instead of lead it uses copper as its absorber. The wheels closest to the IP use copper plates of thickness 25 mm, while those further have thickness 50 mm. The plates extend from 0.475 m to 2.03 m in r.

The FCal covers the very forward direction, $3.1 < |\eta| < 4.9$, and is split into three modules. All of them feature LAr as their active medium, however the first module uses copper for its absorber while the second and third use tungsten. Copper was chosen to optimize electromagnetic measurements, while tungsten was chosen with the measurement of hadronic interactions in mind.

3.2.3 Muon Spectrometer

The Muon Spectrometer (MS) is the outermost subdetector layer of the ATLAS detector as well as the largest, and is composed from four kinds of tracking chambers – Resistive-Plate Chambers (RPC), Thin-Gap Chambers (TGC), Monitored Drift Tubes (MDT), and Cathode Strip Chambers (CSC). As the name suggests, it is designed to detect final-state muons. A system of superconducting toroid magnets is built in to the detector to bend the trajectories of the muons, allowing for momentum measurement. The layout of the MS, seen in fig. 3.12, is separated into two regions as is consistent with the rest of the ATLAS detector: the barrel ($|\eta| < 1$) and the endcaps ($1 < |\eta| < 2.7$). The barrel chambers are arranged into three layers of stations around the beamline with radii of approximately $r = 5,\ 7.5,$ and $10\,\mathrm{m}$. The endcaps chambers are arranged into four circular disks at $z = \pm\,7,\ 10,\ 14,$ and $21 - 23\,\mathrm{m}$, concentrically centered on the beamline.

Tracking is provided by the MDT chambers located throughout both the barrel and endcaps. In the forward direction, $2 < |\eta| < 2.7$, CSCs are also used as they are better able to handle the high rate and background present in that region. The RPC and TGC detectors are located in the barrel and endcaps respectively, and are used for triggering.

In theory, the only particles in the Standard Model that are not fully absorbed and are able to continue into the final layer of the ATLAS detector, i.e. the MS, are muons and neutrinos. In practice, however, this is not always true. Since hadronization is a statistical process, some particles are able to traverse the entirety of the calorimeters and continue into the MS before all of their energy is absorbed. These jets are known as *punch-through jets.*

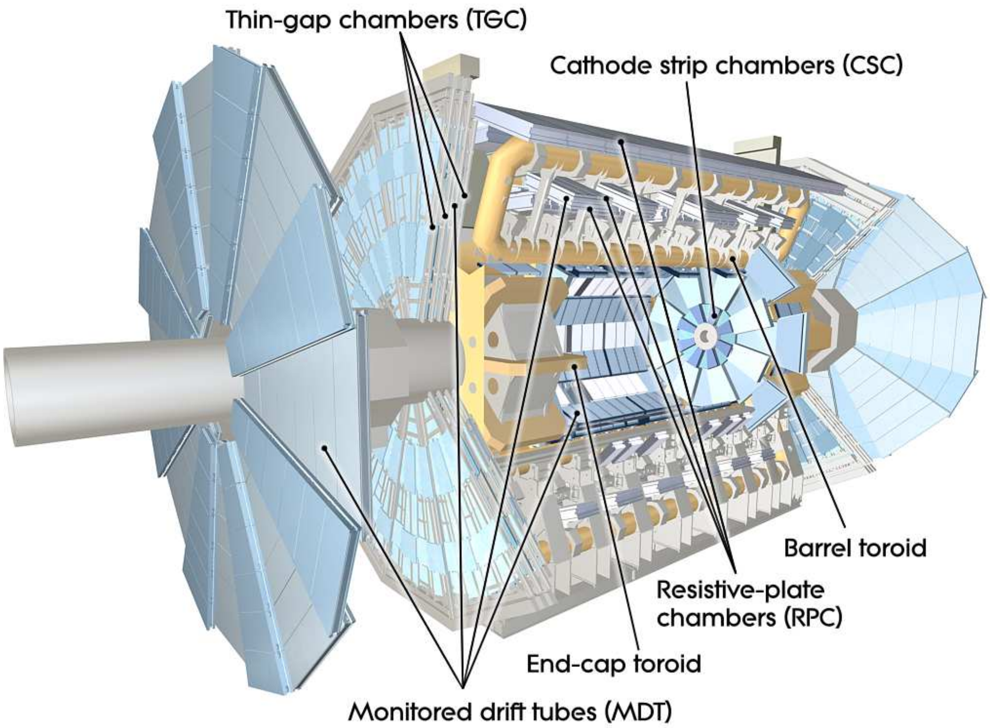

Figure 3.12: Schematic of the ATLAS muon spectrometer.

Monitored Drift Tubes

A Monitored Drift Tube chamber, seen in fig. 3.14, has two multilayers. Each multilayer has four layers of MDT tubes if it's in an inner station, or three layers of tubes if it's in a middle or outer station. The tubes are aluminum, 30 mm in diameter, and have a tungsten-rhenium wire of diameter 50 μm at the center. They are filled with Ar-CH_4-N_2 gas at a pressure of 3 bar, which corresponds to a gas gain of 2×10^4. Depending on their location in the detector, the tube lengths vary from 70 cm to 630 cm. There are 372000 tubes total throughout the ATLAS detector, with an average resolution of 80 μm per tube.

Cathode Strip Chambers

Cathode Strip Chambers are multiwire proportional chambers and, like the MDTs, they use tungsten-rhenium wires. In their case, the diameter of each wire is 30 μm, and the gas used is Ar-CO_2-CF_4 with a gain of 10^4. CSCs are able to measure both z/R and ϕ directions simultaneously, which means it is able to handle much higher rates than MDTs and are therefore placed in the forward region, where particle fluxes and muon-track density are

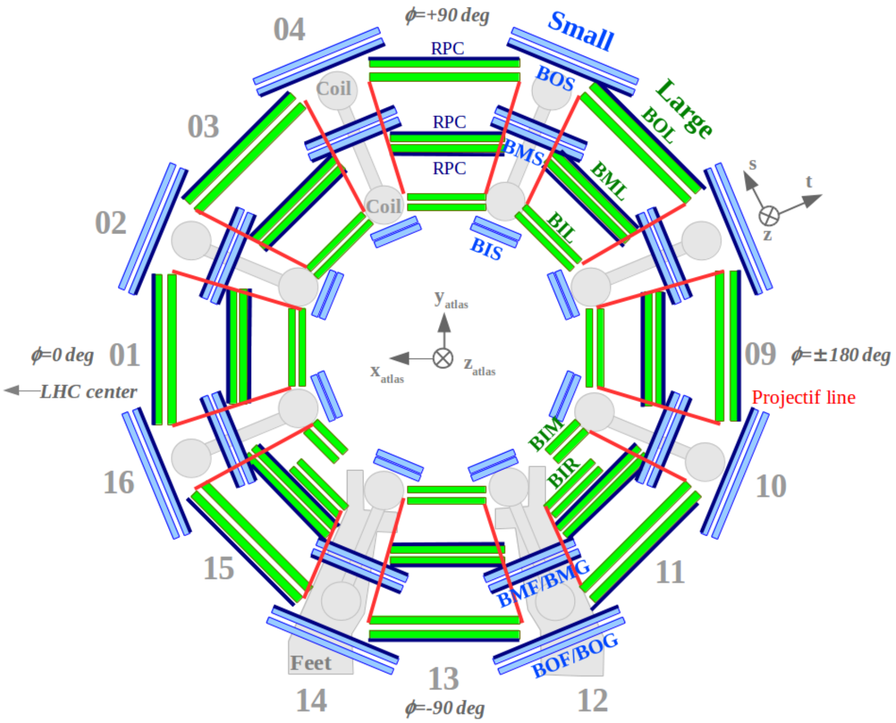

Figure 3.13: Cross section of the MS barrel.

highest. Specifically, CSCs replace the innermost layer of MDTs for $2 < |\eta| < 2.7$.

Resistive-Plate Chambers

Resistive-Plate Chambers are used for triggering in the barrel region of the MS. They have two parallel resistive bakelite plates with a 2 mm gas gap between them, filled with 97% tetrafluoroethane ($C_2H_2F_4$) and 3% isobutane (C_4H_{10}). A uniform electrical field of 4.5 kV/mm is applied to multiply primary ionization electrons into avalanches. The signal is read out on either side of the chamber via capacitive coupling, and the time difference between the two signals improves the time resolution. A chamber is made from two layers oriented perpindicularly to each other, so that one layer provides an η measurement and the other provides a ϕ measurement. The spacial resolution is 1 cm, and the time resolution is 1.5 ns.

Thin-Gap Chambers

Thin-Gap Chambers are used for triggering in the endcaps region of the MS, and they have a similar design as CSCs. Anode wires held at 3100 V, spaced 1.8 mm apart, are placed in

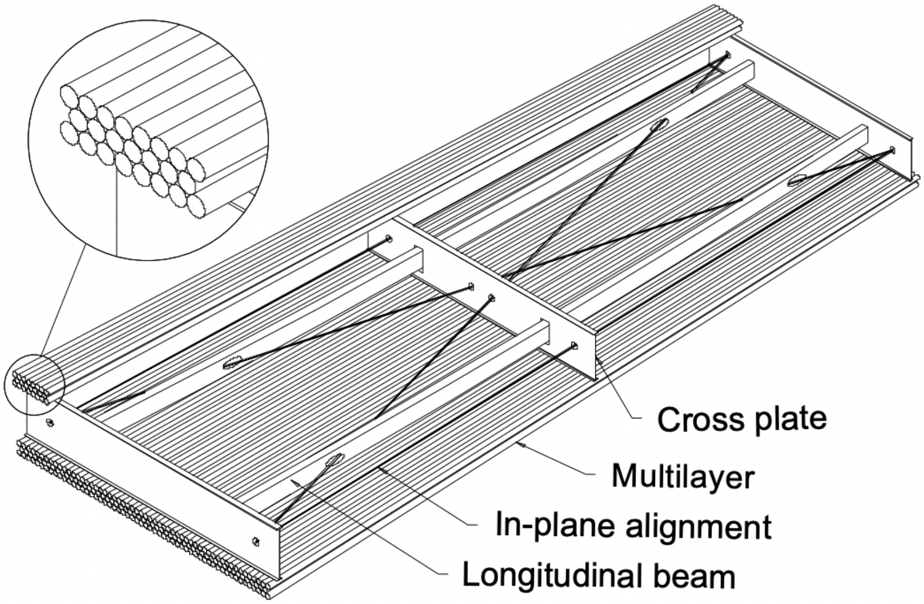

Figure 3.14: Cross section of an MDT chamber, with part of the top multilayer removed.

a gas gap of 2.8 mm. This means that the anode-cathode distance is only 1.4 mm, which is smaller than the distance between wires. The gas mixture is 55% CO_2 and 45% $n{-}C_5H_12$ with a gain of 10^6.

3.3 Trigger System

Nominal bunch spacing in the LHC was 25 ns throughout Run 2, meaning that ATLAS observed and measured 40 million collisions per second, i.e. with a rate of 40 MHz. It is not feasible to store all of this data – about 1 MB of data is collected per collision [30] – so a trigger system was employed to select and store only the events that were deemed particularly interesting. The ATLAS Level 1 (L1) trigger is hardware-based and makes a decision based on coarse, limited detector information to either store or discard the event within $2.5\,\mu$s. This level reduced the rate to 100 kHz. The second level, the High Level Trigger (HLT), uses more complete and higher-granularity detector information to make further selections on events, for an average final rate of 1 kHz.

The L1 trigger is made of a set of trigger items. Each item imposes specific criteria chosen to search for a particular kind of interesting activity. Some trigger items search for detector signatures consistent with muons, electrons, and photons, as well as jets and τ-

leptons decaying to hadrons. Others search for more global phenomena such as large missing or total transverse energy. In each event, the L1 trigger defines one or more Regions-of-Interest (RoIs), which indicate where the interesting activity was spatially located in the detector. An L1 trigger item will then provide the seed for an HLT chain, which makes a decision to keep or throw away that event with more refined criteria and full detector information from within the RoI. A single L1 trigger item may seed several HLT chains.

The triggers associated with common processes can still have a higher firing rate than desired, given the constraints on the final overall trigger rate. In these cases a prescale is applied, meaning that only a fraction of the events passing the HLT trigger chain are actually saved. A prescale of 4, for example, means that 1 event in 4 that pass the trigger is saved.

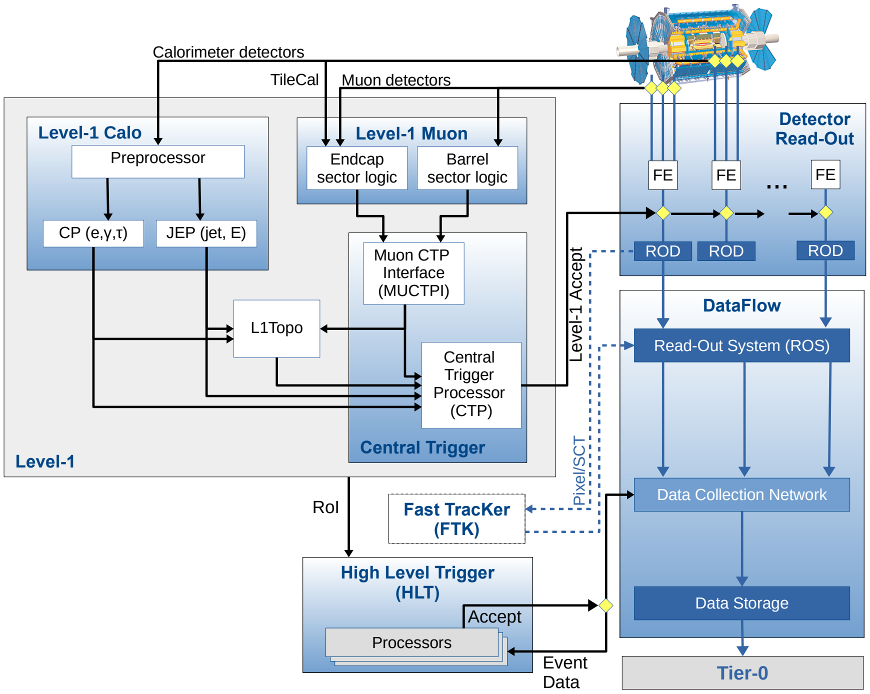

Figure 3.15: Schematic showing the flow of the trigger/DAQ system. [31].

3.3.1 Muon RoI Cluster trigger

The analysis described in this thesis employs a signature-driven trigger that selects events based on the detector signature of a decay in the MS. The L1 item is L1_2MU10, and the HLT chain is `HLT_j30_muvtx_noiso`. It is based on the Run-1 trigger described in Ref. [32], but the previously-employed strict isolation requirements are no longer applied.

The trigger is efficient for LLPs decaying to hadronic jets from the outer region of the HCal to the MS middle station. When they decay in the MS, the resulting hadronic showers tend to be reconstructed by the L1 Muon trigger system as a cluster of muon RoIs centred on the LLP line of flight. A cluster of muon RoIs is defined as at least three (four) muon RoIs lying within a $\Delta R = 0.4$ radius in the MS barrel (endcaps)[1].

Thus, the Run 2 "noiso" trigger is implemented to select events passing L1_2MU10, which means that there were two muon RoIs with $p_T \geq 10$ GeV in the event. Then at HLT a cluster of RoIs is required, i.e. three (four) muon RoIs in the barrel (endcaps) within a cone of $\Delta R < 0.4$. L1 muon RoIs are formed in a $\Delta\eta \times \Delta\phi = 0.2 \times 0.2$ region ($\Delta\eta \times \Delta\phi = 0.1 \times 0.1$ region) in the barrel (endcaps), so a cone with radius 0.4 is appropriate to select groups of RoIs. L1 muon RoI formation is based on deviations from an infinite momentum track from an object that is assumed to originate at the IP, which is not the case for our signal objects. However this is not problematic since the L1 muon RoIs reconstructed in signal events are from hadronic showers, and the abundance of hits means that some combinatorial combination will resemble a muon originating from the IP. In these events, the L1 muon RoIs are not necessarily created from a single-particle trajectory.

This trigger does not have any isolation requirements with respect to either calorimeter jets or ID tracks, and consequently selects both signal-like events that are isolated, and an orthogonal sample of background events that are non-isolated.

3.3.2 Zero bias trigger

Backgrounds can come from a variety of difference sources and many are not properly simulated in MC – this includes pileup from minimum bias events, beam-gas, beam-halo, cavern backgrounds, cosmic rays, and electronic noise. One of the realistic ways of estimating these backgrounds involves using raw data acquired with a special *zero-bias* trigger, which fires on the bunch crossing one full LHC revolution after a low-threshold, calorimeter-based luminosity trigger. It was designed this way to select events with no bias with respect to what kind of activity is present in the event, hence the name. The HLT chain for this trigger is called `HLT_zb_noalg_L1ZB`. Since it ran throughout Run 2, it contains the same background activity as was present in the Muon RoI Cluster trigger (or any trigger used for signal selection).

---

[1] The RoI multiplicity in barrel and endcaps has been fixed using the models and mass points in [32].

Chapter 4

Data and MC Samples

4.1 Monte Carlo samples

Monte Carlo (MC) simulation, also known as the Monte Carlo method or multiple probability simulation, is a mathematical technique used when an element of probability is present. It refers to a class of computational algorithms that uses numeral analysis to evaluate a range of possible outcomes and calculate the probability of a particular outcome occuring. Input variables are provided with probability density functions, and a computation is repeatedly performed while randomly sampling from these input distributions. The more times the calculation is performed, the higher the statistics and so the MC prediction of the outcomes becomes more accurate.

This method is invaluable for the simulation of elementary particles, since their interactions are probabilistic in nature. Using the MC method, pp collisions are simulated with a given *parton distribution function* (PDF), which expresses the probability that a given parton will participate in an inelastic collision. The interactions and decays of the particles produced in the collision are then simulated as they traverse the material in the ATLAS detector. This method can be used to generate and study both signal and background events.

In the analysis described in this thesis, MC samples were produced for each signal benchmark model mass point to simulate the decay of the LLPs into hadronic jets in the ATLAS detector in pp collisions at $\sqrt{s} = 13$ TeV according to model parameters. The lifetime of each sample was chosen to have roughly equal numbers of LLP decays in the calorimeters and the MS, as the samples were shared with the CalRatio analysis, which performs a search for displaced hadronic jets in the calorimeters [33]. A second, greater lifetime was generated for some samples in order to cross-check the lifetime-extrapolation of efficiencies and limits. All samples were also generated with pileup and luminosity distributions to match run conditions in real data.

4.1.1 Signal MC samples

Samples for the HSS model, as described in section 2.3.1, were generated with the Hidden Abelian Higgs Model `HAHM_variableMW_v3_UFO` [34] using MadGraph5_aMC@NLO [35], interfaced to the Pythia8 [36] parton shower model and using EvtGen 1.2.0 [37] to model b- and c-hadron decays. All generated events include production and decay kinematics. The parameterization at leading order used for the proton parton distribution function (PDF) is NNPDF2.3LO [38]. Table 4.1 reports the parameters for the simulated model.

m_Φ [GeV]	m_s [GeV]	**Low lifetime** $c\tau$ [m]	**Low lifetime** **Events**	**High lifetime** $c\tau$ [m]	**High lifetime** **Events**
60	5	0.217	600 k	-	-
	15	0.661	300 k	-	-
125	5	0.127	160 k	0.411	610 k
	15	0.580	510 k	-	-
	35	1.310	720 k	2.630	510 k
	55	1.050	1010 k	5.320	460 k
200	50	1.255	200 k	-	-
400	100	1.608	200 k	-	-
600	50	0.590	300 k	-	-
	150	1.840	300 k	3.309	150 k
	275	4.288	1000 k	-	-
1000	50	0.406	300 k	-	-
	275	2.399	300 k	4.328	150 k
	475	6.039	1000 k	-	-

Table 4.1: Summary of the masses and proper lifetimes ($c\tau$) simulated for the HSS model.

Figures 4.1 and 4.2 show the distribution of the p_T, β, η, ϕ, L_{xy} and L_z of the long-lived particles for some signal MC benchmark samples.

4.1.2 Multijet simulation

Simulated multijet samples were used to study background events coming from punch-through jets as well as the performance of triggering and vertex reconstruction. These samples are divided into 13 *slices* according to the p_T of the leading jet. They are named JZXW where X $\in \{0, 12\}$ indicates the p_T range of the leading jet for the events in that slice, as seen in Table 4.2.

Slice	**Leading jet $\mathbf{p_T}$** [GeV]	**Events**
JZ0W	0 – 20	31987000
JZ1W	20 – 60	31995000
JZ2W	60 – 160	31970500
JZ3W	160 – 400	31758000
JZ4W	400 – 800	31900000
JZ5W	800 – 1300	26656000
JZ6W	1300 – 1800	35494400
JZ7W	1800 – 2500	31099500
JZ8W	2500 – 3200	31986000
JZ9W	3200 – 3900	28507000
JZ10W	3900 – 4600	29713000
JZ11W	4600 – 5300	31751000
JZ12W	> 5300	31595600

Table 4.2: Summary of the leading jet p_T range and number of events generated for each multijet slice.

All multijet slices were generated using PYTHIA8 8.230 [39] with leading-order matrix elements that were matched to the parton shower. The NNPDF2.3LO PDF set was used in the matrix element generation, the parton shower, and the simulation of the multi-parton interactions. The A14 set of tuned parameters was used. Perturbative uncertainties were estimated through event weights that encompass variations of the scales at which the strong coupling constant is evaluated in the initial- and final-state shower as well as the PDF uncertainty in the shower and the non-singular part of the splitting functions.

4.2 Data samples

This analysis used data collected in pp collisions with stable beams at $\sqrt{s} = 13$ TeV from the full Run 2 data-taking period, which ran from 2015 to 2018. All data had the nominal

25 ns bunch filling scheme. We require the muon spectrometer to be fully operational as it is critical for displaced vertex reconstruction, and we apply the Good Run List (GRL). After these data quality requirements, the total integrated luminosity is 139 fb^{-1}. The uncertainty on the integrated luminosity is 1.7%, obtained from measurements by the LUCID-2 detector [40].

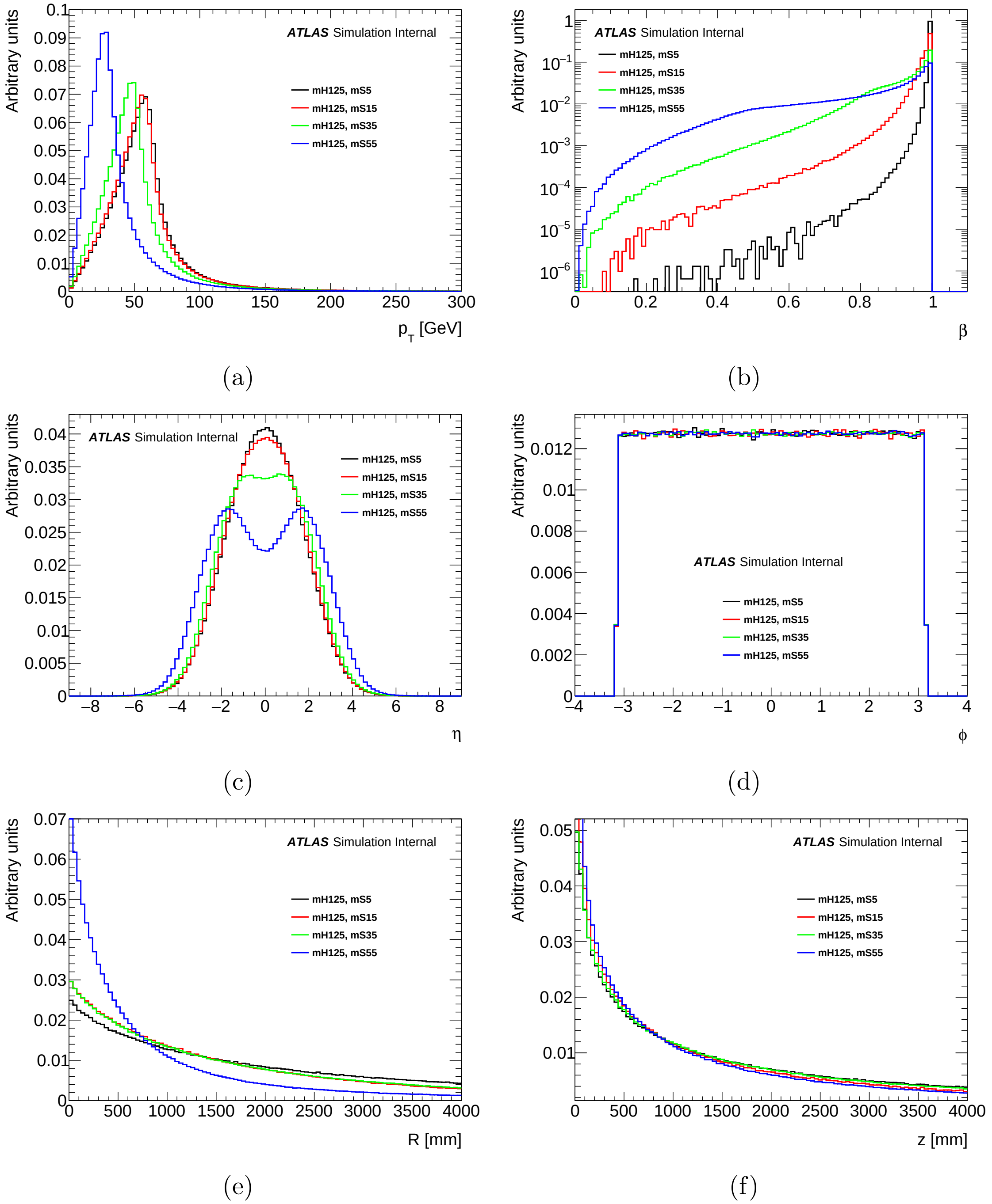

(a) (b) (c) (d) (e) (f)

Figure 4.1: Truth-level distributions of some of the key variables obtained from the generated HSS MC samples where $m_{\Phi} = 125$ GeV.

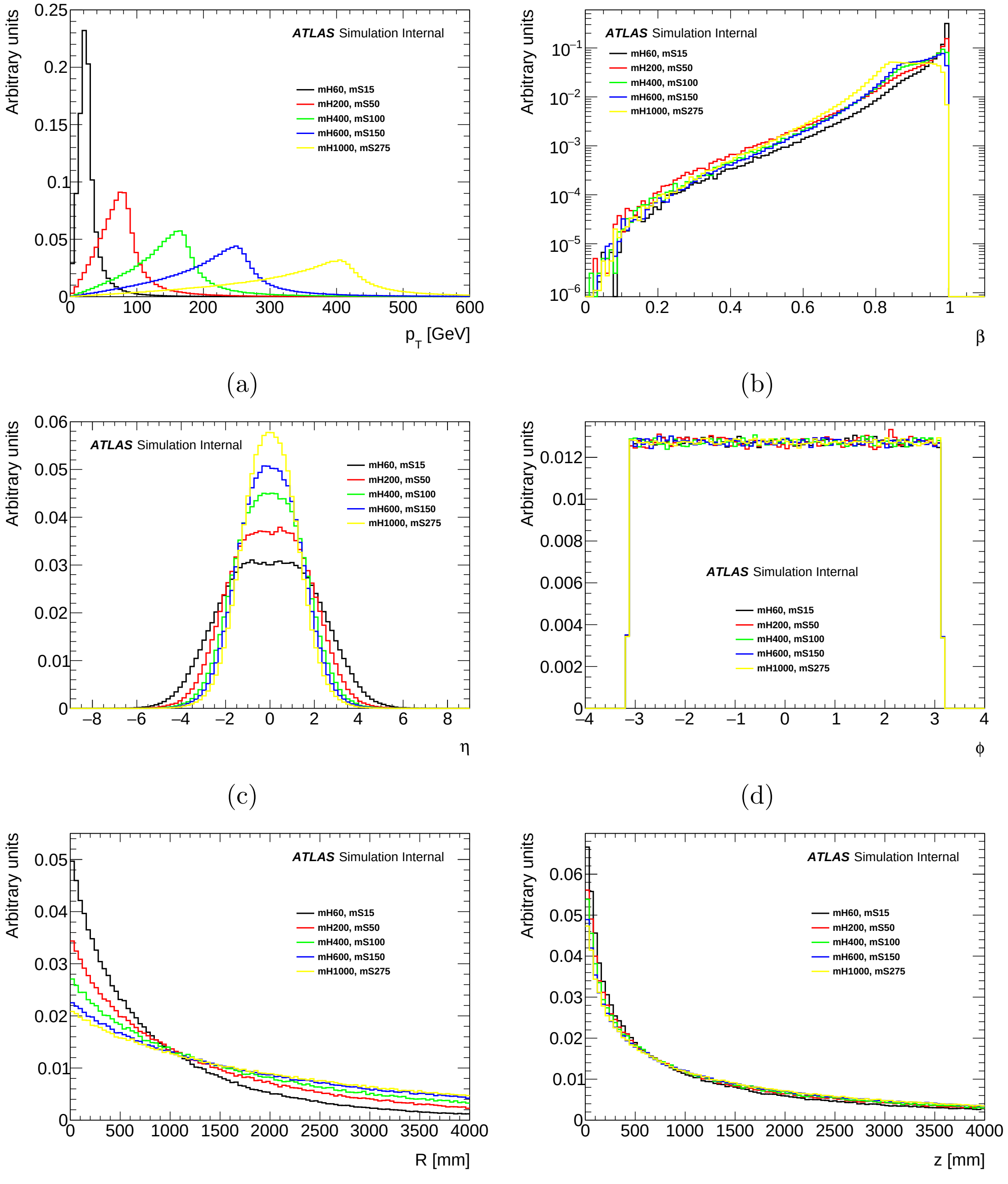

(a) (b)

(c) (d)

(e) (f)

Figure 4.2: Truth-level distributions of some of the key variables obtained from the generated HSS MC samples where $m_{\Phi} \neq 125$ GeV.

Chapter 5

Reconstruction

When a trigger is fired, all detector information from that event is saved. A set of standard reconstruction algorithms is then run on the raw hit information with the goal of creating a complete picture of what happened in the collision. What particles were created? What were their energies, their trajectories? Did they decay? What were the decay products, and their energies and trajectories? From the activity in each part of the ATLAS detector, particles can be identified and their momenta calculated. This identification is illustrated in fig. 5.1.

Beyond the identification and reconstruction of standard SM objects – photons, electrons, neutrons, etc. – there are also algorithms designed to search for the signatures of BSM particles. The search described in this thesis relies on one such algorithm reconstructing displaced hadronic decays in the muon spectrometer, which is described in section 5.4. Since this search relies so heavily on the muon spectrometer, it is instructive to understand how muons are reconstructed. This is detailed in section 5.3. The search also makes use of reconstructed tracks in the ID and jets in the calorimeters, which are described in sections 5.1 and 5.2.

5.1 Track reconstruction

Reconstruction of charged-particle tracks in the ID is extremely challenging due to high occupancy, where separation of the charged particle trajectories can be on the order of the detector granularity. The reconstruction algorithm [42] begins with the clustering of raw

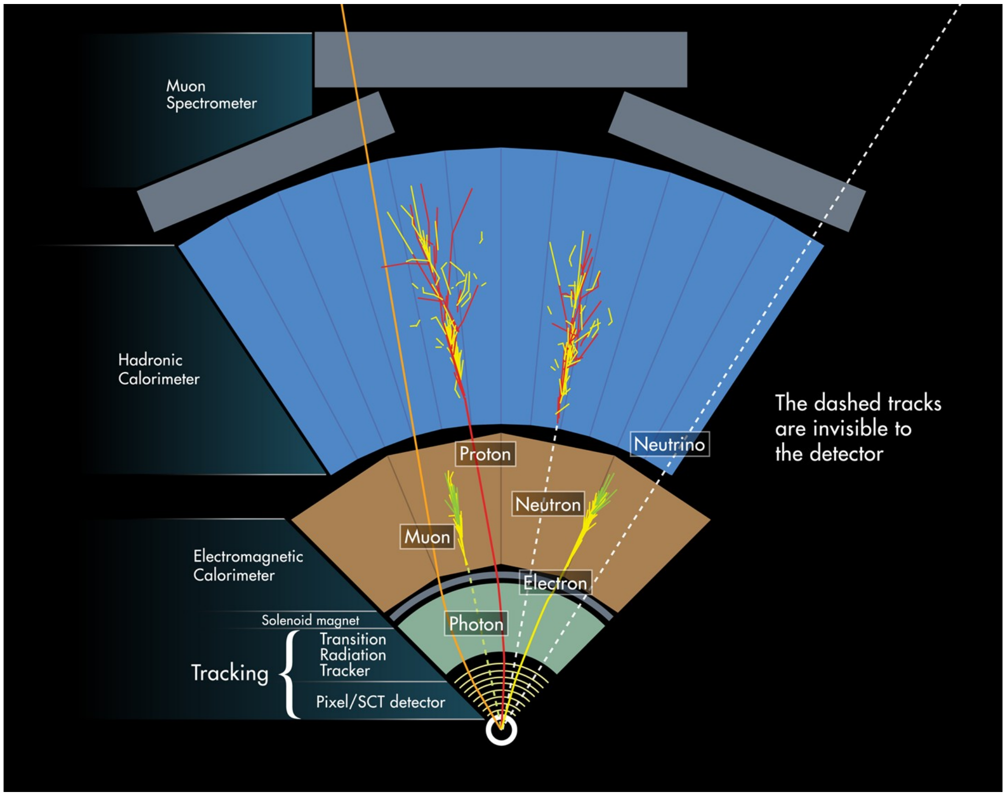

Figure 5.1: Example showing the detector signatures of some SM particles. Each signature is unique, allowing for identification of the particle. [41]

information from the pixel and SCT detectors, followed by iterative combinatorial track finding. Then ambiguity-solving of track candidates is implemented, and finally the tracks are extended into the TRT.

Pixels and strips with a common edge or corner are clustered if deposited energy is above a given threshold. A cluster provides a three-dimensional measurement called a *space-point* of where a charged particle crossed the ID sensor. In the case where one cluster is formed from the energy deposits of one particle, the cluster is known as a *single-particle* cluster. Otherwise, sometimes a single cluster can be formed where multiple particles traversed – this is called a *merged cluster*. It is important for reconstruction efficiency to quickly and correctly identify clusters as single-particle or merged. This is achieved with an artificial neural network (NN) that is trained to identify merged clusters using information on measured charge, the relative positions of pixels inside a cluster, and the particle's incident angle. The NN has 90% efficiency for identifying merged clusters created from two charged particles, and 85% efficiency for identifying clusters created from three or more charged particles.

Three space-points – measured in the SCTs, the pixels, or a mix of the two – can be combined to form a track seed, which already enables a first, approximate momentum measurement. A fourth space-point is required to be consistent with the trajectory of the track reconstructed from the seed. The trajectory must also be consistent with having originated from the interaction point; the location of the particle's creation is estimated with respect to the center of the interaction region by assuming a perfectly helical trajectory in a uniform magnetic field.

These initial requirements increase the *purity* of the track candidates, or the fraction of candidates that result in a good reconstructed track. The track candidates are built with a combinatorial Kalman filter [43] which includes further space-points in the pixels and SCTs that are consistent with the seed's initial calculated trajectory. Often a hit will be assigned to multiple track candidates or incorrectly assigned to the wrong track, which necessitates the ambiguity-solving algorithm.

The candidates are given a track score, which ranks the tracks in terms of their estimated quality. A track seeded from three SCT hits gets a higher contribution to the track score than one seeded from three pixel hits. A track seeded from three pixel hits, in turn, gets a higher contribution than one seeded from a mix of pixel and SCT hits. Holes, where the track intersects a detector element but no hit is registered in that detector, reduce the track score. A χ^2 fit is calculated for each track, and a poor fit will also reduce the track score. Tracks with incorrectly assigned hits tend to have low p_T, so high-p_T tracks also get a favorable contribution to the track score.

The tracks are ordered according to the track score and the ambiguity solver is used to assess clusters that are assigned to multiple track candidates. Shared clusters can be assigned to a maximum of two tracks, with preference given to the track candidates with highest track score.

5.1.1 Primary vertex

The primary vertex (PV) of an event is defined as the point where a pp hard scatter occurred. With the high luminosity and pileup conditions at the LHC, there are often multiple hard scatter interactions per event, in which case the PV is taken to be the one with the highest p_T. The reconstruction and identification of the PV is performed with tracks that fulfill the following conditions:

- $p_T > 400$ MeV
- $|\eta| < 2.5$
- Number of silicon hits ≥ 9 (11) if $|\eta| < 1.65$ ($|\eta| > 1.65$)
- At least one hit in the first two pixel layers
- Maximum 1 shared module (1 shared pixel hit or 2 shared SCT hits)
- 0 pixel holes
- Maximum 1 SCT hole

The PV must be reconstructed from at least two of these tracks. More details are given in Ref. [44].

5.2 Jet reconstruction

When a quark or gluon is produced in a collision, it cannot remain in a free state due to confinement and therefore undergoes *hadronization*, where a shower of hadrons is formed by creating quark-antiquark pairs and sometimes gluons from the vacuum. This cone of hadronic activity is called a jet.

Analogous to the silicon clusters formed in track reconstruction, topologically connected calorimeter cells with significant activity are clustered and provided as inputs to the anti-k_t jet reconstruction algorithm with a radius parameter of $\Delta R = 0.4$. This algorithm was designed to be infrared and collinear safe, and a full description can be found in Ref. [45].

The algorithm begins by calculating the distances d_{ij} between all input cluster objects (referred to as particles, or pseudojets) i and j:

$$d_{ij} = \min\left(1/k_{ti}^2, 1/k_{tj}^2\right) \frac{\Delta_{ij}^2}{R^2} \tag{5.1}$$

where $\Delta_{ij}^2 = (y_i - y_j)^2 + (\phi_i^2 - \phi_j)^2$, and k_{ti}, y_i and ϕ_i are the transverse momentum, rapidity, and azimuthal angle of particle i. The distances between each of those object and the beamline, d_{iB}, are also calculated using eq. (5.1) where the beamline B takes the place of particle j. Then the algorithm identifies the minimum distance from the set of all d_{ij} and d_{iB} values.

When this minimum distance is some d_{ij}, the clusters i and j are merged into a single object and returned to the list of inputs. When the smallest distance is d_{iB} instead, cluster i is identified as a jet and removed from the list of inputs. This procedure is iterated until no distance d_{ij} is smaller than d_{iB}, and all input objects have been resolved into jets.

Jet structure depends on many things, including the kinematics and multiplicity of the jet constituents and which parton initiated the hadronization (referred to as the *flavor* of the jet). Usually, a jet will consist of an energetic core, which means that $20-30\%$ of the jet's energy is often deposited in a single cluster.

5.2.1 Jet calibration

Jets are initially calibrated to the electromagnetic (EM) energy scale, which means that energy deposits are assumed to come from electromagnetic showers.

Corrections must be applied to the measured jet energies because the calorimeters, as described in section 3.2.2, will only measure the energy deposited in their active materials. The fraction of energy that is deposited before the calorimeters or in the passive layers will not be captured, and it varies based on the η and ϕ of the jet due to the physical layout of the detector. Calibration also takes into account signal losses that occur during clustering and reconstruction due to noise thresholds and particle reconstruction efficiencies. These factors are contained in a correction called the jet energy scale (JES). A further calibration, called global sequential calibration (GSC), corrects for the energy fluctuations that occur when there is a hadronic rather than purely electromagnetic shower. Further details can be found in Ref. [46, 47].

5.3 Muon reconstruction

Muons originating from the interaction point leave a unique signature in the ATLAS detector. They are charged particles, so they leave a track in the ID. Unlike other charged particles, however, they deposit very little energy into the calorimeters and continue on to leave a track in the muon spectrometer as well. The crux of muon identification, then, is to match a reconstructed track in the MS with its associated track in the ID. This is not entirely straightforward since the muon experiences a magnetic field between the ID and the MS, so its trajectory is bent.

The passage of a muon through the ID is reconstructed like any other ID track, as described in section 5.1. In the MS, hit patterns seed the reconstruction of straight-line segments within each muon chamber. The segments from different layers are combined to form a full muon track. This combination step starts with segments in the middle layer. Segments in the inner and outer layers are then considered as potential matches to the middle segments. These segments must pass requirements on hit multiplicity and fit quality, and they must have a position and direction that is compatible with the middle segment to be added to the track candidate. The same segment may be used to build several track candidates, but an overlap removal algorithm ensures that that segment is shared by a maximum of two final muon tracks. A track candidate is accepted when a global χ^2 fit of all hits associated with the candidate passes the selection criteria.

Several algorithms are used to maximize the acceptance and efficiency of muon reconstruction. These algorithms result in four types of reconstructed muons:

- Combined (CB) muons are formed when an MS track is extrapolated inwards and successfully matched with an ID track using a global fit. This strategy is referred to as "outside-in". Another strategy of combination, "inside-out", is sometimes used where ID tracks are extrapolated outwards to be matched with MS tracks.

- Segment-tagged (ST) muons have an ID track that is combined with at least one MS segment. This type might be reconstructed if the muon trajectory only crosses a single chamber layer in the MS, meaning a full MS track cannot be reconstructed.

- Calorimeter-tagged (CT) muons have an ID track matched to an energy deposit in the calorimeter that is compatible with a minimum-ionizing particle. This type can be used in areas where the MS does not have full coverage, for example the region $\eta < 0.1$ where there is an access shaft allowing service to the solenoid magnet, calorimeters, and ID.

- Extrapolated (ME) muons have an MS track that is not associated with an ID track, but does have a trajectory that is loosely compatible with the collision point. This is useful in the forwards region since the ID provides tracking up to $\eta < 2.5$ but the MS has coverage up to $\eta < 2.7$.

Once reconstructed, muons are then classified in terms of quality as *loose*, *medium*, or *tight*. These classifications are inclusive, so tight muons are a subset of medium muons and medium muons are a subset of loose muons. Medium muons are the standard quality used by most physics analyses.

The medium selection draws from CB and ME muons. CB muon tracks must have at least 3 MDT hits in at least 2 layers of MDT chambers, unless they are within $\eta < 0.1$, in which case one layer is acceptable if there is no more than one MDT hole layer. ME muon tracks are accepted only in the region $2.5 < \eta < 2.7$, and they must have at least 3 MDT or CSC layers. In all cases, the ID and MS tracks must have loosely compatible momentum measurements. "Compatible" momentum measurements are quantified in terms of *q/p significance*, which is the absolute value of the difference between the ratio of the muon charge and momentum in the ID versus the MS, divided by the sum in quadrature of the uncertainties. For medium CB muons, this significance must be < 7.

Loose muons include the CB and ME muons that have passed the medium selection plus CT and ST muons that are in the region $\eta < 0.1$. Tight muons accept only CB muons whose tracks include at least two MS stations, and the χ^2 of the track must be < 8. Tight muons also impose cuts on q/p significance and on ρ', which is the absolute value of the difference between the tranverse momentum measurements in the ID and MS, divided by the transverse momentum of the combined track. These cuts vary as a function of p_T.

Efficiency of muon reconstruction is shown in fig. 5.2a for loose, medium, and tight muons as a function of η, and the efficiency of medium muon reconstruction is shown in fig. 5.2b as a function of p_T.

Further information for muon reconstruction and performance can be found in Ref. [48, 49].

5.4 MS vertex reconstruction

The muon spectrometer is designed to reconstruct muon tracks with highly precise position and momentum measurement, as described in the previous section. The hadronic decay of a long-lived particle in the muon spectrometer gives a drastically different signature than a clean muon track, so a different algorithm was required to reconstruct the vertex from such a decay. The MS is not designed for this usage, so the position and momentum precision

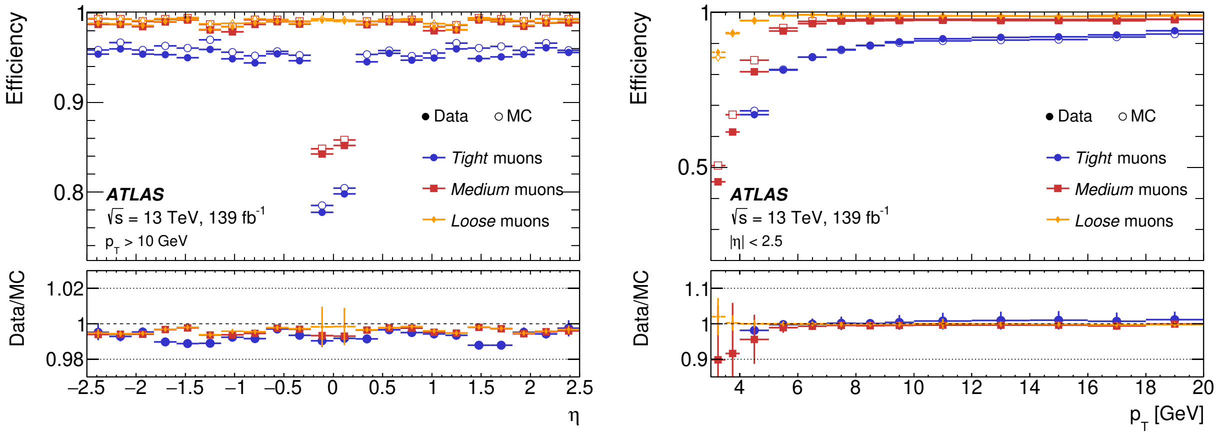

(a) (b)

Figure 5.2: Muon reconstruction efficiency as measured in (a) $Z \to \mu\mu$ events as a function of η and (b) $J/\psi \to \mu\mu$ events as a function of p_T [48].

that can be achieved is much lower than for a muon originating at the IP. This is not a significant concern, however, because the algorithm is only used in the search for long-lived particles, where discovery is the primary concern and precision measurement is secondary. In fact, the algorithm has been deliberately tuned to maximize overall vertex reconstruction efficiency rather than position resolution. A full description of the MS vertex reconstruction algorithm can be found in Ref. [50].

5.4.1 Tracklet reconstruction

The MS vertex reconstruction algorithm takes advantage of the spatial separation of MDT chambers. As described in section 3.2.3, each MDT chamber is composed of two *multilayers*, where each multilayer is itself composed of 3 to 4 rows of drift tubes.

The MDT tubes are uniquely numbered within the multilayer as illustrated in fig. 5.3. MDT hits are sorted in order of increasing tube number. Three hits within the multilayer form a seed when they fulfill the following criteria:

- Hits 1 and 2 are in the same or sequential layers
- Hit 3 is in the same layer or one higher than hit 2, but not in the same layer as hit 1
- In the barrel, $|z_1 - z_2| < 50$ mm and $|z_1 - z_3| < 80$ mm
- In the endcaps, $|R_1 - R_2| < 50$ mm and $|R_1 - R_3| < 80$ mm

where $R = \sqrt{x^2 + y^2}$ is measured in the local coordinate system with its origin at one corner of the MDT chamber.

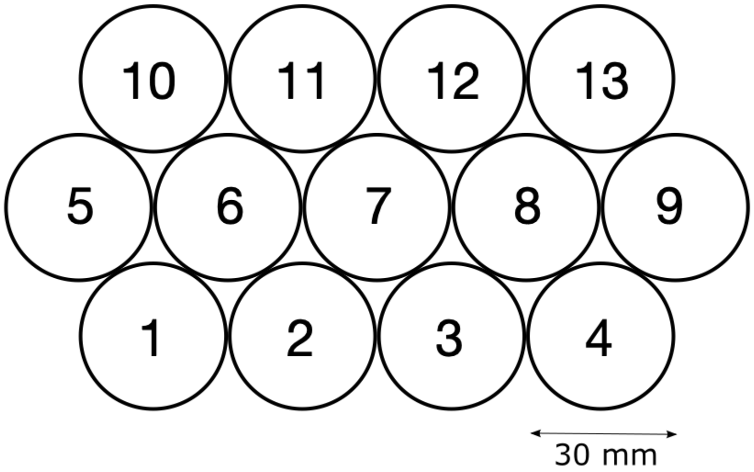

Figure 5.3: Illustration of the MDT tube numbering scheme within a single multilayer.

A study on the MDT hit patterns accepted as tracklet seeds is detailed in appendix A. From these seeds, straight-line MS segments are reconstructed in each multilayer using a minimum χ^2 fit. All combinations of MS segments from multilayer 1 (ML1) and multilayer 2 (ML2) are considered and parameters Δb and $\Delta\alpha$ are calculated for each combination, as seen in fig. 5.4. Δb is the minimum distance between the two MS segments at the midline between the two MLs, and $\Delta\alpha$ is the difference in angle between the two MS segments. If the combination of MS segments passes the cuts on Δb and $\Delta\alpha$ specified in table 5.1, it is considered a *tracklet*. The angular uncertainty of tracklets was determined using a simulated sample of muons with momentum 1 TeV, which have straight trajectories in the MDT chambers; from this the RMS values of $\Delta\alpha$ and Δb were determined to be 4.3 mrad and 1.0 mm, respectively.

The selection criteria is different between the barrel and the endcaps due to the magnitude of the magnetic field in each region. In the endcaps the magnetic field is always small within the MDT chambers, so it is assumed the particle will experience negligible bending in its trajectory. Therefore the allowed angle between MS segments is quite small, and the tracklets that do pass the cut are then refit as a straight line through both MLs.

Since the tracklets in the barrel are reconstructed with bending, a momentum measurement can be made using the equation $p = k/|\Delta\alpha|$ where k is a chamber-dependent parameter. Then the uncertainty in the momentum measurement, following from the tracklet $\Delta\alpha$ un-

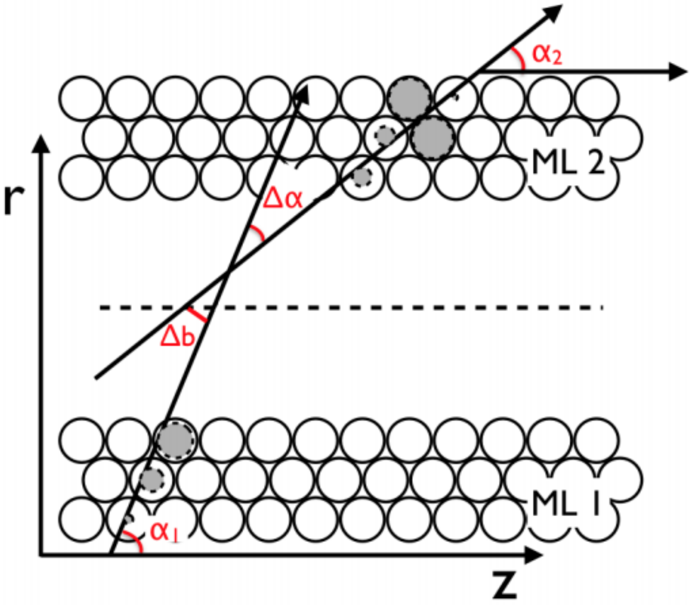

Figure 5.4: The combination of MS segments into tracklets uses the difference in angle between tracklets, $\Delta\alpha$, and the distance between tracklets in z, Δb, as parameters.

Chamber type	Number of layers	ML spacing (mm)	$\lvert\Delta\alpha_{\text{max}}\rvert$ (mrad)	$\lvert\Delta b_{\text{max}}\rvert$ (mm)	Refit
BIS	4	6.5	12	3	Always
BIL	4	170	36	3	if $\lvert\Delta\alpha\rvert < 12$ mrad
BMS	3	170	67	3	if $\lvert\Delta\alpha\rvert < 12$ mrad
BML	3	317	79	3	if $\lvert\Delta\alpha\rvert < 12$ mrad
BOS	3	317	12	3	Always
BOL	3	317	36	3	if $\lvert\Delta\alpha\rvert < 12$ mrad
Endcap	3	170	12	3	Always

Table 5.1: Selection criteria for MS segments when forming tracklets.

certainty, is approximately $\sigma_p/p \approx 0.06 \cdot p/\text{Gev}$ in the BML chambers, $\sigma_p/p \approx 0.08 \cdot p/\text{Gev}$ in the BMS chambers, and $\sigma_p/p \approx 0.13 \cdot p/\text{Gev}$ in the BOL and BIL chambers.

5.4.2 Vertex reconstruction

Once MS tracklets are reconstructed, they are used as inputs to the MS vertex reconstruction algorithm. Again this algorithm differs between the barrel and endcaps, however in both regions it adheres to the following general procedure:

1. Tracklets are clustered using a cone algorithm, where the cone has radius $\Delta R = 0.6$ and points back to the IP.
2. Using trigger hits in addition to the tracklets, the LLP flight trajectory is calculated in η and ϕ.
3. The clustered tracklets are mapped onto the $r - z$ plane defined by the ϕ line-of-flight calculated in step 2.
4. The tracklets are back-extrapolated to find the vertex position.

The difference in how the vertex reconstruction is performed arises only in the last step of the procedure, other than the fact that "trigger hits" refers to RPC hits in the barrel and TGC hits in the endcaps in step 2. The mapping of the tracklets into a single $r - z$ plane is necessary because the resolution of the ϕ coordinate is too coarse to be useful.

In the barrel, the back-extrapolation of the tracklets must take into account the inhomogeneous magnetic field present in this region. To that end, the tracklets are extrapolated to a series of lines of constant radius, as seen in fig. 5.5, using the full magnetic field map. These lines are equally spaced in the range $r = 3.5$ m to $r = 7$ m. The spacing is taken to be every 25 cm along the line-of-flight, which means the number of lines of constant radius used in the extrapolation procedure varies according to the angle of the line-of-flight with respect to the z-axis. At $\eta = 0$, 15 lines are used; at $\eta = 1$, 22 lines are used. At each line of constant radius, the z position of the extrapolated tracklet is calculated.

There is an uncertainty on the extrapolated z position due to the imprecision with which the ϕ coordinate is known, leading to an imprecision in the magnetic field that is experienced. This uncertainty is calculated by rotating the $r - z$ plane used during the procedure by 200 mrad (which corresponds to about $\frac{1}{2}$ of a large MDT chamber, and therefore the maximum variation in position from the center of a chamber), extrapolating the tracklet again, and taking the difference in z position between the nominal and rotated plane configurations. To assign the total position uncertainty σ_z at the line of constant radius, this uncertainty associated to the magnetic field is added in quadrature to the uncertainty in the tracklet's momentum measurement.

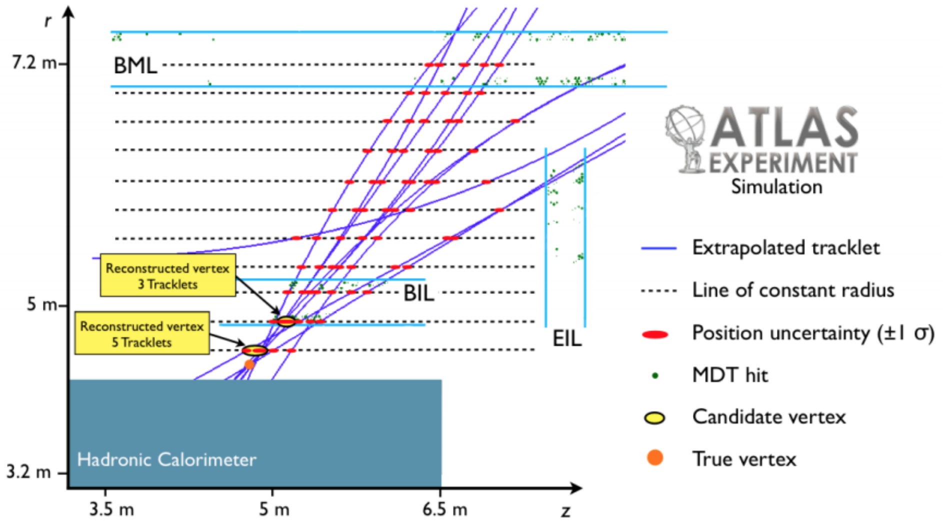

Figure 5.5: Backwards extrapolation procedure of tracklets to reconstruct vertices in the barrel.

At each line of constant radius, a candidate vertex position is calculated to be the average z position of the extrapolated tracklets, where each tracklet is weighted by $1/\sigma_z^2$. Assuming all tracklets originate from this vertex, its χ^2 probability is calculated. If the probability is less than 5%, the tracklet with the greatest contribution to the χ^2 is dropped and the χ^2 is recalculated. This process repeats until the χ^2 probability is found to be greater than 5% or there are fewer than 3 tracklets left. The final vertex is chosen as the candidate vertex with χ^2 probably greater than 5% and the highest number of associated tracklets. If multiple candidate vertices have the same number of associated tracklets, the vertex with the smallest χ^2 is chosen. This ensures that the final vertex position is as close to the LLP decay truth position as possible.

The back-extrapolation in the endcaps is similar in spirit to that in the barrel, seen in fig. 5.6, with the simplification that no magnetic field needs to be taken into account so the tracklets are extrapolated as straight lines. Each tracklet has an equation $\beta = -r\tan(\alpha) + z$ where β is the z-intercept and α is the angle of the tracklet. The equations for all clustered tracklets are used in a least-squares regression fit to solve for the vertex position. This is iterated by dropping the tracklet farthest from the vertex position and refitting, until all tracklets have a distance of closest approach of less than 30 cm from the vertex or there are fewer than 3 tracklets left.

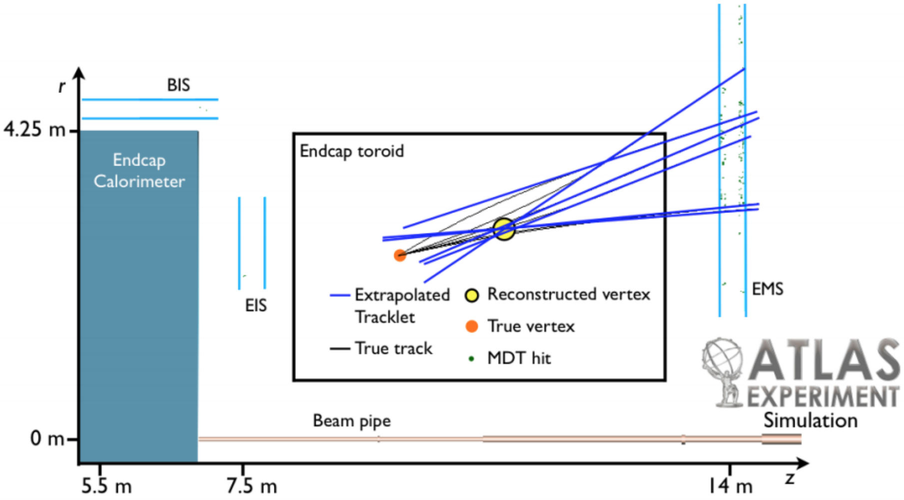

Figure 5.6: Backwards extrapolation procedure of tracklets to reconstruct vertices in the endcaps.

5.4.3 Good vertex criteria

A set of *good vertex criteria* (GVC) was established in order to maximize the acceptance of signal vertices while minimizing the acceptance of vertices reconstructed from background activity. The distributions of several key variables were studied to find the optimal cuts to apply. These fall into two main categories: hits associated to the vertex, and variables related to isolation. The main background that these cuts aim to reject is vertices from punch-through jets, so a comparison between signal samples and QCD multijet samples is made. Distributions from data are also shown, as they further include non-collision backgrounds and it is instructive to see where their behavior diverges from that of the multijets. In both data and MC, vertices are required to pass the standard ATLAS event cleaning (meaning the event has a good PV and all detector systems were fully operational) and either of the single jet triggers `HLT_j400` or `HLT_j420`. The events are also required to have exactly one reconstructed MS vertex.

The final GVC used in the analysis are summarized in table 5.3.

Hits associated to the vertex

A LLP decaying to hadronic jets in the MS leaves a flurry of activity that is not normally expected in that detector, since within the predictions of the SM it would only be visibly traversed by muons. This signal activity is often higher than the average activity left by a punch-through jet as well, depending on the signal mass point, since that jet has already deposited much of its energy in the calorimeters by the time it reaches the MS. Thus a minimum number of MDT and RPC/TGC hits associated to the vertex is introduced. This has an additional use of removing vertices reconstructed from noise bursts in the MDTs, as these bursts are unlikely to happen coherently with significant activity in the RPCs or TGCs. A vertex is required to have at least 300 MDT hits associated to it and at least 250 RPC hits if it is in the barrel, or similarly at least 250 TGC hits if it is in the endcaps. The acceptance of vertices as a function of the GVC hit cut are seen in fig. 5.7, where the cut used in the analysis is indicated with a dashed vertical line.

A cut on the maximum number of MDT hits associated to the vertex is also imposed at 3000 in order to remove vertices reconstructed from noise bursts. The acceptance of vertices as a function of this upper hit cut are seen in fig. 5.8, where the cut used in the analysis is again indicated with a dashed vertical line.

Isolation variables

The isolation of a vertex quantifies the angular distance from the MS vertex to any preceding track or jet activity. This is one of the most powerful discriminating variables between signal and background because the majority of non-signal vertices are reconstructed from punch-through jet activity, meaning there will be significant activity present in the ID and/or calorimeters pointing directly at the reconstructed MS vertex.

A cone is defined from the PV to the MS vertex with some radius ΔR. If a significant amount of activity is present within this cone (measured in terms of p_T for tracks and energy for jets), then the vertex is determined to be non-isolated and originating from background sources.

The value of ΔR and the amount of activity considered to be "significant" varies according to the kind of activity that is being considered: jets, low-p_T tracks, or high-p_T tracks. Studying the activity from many low-p_T tracks as well as from singular high-p_T tracks ensures that the isolation is collinear-safe. Jets considered during vertex isolation also need to pass the quality cuts summarized in table 5.4. The Jet Vertex Tagger (JVT) is a standard ATLAS discriminant used to identify and suppress pileup jets [51]. The quantity $\log(E_{\mathrm{HAD}}/E_{\mathrm{EM}})$ measures the comparative fraction of jet energy that is deposited in the ECal versus the

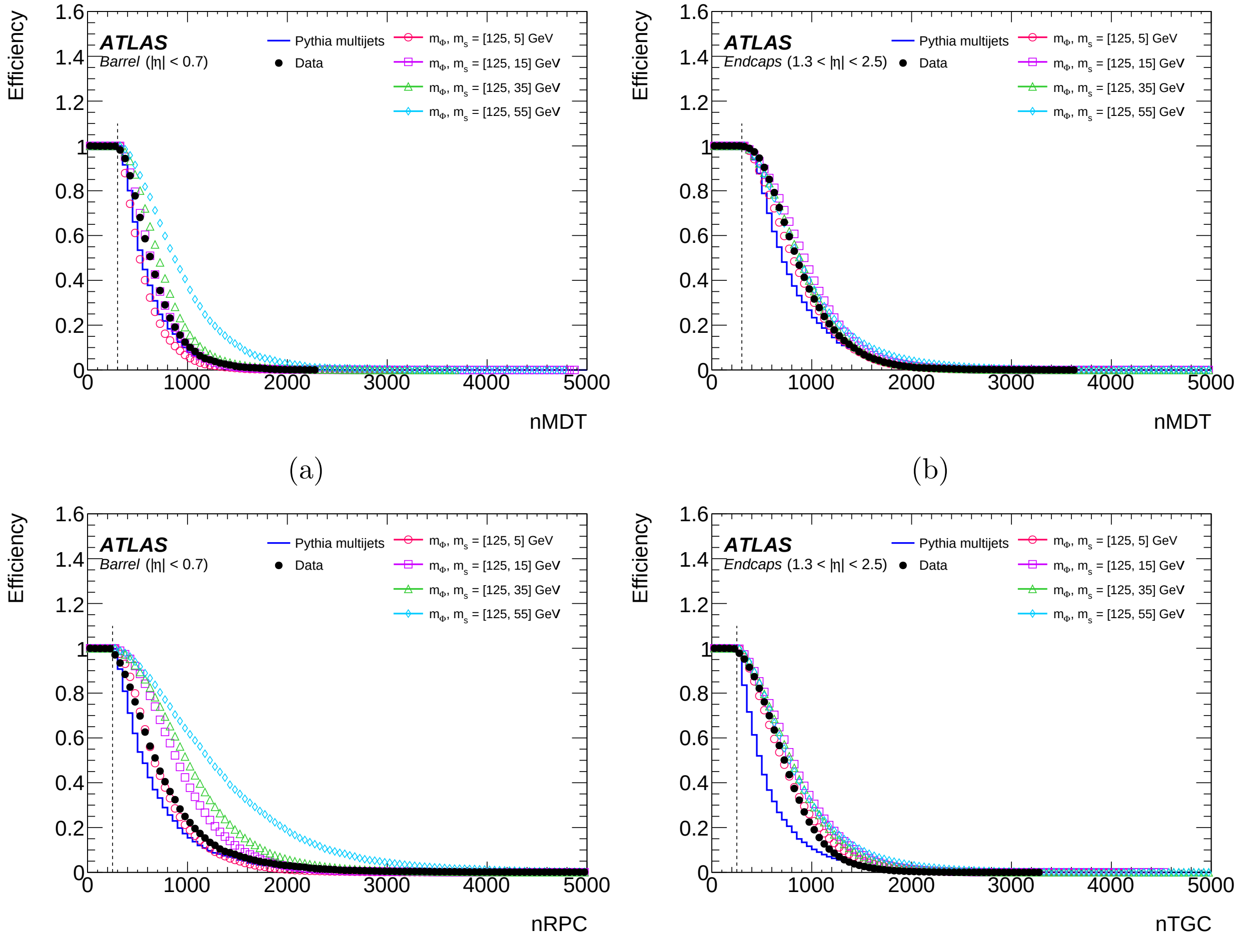

(a) (b)

(c) (d)

Figure 5.7: Good vertex criteria distributions in data, multijet MC, and select signal MC samples showing the efficiency of MS vertices passing cuts with respect to the minimum number of associated (a) MDT hits in the barrel, (b) MDT hits in the endcaps, (c) RPC hits in the barrel, and (d) TGC hits in the endcaps.

HCal. This ensures that the analysis does not reject vertices that are reconstructed from LLP decays that occur at the end of the HCal.

Acceptance of vertices as a function of these isolation variables – the ΔR of the isolation cone, and the energy/p_T of the activity within it – is shown in figs. 5.9 to 5.11. The distributions are plotted separately between barrel and endcaps. The cuts used in the analysis are indicated with a dashed vertical line.

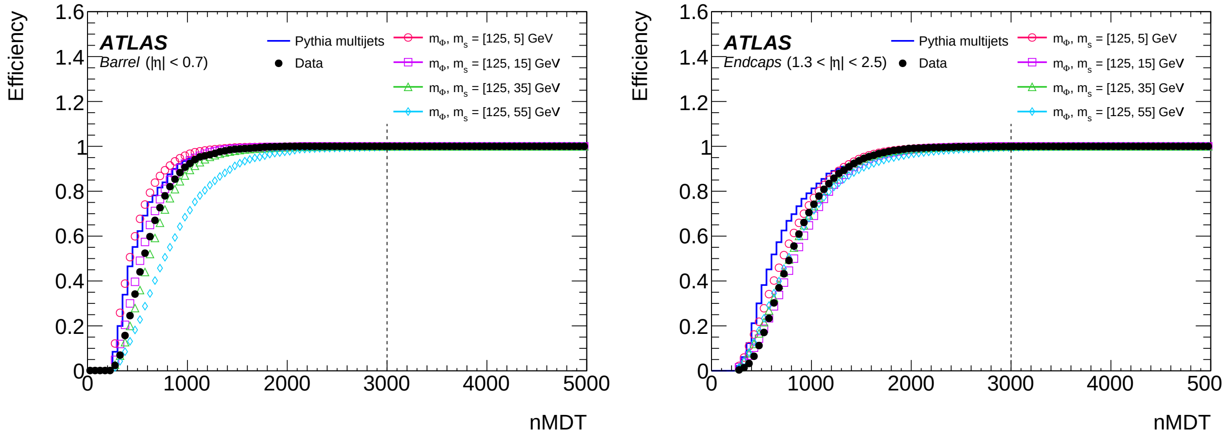

(a) (b)

Figure 5.8: Good vertex criteria distributions in data, multijet MC, and select signal MC samples showing the efficiency of MS vertices passing cuts with respect to the maximum number of associated MDT hits in the (a) barrel and (b) endcaps.

Table 5.2: Summary of criteria for good MS vertices in the barrel and endcap regions.

Requirement	Barrel	Endcap
MDT hits	$300 \leq n_{\text{MDT}} < 3000$	$300 \leq n_{\text{MDT}} < 3000$
RPC/TGC hits	$n_{\text{RPC}} \geq 250$	$n_{\text{TGC}} \geq 250$
> 5 GeV track isolation	$\Delta R > 0.3$	$\Delta R > 0.6$
Track $\lvert\Sigma \vec{p_T}\rvert$ in 0.2 cone	< 10 GeV	< 10 GeV
> 30 GeV jet isolation	$\Delta R > 0.3$	$\Delta R > 0.6$

Table 5.3: Summary of criteria for good MS vertices in the barrel and endcap regions.

Requirement	Barrel	Endcap
> 5 GeV track isolation	$\Delta R > 0.3$	$\Delta R > 0.6$
Track $\lvert\Sigma \vec{p_T}\rvert$ in 0.2 cone	< 10 GeV	< 10 GeV
> 30 GeV jet isolation	$\Delta R > 0.3$	$\Delta R > 0.6$

Table 5.4: Description of the selection criteria for jets used in MS vertex isolation.

Level	Cut	Value
Jet selection	p_T	> 30 GeV
for vertex	$\log(E_{\text{HAD}}/E_{\text{EM}})$	< 0.5
isolation	JVT	JVT> 0.59 if jet p_T < 60 GeV

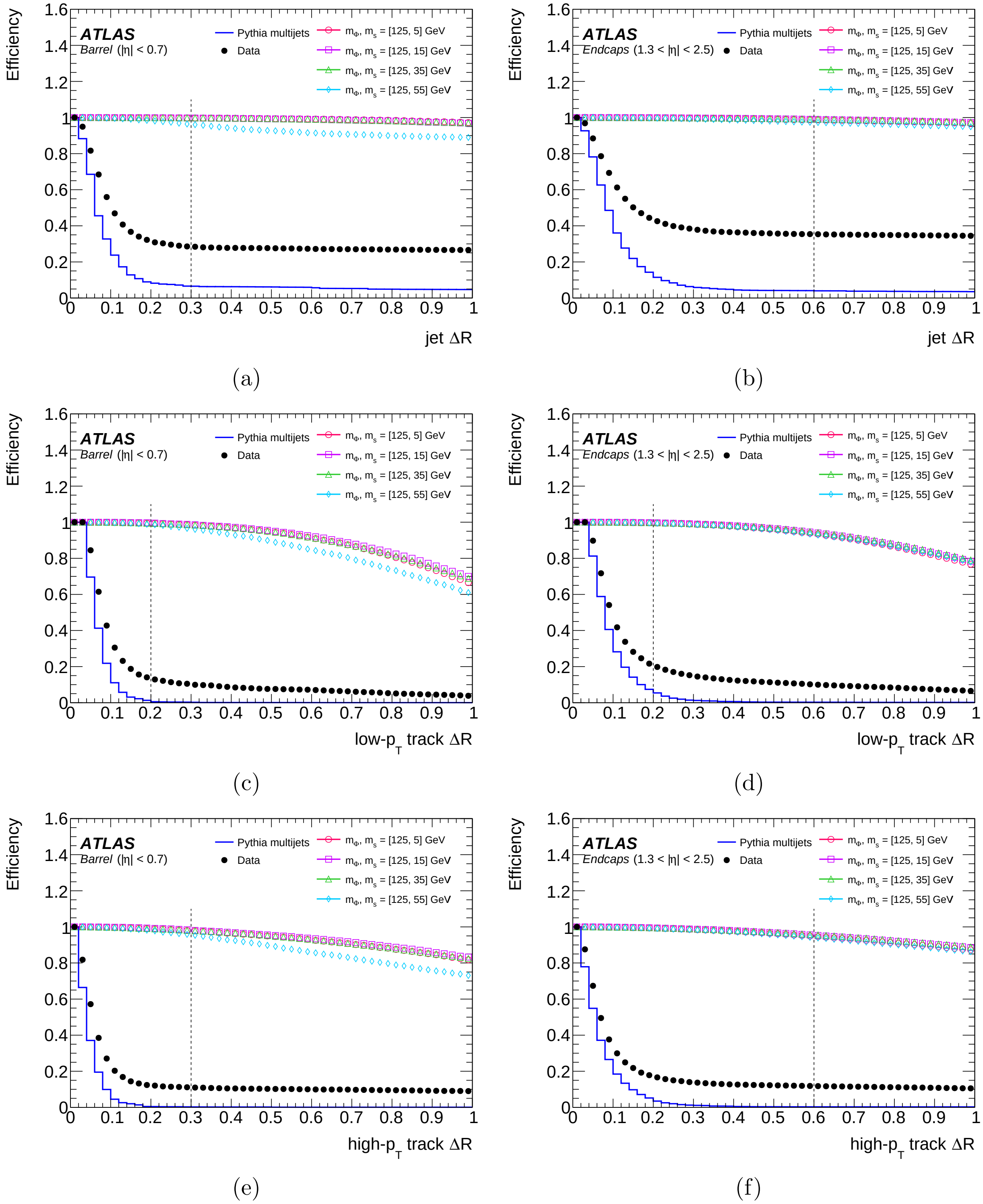

(a) (b) (c) (d) (e) (f)

Figure 5.9: Good vertex criteria distributions in data, multijet MC, and select signal MC samples showing the efficiency of MS vertices passing isolation cuts with respect to (a) jets in the barrel, (b) jets in the endcaps, (c) the sum of low-p_T tracks in the barrel, (d) the sum of low-p_T tracks in the endcaps, (e) high-p_T tracks in the barrel, and (f) high-p_T tracks in the endcaps, as a function of the selected ΔR. The vertical dashed line shows the ΔR cut value that is used in the analysis.

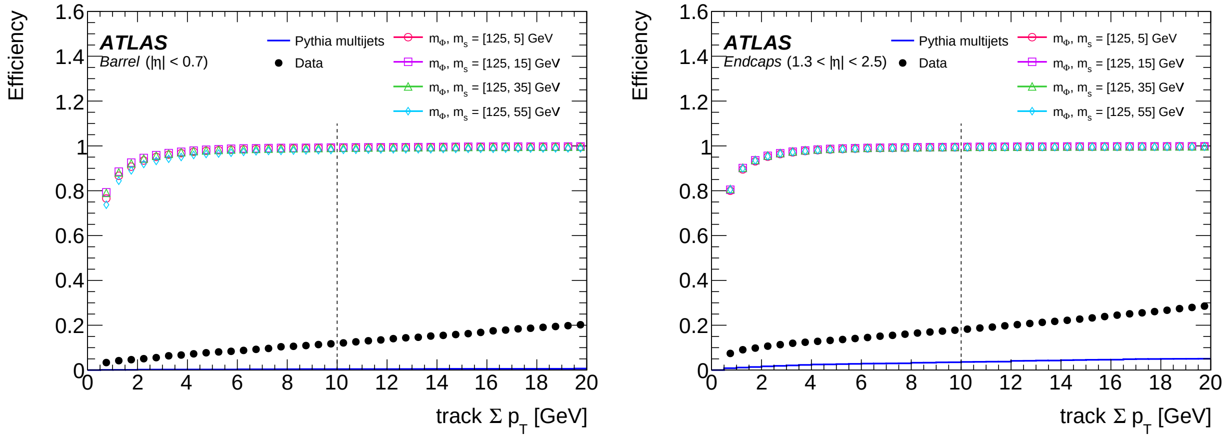

(a) (b)

Figure 5.10: Good vertex criteria distributions in data, multijet MC, and select signal MC samples showing the efficiency of MS vertices passing isolation cuts where the sum of low-p_T tracks in a $\Delta R = 0.2$ cone around the vertex direction in the (a) barrel and (b) endcaps must be less than the specified cut in p_T. The vertical dashed line shows the ΔR cut value that is used in the analysis.

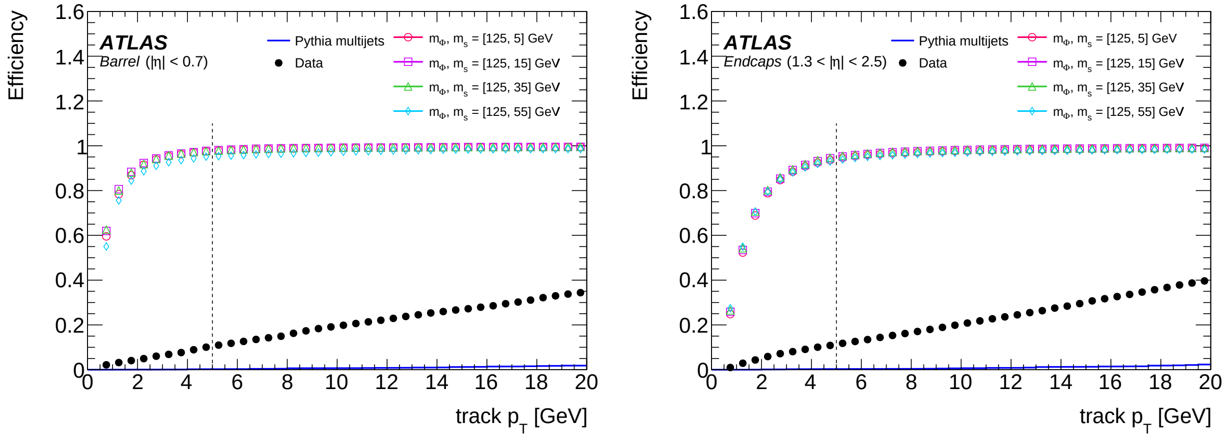

(a) (b)

Figure 5.11: Good vertex criteria distributions in data, multijet MC, and select signal MC samples showing the efficiency of MS vertices passing isolation cuts where high-p_T tracks in the (a) barrel and (b) endcaps must be less than the specified cut in p_T. The vertical dashed line shows the ΔR cut value that is used in the analysis.

Chapter 6

MS Trigger and Vertex Performance

It is crucial to understand the performance of the triggering and vertexing algorithms, as this is key to an accurate understanding of the signal acceptance and background rejection of the analysis. Performance is studied in several ways. First, the behavior of the physics objects used as inputs to the triggering and vertexing algorithms (*i.e.* muon RoIs and tracklets, respectively) is compared between data and MC in order to understand how well these objects are modeled in MC. Section 6.1 describes the study of muon RoIs to understand potential mismodeling in the trigger, followed by a description of trigger efficiency in section 6.2. Section 6.3 details the study of tracklets to understand potential mismodeling in the vertexing, section 6.4 describes vertex efficiency, and section 6.5 illustrates the accuracy of the reconstruction algorithm by comparing the position of the reconstructed vertex with the truth position of LLP decay.

The events used in these studies cannot be required to pass the muon RoI cluster trigger or have a vertex reconstructed in the MS, as these impose requirements on the number of RoIs/tracklets and would bias the results of the studies. Instead events with punch-through jets are considered, as punch-through is the only SM process originating from a pp collision that gives rise to a similar kind of high-activity hadronic shower in the MS as is expected for a LLP decay. Events that pass `HLT_j400` or `HLT_j420` triggers are used, which select jets with $pT > 400$ or 420 GeV, because jets must have significant p_T if they are able to traverse the calorimeters completely and still have remaining energy to punch-through into the muon spectrometer. A minimal dijet selection is then imposed:

- $p_T > 30$ GeV

- $\log(E_{\mathrm{HAD}}/E_{\mathrm{EM}}) < 0.5$
- JVT > 0.59 if jet $p_T < 60$ GeV

Only leading and subleading jets (meaning the jets with the highest and second-highest p_T in the event) are selected, since they are known to be well-modeled in the MC. Signal events have, on average, 50 muon segments reconstructed within a $\Delta R < 0.4$ cone of the reconstructed vertex, so to ensure that the event is as signal-like as possible, at least 50 muon segments are required to be reconstructed within a $\Delta R < 0.4$ cone of the punch-through jet.

6.1 Muon RoI mismodeling

Using events that pass the selection described above, mismodeling in the Muon RoI Cluster trigger is assessed by comparing the normalized distribution of the number of L1 muon RoIs within a $\Delta R = 0.4$ punch-through jet cone in data and MC. This is seen in fig. 6.1, plotted separately for the barrel and the endcaps, in addition to the data-MC ratio of the distributions. The normalized distribution of the number of muon RoIs found within a $\Delta R = 0.4$ MS vertex cone is shown in fig. 6.1 for a few select signal mass points, for comparison.

The vertical lines in figs. 6.1a and 6.1b indicate the cut on muon RoIs that is present at trigger level. To quantify the mismodeling between data and MC, the integral above this cut is calculated for both data and MC. The trigger mismodeling factor is defined to be the data/MC ratio of these integrals, as it gives an indication of how often a muon RoI will be reconstructed in data compared with MC. This mismodeling factor is 1.24 ± 0.01 in the barrel and 1.20 ± 0.01 in the endcaps. The difference between the two regions is not unexpected, as the detector technology used for triggering is different: RPCs provide the trigger in the barrel, and TGCs in the endcaps.

The mismodeling factor indicates that the detector is more efficient at reconstructing muon RoIs during data-taking than MC would predict. However the origin of the mismodeling is not well understood, therefore to be conservative the factors are not applied as corrections on the barrel and endcaps trigger efficiencies derived using signal MC. Instead it is applied as a systematic uncertainty of 24% in the barrel and 20% in the endcaps.

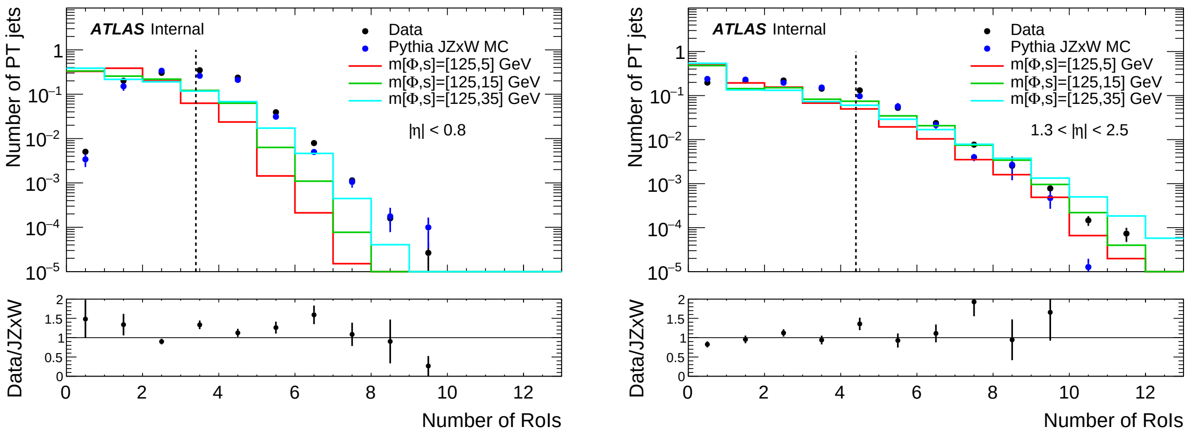

(a) (b)

Figure 6.1: Muon RoI distribution within $\Delta R = 0.4$ of the punch-through jet axis for barrel (a) and endcaps (b). The black dots show 2015-2018 data, the blue dots the dijets MC simulations, and the solid lines a few signal benchmark samples. The vertical lines show the cut applied at trigger level.

6.2 Trigger efficiency

The efficiency of the Muon RoI Cluster trigger is defined as the fraction of LLP decays that result in the trigger firing. This is derived from signal MC by dividing the number of triggering muon RoI clusters matched to a LLP by the total number of LLP decays. A cluster is considered “matched” to a LLP if its position is within a $\Delta R < 0.4$ cone of the LLP trajectory, where the position of the cluster is calculated to be the average of all the muon RoIs. LLPs are only considered for matching if their decay position is within the fiducial volume of the MS, as detailed in table 6.1.

The efficiencies are presented as a function of the LLP decay position in fig. 6.2, with detector boundaries indicated by dashed vertical lines. The shape of the efficiency distribution depends strongly on the mass and boost of the LLP. In all cases, a decay towards the end of the HCal will only occasionally produce enough activity in the MS to fire the trigger. The trigger efficiency is usually highest just after the first RPC/TGC station and decreases until the second RPC/TGC station; this is because the hadronic shower needs to develop for some distance (depending on the boost) before the decay products are spatially separated enough to form multiple muon RoI clusters. This is primarily because at level 1 the trigger requires 3 (4) RoIs in the barrel (endcaps), while only 2 RoIs can be reconstructed per sector. Therefore the decay products must be spread over at least two sectors to fire the trigger; when the LLP decays further towards the end of the MS, the decay products are often too collimated to achieve that much spread. This is especially true for highly boosted decays where the decay products tend to be more collimated. However, the argument does not hold true anymore when the LLP decay has extremely low boost, as the decay products can actually be too spatially separated. Then the activity is spread over a larger region than the trigger algorithm expects, and will not fulfill the minimum hit requirements within $\Delta R = 0.4$ of the central location of the clusters.

Detector	**Fiducial Volume**
MS barrel	$3\,\text{m} < L_{xy} < 8\,\text{m}$, $\lvert\eta\rvert < 0.7$
MS endcaps	$L_{xy} < 10\,\text{m}$, $5\,\text{m} < \lvert L_z\rvert < 15\,\text{m}$, $1.3 < \lvert\eta\rvert < 2.5$

Table 6.1: Fiducial volume definition for the MS barrel and endcaps regions.

6.3 Tracklet mismodeling

The MC mismodeling in the reconstruction of MS vertices is assessed by comparing the normalized distributions of the number of tracklets in the cone of a punch-through jet in data and MC, with the similar strategy used for the trigger RoIs. With the same selection of leading and subleading punch-through jets as described in section 6.1, fig. 6.3 presents the normalized distributions for the number of tracklets within a punch-through jet cone for barrel and endcaps. Data and MC distributions and their ratio are presented. Select signal samples are included for comparison.

The data/MC ratio of the integrals of the normalized distributions above the selection cut used at vertex reconstruction level (i.e. at least 3/4 tracklets in the barrel/endcaps) is 0.80 ± 0.01 in the barrel and 0.75 ± 0.01 in the endcaps. This provides a measure of how many more tracklets are found in the cone of a hadronic shower, on average, in MC compared to data. In this case, since the number of reconstructed tracklets is higher in MC than in data, the effect on vertex reconstruction efficiency can be estimated by artificially reducing the tracklet reconstruction in efficiency in MC to match that in data. The details of this are given in section 6.4.

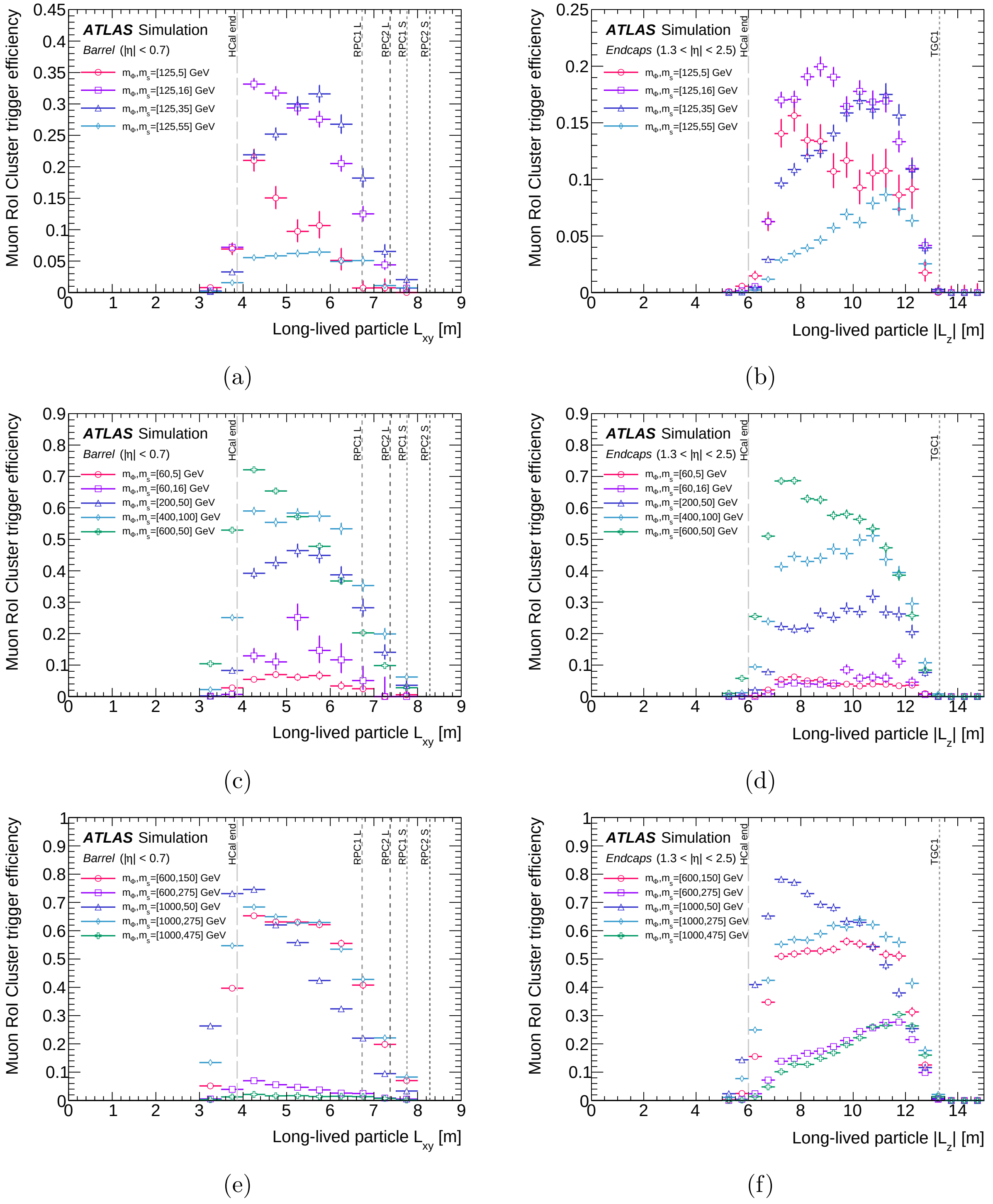

(a) (b) (c) (d) (e) (f)

Figure 6.2: Truth-based Muon RoI Cluster trigger efficiency for (a-b) HSS samples where $m_{\Phi} = 125$ GeV and (c-f) HSS samples where $m_{\Phi} \neq 125$ GeV. Plots on the left side are for the barrel, and those on the right side are for the endcaps.

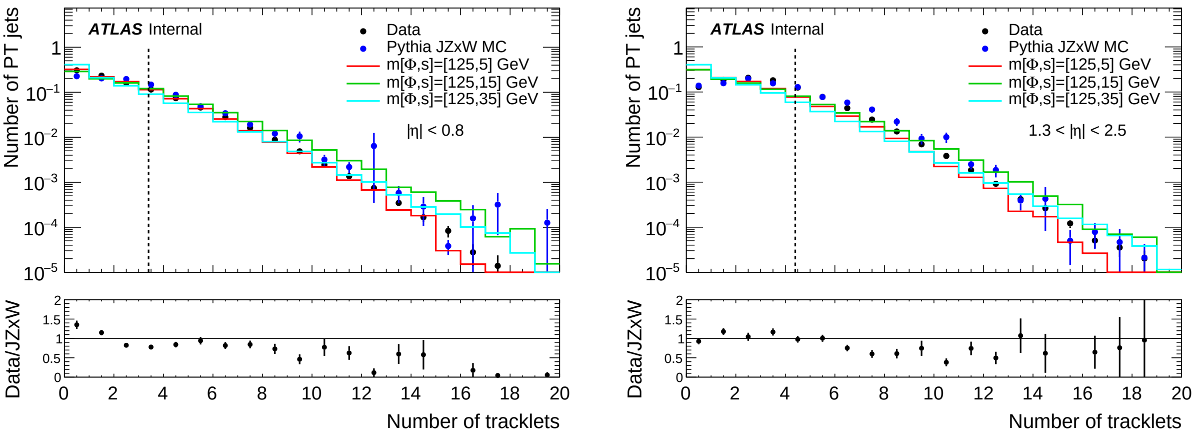

(a) (b)

Figure 6.3: Tracklets distribution within $\Delta R = 0.4$ of the punch-through jet axis for (a) barrel and (b) endcaps. The black dots show 2015-2018 data, the blue dots show dijet MC simulations, and the solid lines show some select signal samples. The vertical lines show the cut applied at vertex reconstruction level.

6.4 MS vertex reconstruction efficiency

The efficiency for the MS vertex reconstruction is defined as the fraction of simulated LLP decays in the MS fiducial volume that have a reconstructed vertex satisfying the GVC discussed in section 5.4.3.

The impact of the tracklet MC mismodeling is estimated by dropping the tracklets used to reconstruct the vertex according to the measured data-MC factor in the barrel and endcaps and counting the number of reconstructed vertices (i.e. vertices that have at least 3 (4) associated tracklets in the barrel (endcaps)). This is done by rerunning the vertex reconstruction on the MC ESD files that are stored during the MC production of the official samples. Figure 6.4 and fig. 6.5 show the efficiency variation for the nominal reconstruction and the reconstruction where the scale factors are applied. The efficiency variations for all signal mass points are detailed in tables 6.2 and 6.3. For simplicity, the final loss in efficiency is taken to be the average of the losses between all samples; as usual, this is calculated separately for the barrel and the endcaps. This is reported in the first column of tables 6.4 and 6.5. The barrel shows a much higher loss of efficiency than the endcaps (27% compared with 9.0%) – the reason for this is not entirely understood, but the difference is not necessarily unreasonable given the differences in vertex reconstruction between the two regions. For example, the barrel algorithm requires a minimum of 3 tracklets associated to the vertex, while the endcaps algorithm requires a minimum of 4 tracklets. Therefore, a vertex that is reconstructed with 3 (4) tracklets in the nominal reconstruction in the barrel (endcaps) will automatically fail to be reconstructed if one of its tracklets is randomly dropped when the SF is applied. A higher proportion of vertices in the barrel have 3 associated tracklets than vertices in the endcaps have 4 associated tracklets, therefore it is logical that the application of the SF has a more significant effect in the barrel region.

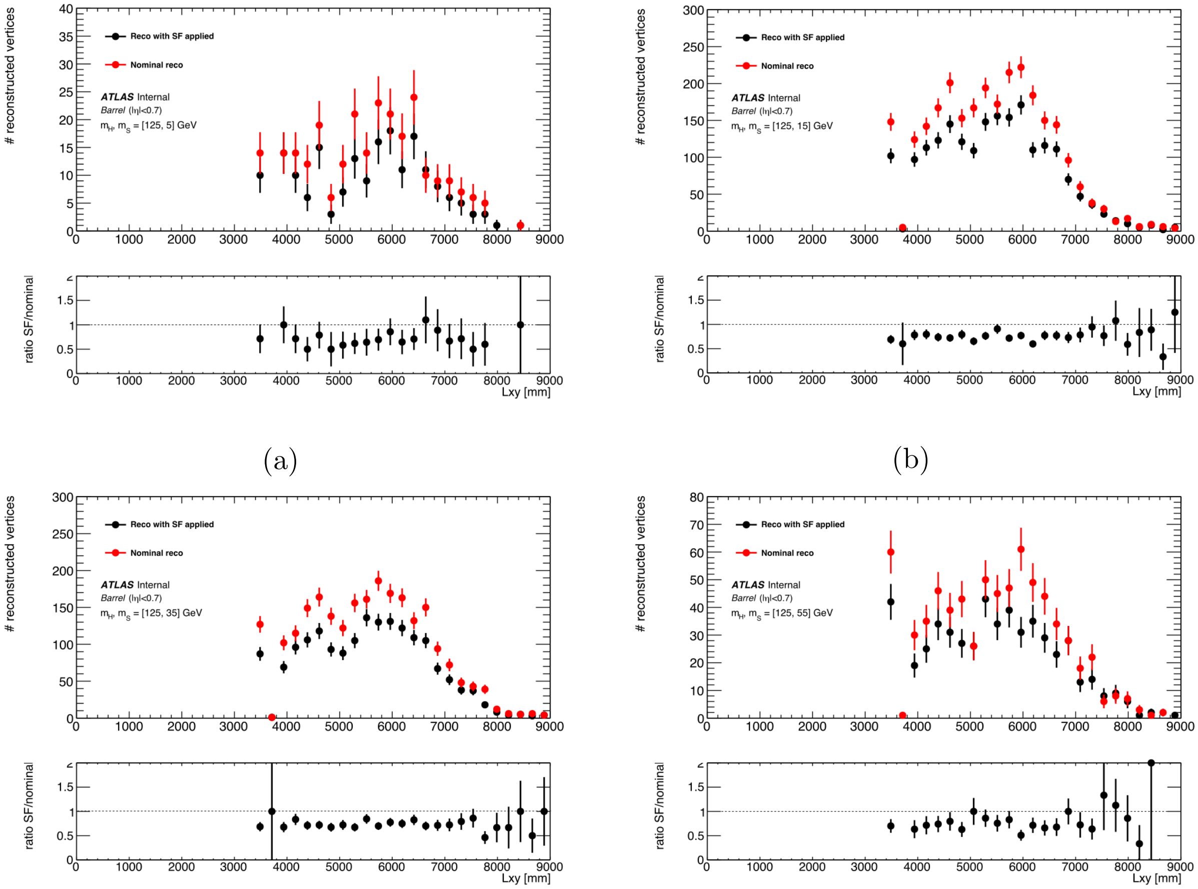

(a)

(b)

(c)

(d)

Figure 6.4: Vertex reconstruction efficiency in the barrel after the vertexing scale factor is applied compared with efficiency after nominal reconstruction for scalar samples mediated by the SM-like Higgs.

In order to compute the systematic uncertainty associated to rescaling the vertex reconstruction efficiency, the loss of efficiency is also evaluated by an alternative method and a comparison is made with the primary method of dropping tracklets during reconstruction. The alternative method uses the ratio between the data and MC distributions as a weight

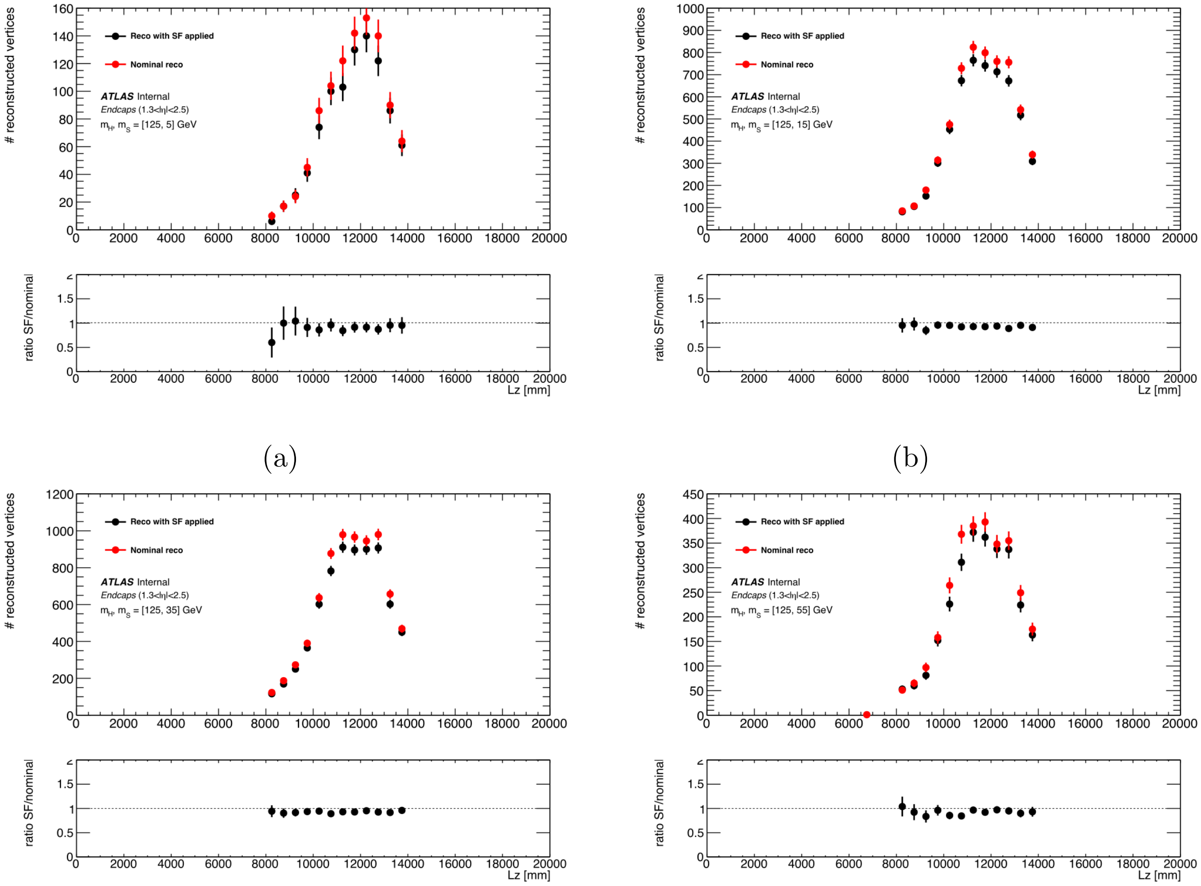

(a) (b)

(c) (d)

Figure 6.5: Vertex reconstruction efficiency in the endcaps after the vertexing scale factor is applied compared with efficiency after nominal reconstruction for scalar samples mediated by the SM-like Higgs.

m_{Φ} [GeV]	m_s[GeV]	nVertices reconstructed with nominal reco	nVertices reconstructed after SF is applied during reco	Loss in efficiency
125	5	266	193	27.4%
	15	2723	2047	24.8%
	35	2414	1765	26.9%
	55	720	531	26.3%
60	5	1921	1403	27.0%
	15	1417	1085	23.4%
200	50	3481	2617	24.8%
400	100	6536	4463	31.7%
600	50	17060	12943	24.1%
	150	11254	7736	31.3%
	275	3821	2849	25.4%
1000	50	10414	7144	28.7%
	275	15598	11546	26.0%
	475	3077	2071	32.7%

Table 6.2: Summary of the effect of the vertex scale factor on vertex reconstruction efficiency in the barrel for all signal samples.

m_{Φ} [GeV]	m_s[GeV]	nVertices reconstructed with nominal reco	nVertices reconstructed after SF is applied during reco	Loss in efficiency
125	5	2072	1864	10.0%
	15	11887	11031	7.20%
	35	15224	14118	7.26%
	55	5982	5525	7.64%
60	5	20440	18162	11.1%
	15	12104	11085	8.42%
200	50	17408	16218	6.84%
400	100	20690	18002	13.0%
600	50	29403	27765	5.57%
	150	25759	22333	13.3%
	275	36795	34116	7.28%
1000	50	12996	12001	7.66%
	275	26006	24194	6.97%
	475	28078	23805	15.2%

Table 6.3: Summary of the effect of the vertex scale factor on vertex reconstruction efficiency in the endcaps for all signal samples.

for each bin in fig. 6.3 from the ratio between the data and MC distributions. Then while calculating vertex reconstruction efficiency, the appropriate weight is applied to each vertex given the number of tracklets associated to it. The effect of reweighting the reconstruction efficiency is seen in figs. 6.6 and 6.7. Again, for simplicity, the loss of efficiency is taken to be the average over all samples and this is reported in the second column of tables 6.4 and 6.5. The systematic uncertainty is taken to be difference between the loss of efficiency calculated with dropped tracklets versus with bin-by-bin reweighting, as seen in the third and final column of tables 6.4 and 6.5.

It is interesting to note that the loss of efficiency calculated with the reweighting method is approximately equal between the barrel and endcaps regions, unlike with the primary method. This is not fully understood and further study would be useful, particularly as a reconciliation between the two methods would reduce the systematic uncertainty associated with tracklet mismodelling.

Loss in efficiency, dropped tracklets	Loss in efficiency, reweighting	Difference between methods
27%	19%	8.0%

Table 6.4: Summary of calculated effect of vertex mismodeling on vertex reconstruction efficiency in the barrel and the associated systematic uncertainty.

Loss in efficiency, dropped tracklets	Loss in efficiency, reweighting	Difference between methods
9.0%	21%	12%

Table 6.5: Summary of calculated effect of vertex mismodeling on vertex reconstruction efficiency in the endcaps and the associated systematic uncertainty.

The vertex efficiencies computed using the nominal DAOD MC files are scaled down following the results obtained rerunning the MS vertex reconstruction reported in tables 6.2 and 6.3. Figure 6.8 shows the final, scaled-down MS vertex reconstruction efficiency as a function of the R and z position of the vertex in the barrel and endcaps respectively, computed using each signal sample. The various detector boundaries are depicted by dashed lines.

For the scalar mass of 5 GeV the barrel MS vertex reconstruction efficiency is about 10 % near the calorimeter face ($r \sim 4$ m) and it substantially decreases as the decay occurs closer to the middle station ($r \sim 7$ m). For decays occurring close to the middle station

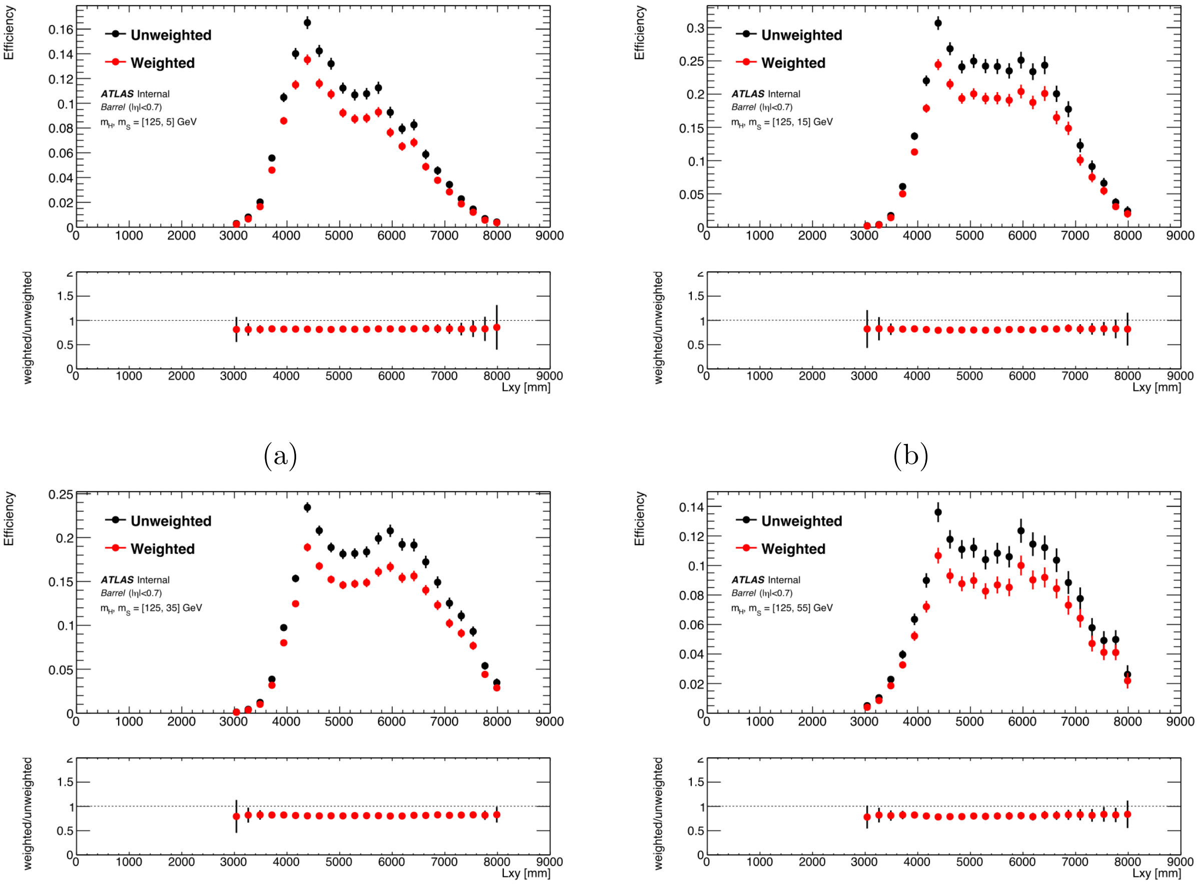

(a) (b)

(c) (d)

Figure 6.6: Vertex reconstruction efficiency in the barrel with reweighting applied compared with efficiency after nominal reconstruction for HSS samples with a SM-like Higgs mediator.

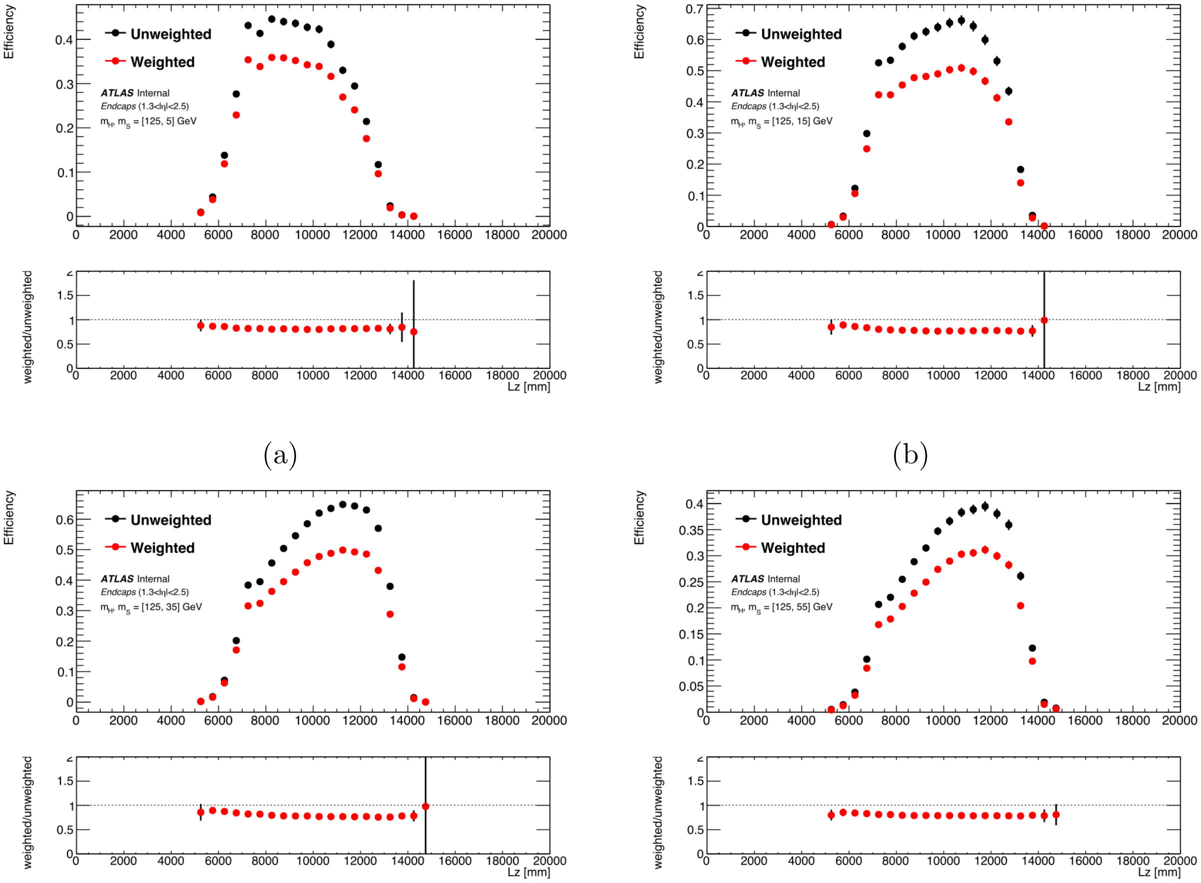

(a) (b)

(c) (d)

Figure 6.7: Vertex reconstruction efficiency in the endcaps with reweighting applied compared with efficiency after nominal reconstruction for HSS samples with a SM-like Higgs mediator.

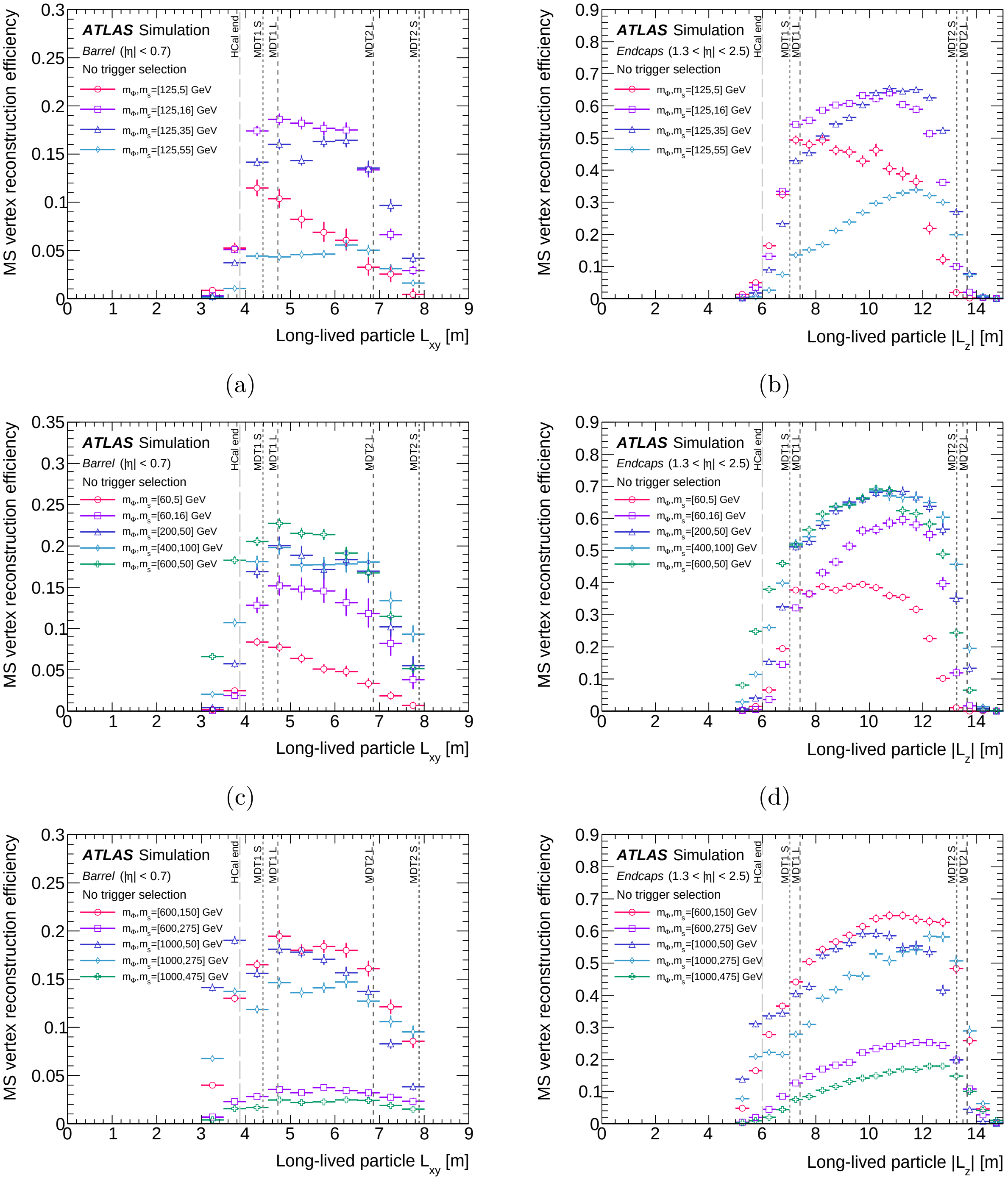

(a) (b)

(c) (d)

(e) (f)

Figure 6.8: Truth-based MS vertex reconstruction efficiency for (a-b) HSS samples where $m_{\Phi} = 125$ GeV and (c-f) HSS samples where $m_{\Phi} \neq 125$ GeV. Plots on the left side are for the barrel, and those on the right side are for the endcaps.The efficiency is scaled down according to the calculated effect of tracklet mismodeling, and no trigger selection is applied.

the vertex reconstruction efficiency decreases because the charged hadrons and photons (and their corresponding EM showers) are not spatially separated and overlap as they traverse the middle station. This reduces the efficiencies for tracklet reconstruction and, consequently, MS vertex reconstruction. The efficiency slightly increases as the mass increases, e.g. for the 15 GeV and 35 GeV samples, because (1) there is more activity and (2) the boost is lower, so the decay products are more spatially separated. This trend does not extend to the 55 GeV sample, however, as its very low boost leads to a very wide decay and not all of the activity is contained within the $\Delta R < 0.6$ cone used to select hits for the vertexing algorithm.

The efficiency for reconstructing vertices in the MS endcaps reaches 70 %. Because there is no magnetic field in the region in which endcaps tracklets are reconstructed, the vertex reconstruction algorithm does not have the same constraints that are present in the barrel [50]; consequently, the endcaps vertex reconstruction is more efficient on signal but also is less robust in rejecting random background.

6.5 MS vertex residuals

To characterize the accuracy of the MS vertex reconstruction algorithm for vertices passing the GVC, *residuals* are calculated as the difference between the position of the decay at truth level and the position of the reconstructed vertex. The residuals in η and ϕ are of particular interest since several selections described in chapter 7 are based on the distance $\Delta R = \sqrt{(\Delta\phi)^2 + (\Delta\eta)^2}$ between an MS vertex and some other object, seen in table 7.1.

The residuals in η, ϕ, R, and z are shown in figs. 6.9 and 6.10 for various HSS samples with a Higgs-like mediator and in figs. 6.11 and 6.12 for various samples with other scalar mediator masses. The barrel and endcaps vertices are shown separately, and sometimes display different behaviour. This is expected, as the reconstruction algorithms differ. The most obvious difference exists in the z-residuals of endcaps vertices, which show a shift away from 0 mm for several Higgs and scalar boson samples. This feature is not present in any barrel vertex residuals, but it is expected in the endcaps. After the LLP decays into many charged tracks, the magnetic field in the endcaps toroid bends the charged tracks while preserving the line-of-flight of the LLP. Because the tracklets are measured after the magnetic field and extrapolated back into the magnetic field region as straight lines, the vertex position is systematically shifted to larger values of $|z_{\mathrm{reco}}|$ and R_{reco} with respect to the true decay position. Due to differences in the underlying LLP kinematics, the shift is not present in all samples. Further details are provided in Ref. [50].

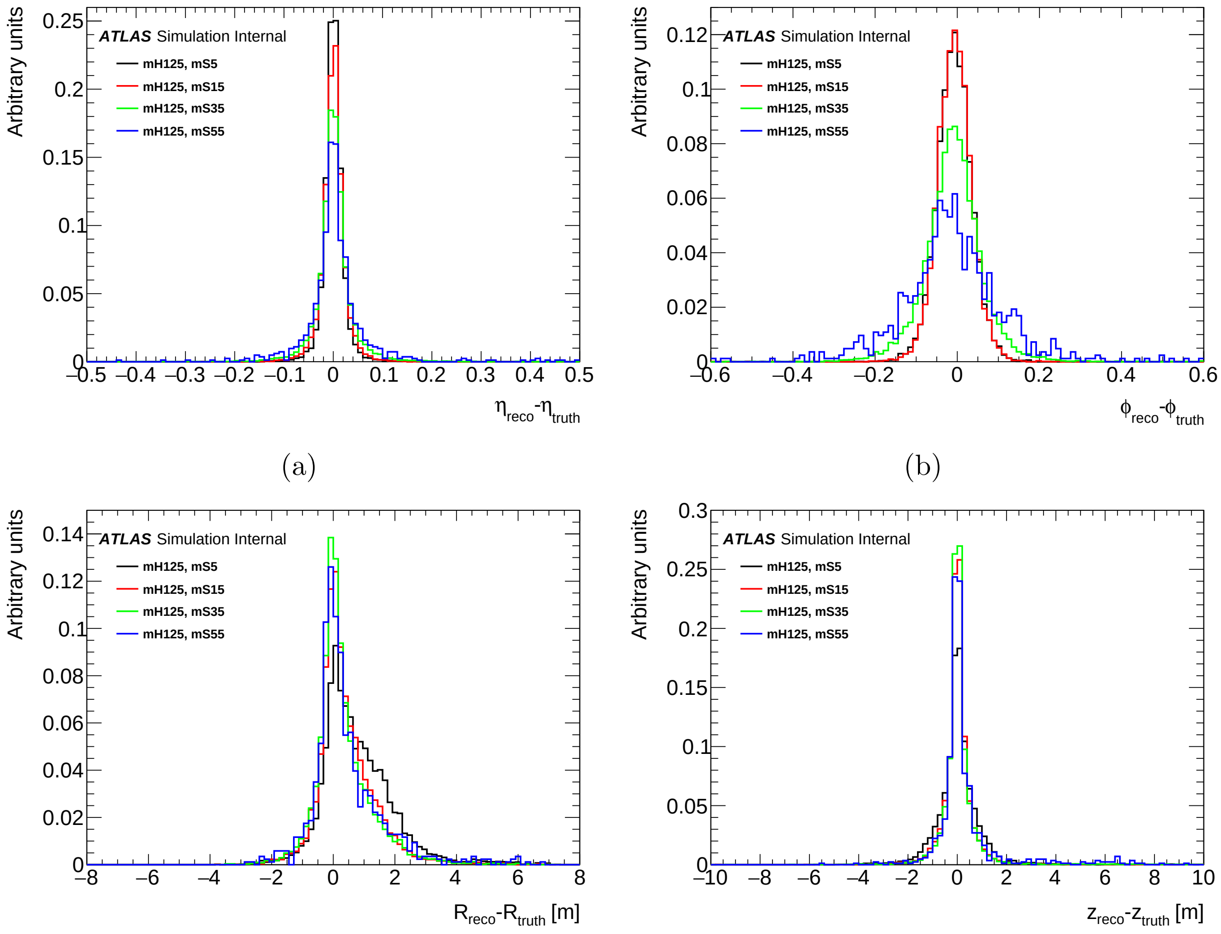

(a) (b)

(c) (d)

Figure 6.9: Vertex residuals in (a) η, (b) ϕ, (c) R, and (d) z coordinates for decays in the MS barrel for HSS samples where $m_{\Phi} = 125$ GeV.

m_{Φ} [GeV]	m_s [GeV]	η	ϕ	R	z
125	5	0.058	0.084	0.25	0.34
	15	0.072	0.081	0.20	0.34
	35	0.094	0.096	0.19	0.46
	55	0.11	0.12	0.22	0.68

Table 6.6: Summary of resolutions for MS vertices in the barrel region for various HSS samples where $m_{\Phi} = 125$ GeV.

m_Φ [GeV]	m_s [GeV]	η	ϕ	R	z
125	5	0.033	0.072	0.28	0.25
	15	0.037	0.076	0.27	0.24
	35	0.050	0.10	0.31	0.24
	55	0.072	0.14	0.41	0.24

Table 6.7: Summary of resolutions for MS vertices in the endcap region for various HSS samples where $m_\Phi = 125$ GeV.

m_Φ [GeV]	m_s [GeV]	η	ϕ	R	z
60	15	0.071	0.081	0.18	0.30
200	50	0.10	0.099	0.23	0.57
400	100	0.12	0.10	0.25	0.70
600	150	0.13	0.11	0.28	0.80
1000	275	0.14	0.12	0.32	1.03

Table 6.8: Summary of resolutions for MS vertices in the barrel region for various HSS samples where $m_\Phi \neq 125$ GeV.

m_Φ [GeV]	m_s [GeV]	η	ϕ	R	z
60	15	0.043	0.083	0.30	0.23
200	50	0.055	0.10	0.33	0.26
400	100	0.066	0.11	0.37	0.29
600	150	0.073	0.12	0.39	0.30
1000	275	0.093	0.13	0.45	0.33

Table 6.9: Summary of resolutions for MS vertices in the endcap region for various HSS samples where $m_\Phi \neq 125$ GeV.

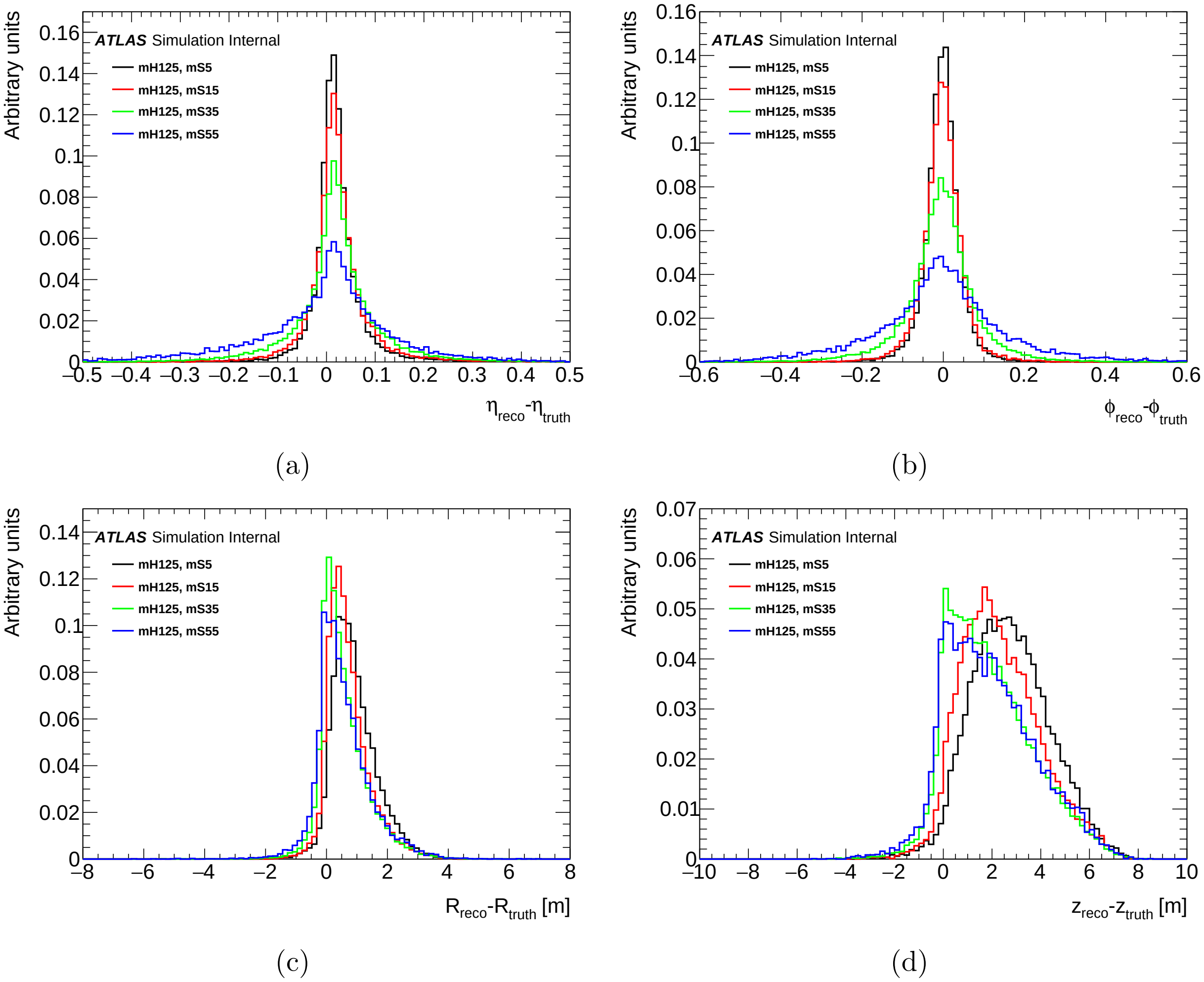

(a) (b)

(c) (d)

Figure 6.10: Vertex residuals in (a) η, (b) ϕ, (c) R, and (d) z coordinates for decays in the MS endcaps for HSS samples where $m_{\Phi} = 125$ GeV

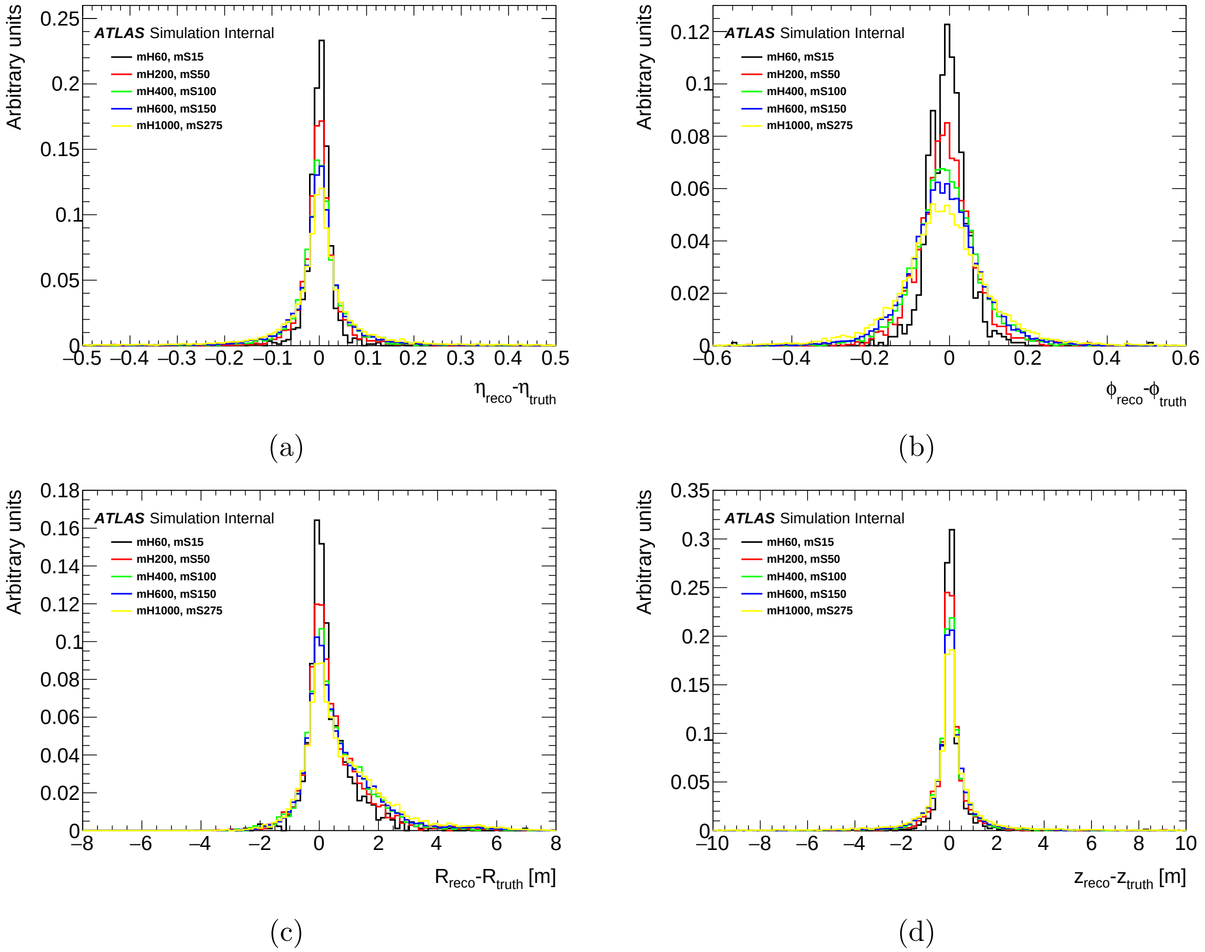

(a) (b)

(c) (d)

Figure 6.11: Vertex residuals in (a) η, (b) ϕ, (c) R, and (d) z coordinates for decays in the MS barrel for HSS samples where $m_{\Phi} \neq 125$ GeV.

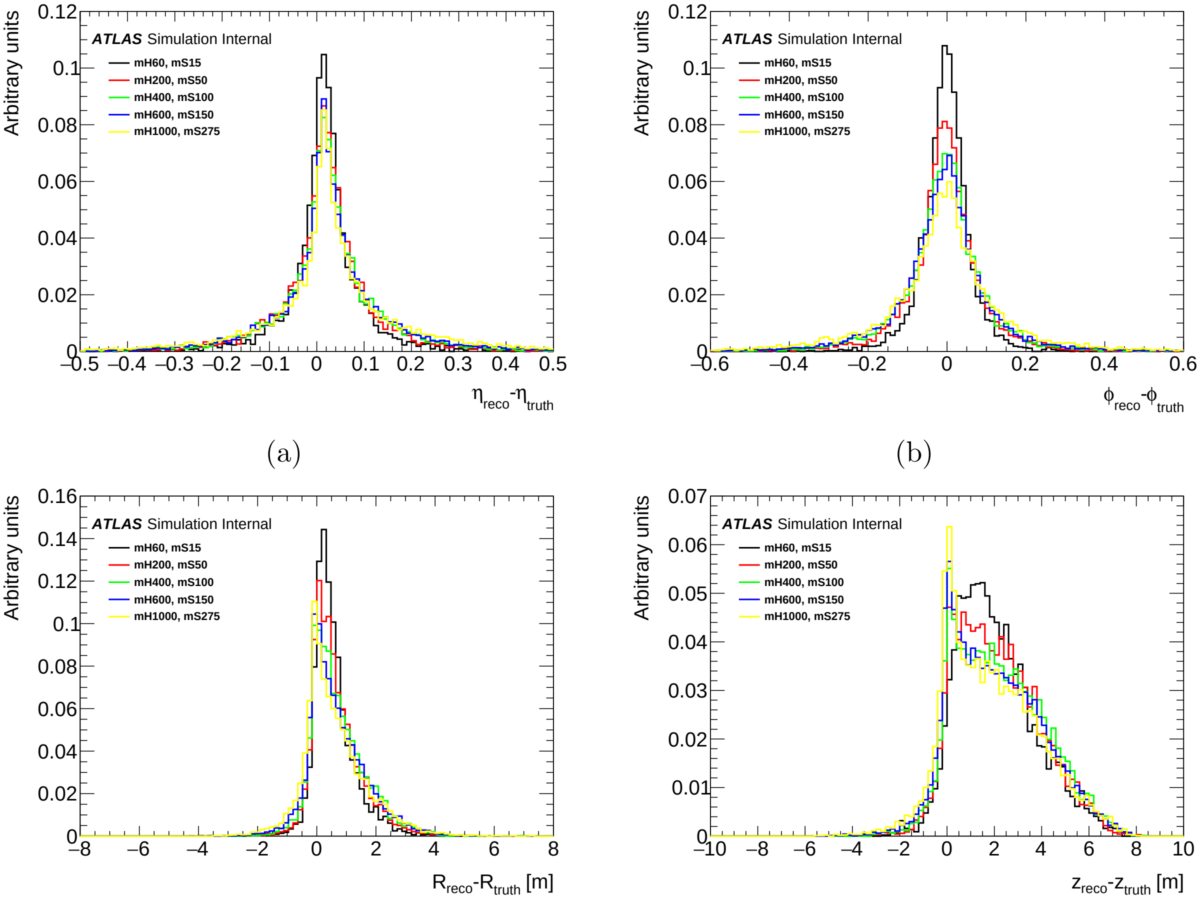

(a) (b)

(c) (d)

Figure 6.12: Vertex residuals in (a) η, (b) ϕ, (c) R, and (d) z coordinates for decays in the MS endcaps for HSS samples where $m_{\Phi} \neq 125$ GeV.

Chapter 7

Two-vertex search

This section details the search for events with two isolated, displaced MS vertices. This search is inclusive of any model that produces at least two hadronically-decaying neutral LLPs. In particular, it has good sensitivity for the decays of a heavy scalar mediator to a pair of neutral, long-lived scalars as described in Section 2.3.1. The requirement that both LLPs decay in the fiducial volume of the MS has the advantage that it results in negligible background, but it also limits the range of LLP lifetimes to which the search is sensitive.

This analysis relies on negligible background. Isolated displaced vertices can be reconstructed from the processes listed below. With the exception of the first item, which is attributed to energy mismeasurement, these vertices appear isolated because the associated process does not originate at the IP.

- A jet fluctuates to contain only neutral hadrons, so its energy is then mismeasured in the calorimeters to be much lower than its truth energy. If it is able to punch-through to the muon system, then it leaves a shower of activity that appears isolated from significant calorimeter activity.
- Beam-halo muons can shower in the endcaps, leaving enough activity to reconstruct a vertex.
- Cosmic muons can shower in the detector, or a cosmic shower can leave enough activity to reconstruct a vertex.
- Noise bursts in the muon system can create enough MDT and trigger hits to reconstruct a vertex through combinatorics.

The probability to reconstruct a single, isolated displaced vertex from any background source is very small. A vertex may be reconstructed from any source that leaves a significant amount of activity in the MS; however, vertices reconstructed from non-signal sources are rarely isolated since they overwhelmingly stem from punch-through jets, which have activity preceding the vertex in the ID and calorimeters. The existence of a second isolated vertex in the same event is uncorrelated to the first, and therefore the probability to find two isolated vertices is proportional to the square of an already small number. However, this background is not exactly zero, and with the high collision statistics being provided by the LHC it is crucial to accurately quantify it.

The reconstruction of background vertices from these processes is not accurately simulated in MC samples. In principle, it would be possible to estimate the background contribution from punch-through jets (i.e. the first item listed above). However, the events with enough fluctuation for the vertex to appear isolated are so rare that extremely large statistics would be required to avoid unreasonably large statistical uncertainties. This is not feasible from a computing resources standpoint. Therefore, a data-driven background estimation method is required.

The analysis cutflow to select signal events is detailed in section 7.1, followed by a description of the background estimation procedure in section 7.2. The validation of this background procedure is described in section 7.3, which is used to determine the systematic uncertainty on the background estimation. Finally, the procedure used to extrapolate the results of the analysis to higher and lower lifetimes is described in section 7.4.

7.1 Analysis cutflow

Event selection in the analysis cutflow can be split into two levels, as summarized in table 7.1. The first level is referred to as *preselection*. At this stage, the event is required to pass the Muon RoI Cluster trigger and have two vertices reconstructed in the MS. The event must also pass basic data quality criteria. Each part of the detector must be fully operational and output uncorrupted data, and a primary vertex must be reconstructed with at least two tracks. The latter requirement reduces contributions from non-collision background sources that occur in a paired bunch crossing.

The next level, *MS vertex selection*, assesses the quality of the two vertices reconstructed in the event. Two regions in the detector are vetoed. The first is the MS overlap region, which is defined as $0.8 < |\eta| < 1.3$. The MS transitions from the barrel to the endcaps in this region, which presents an issue since the vertex reconstruction algorithm operates differently and independently in the barrel and the endcaps. If an LLP decays in this region, some hits may be in barrel chambers and others in endcaps chambers. Then reconstruction efficiency drops significantly, since each reconstruction algorithm attempts to reconstruct a vertex with a subset of the total hits. Occasionally, however, a vertex is successfully reconstructed in both regions, leading to two vertices created from a single LLP decay. Since reconstruction efficiency is poor in this region anyways, it was decided to exclude the overlap region altogether. The second region that is vetoed is the HCal crack region, defined as $0.7 < |\eta| < 1.3$. In this region, the rate of jets punching through to the MS is higher, leading to higher background. Since most of this region was already excluded due to the MS overlap region, it does not represent a significant loss of efficiency to exclude the remaining region of $0.7 < |\eta| < 0.8$.

Additionally, one vertex must match the triggering muon RoI cluster within $\Delta R = 0.4$ since the muon RoI cluster and vertex arising from an LLP decay will rarely have a large separation between them. If a second muon RoI cluster is present in the event, the second vertex must be matched to the second cluster.

Moreover, if there are two clusters in an event then they are required to have some minimum separation between them. The muon RoI cluster algorithm can easily produce multiple clusters that are close to each other, since it is simply a naive cone algorithm with a radius of $\Delta R = 0.4$. Since this radius is a hard cut, any large clusters with muon RoIs spread over an angle larger than 0.4 will appear to be two smaller clusters. However, these two clusters would represent a single region of MS activity. Therefore, clusters must be separated by more than 0.8 to be well-defined. Therefore, clusters are required to have some minimum separation between them. Signal events tend to be separated by at least $\Delta R = 1.0$, as seen in Figure 7.1, so 1.0 is chosen as the minimum separation between clusters.

Additionally, the vertex reconstruction algorithm starts from $(\Delta\eta \times \Delta\phi) = (0.7 \times 1.0)$ clusters of tracklets. Consequently, even if two LLP decays occurred close together, it is unlikely that the vertex reconstruction algorithm could resolve them. Therefore, two vertices reconstructed in an event are also required to be separated by at least $\Delta R > 1.0$.

MS vertices must also pass the GVC requirements detailed in Section 5.4.3.

Table 7.1: Description of the signal selection criteria used for the two vertex search.

Level	Cut	Value
Preselection	Trigger	HLT_j30_muvtx_noiso
	Event cleaning	Standard ATLAS event cleaning
	Primary vertex	At least one (standard ATLAS selection)
	MS Vertex multiplicity	At least 2
MS Vertex selection	MS Overlap region veto	$0.8 < \|\eta_{vx}\| < 1.3$
	HCal crack veto	$0.7 < \|\eta_{vx}\| < 1.3$
	Trigger matching	ΔR(vx, muon RoI cluster) < 0.4
		If a second trigger cluster is present, second vertex matches cluster
	Min. cluster-cluster separation	$\Delta R > 1.0$
	Min. vertex-vertex separation	$\Delta R > 1.0$
	GVC	See table 5.3

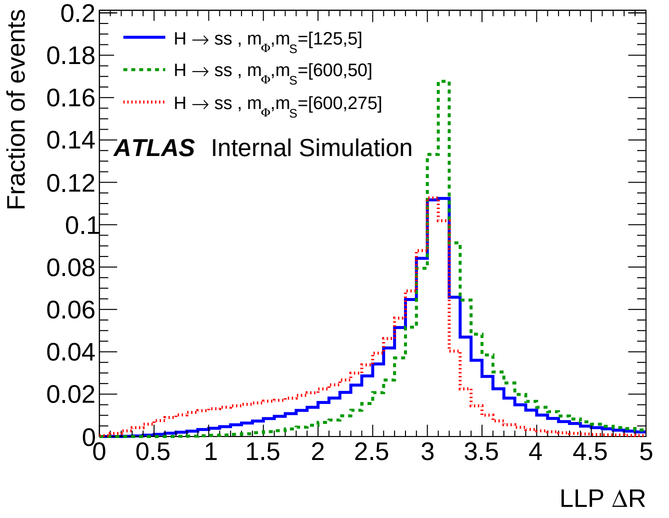

Figure 7.1: Angular separation, ΔR, between long-lived scalars.

7.2 Expected number of background events

To estimate the expected background for the two-vertex strategy, the frequency with which the MS vertex algorithm reconstructs isolated vertices for non-signal events must be quantified. This estimation can be calculated from data using events with *one* isolated MS vertex, which pass either the Muon RoI Cluster trigger or a zero-bias trigger. Two types of vertices must be considered: those matched to a trigger cluster, and those occurring without any trigger. (In the signal, it is important to note, at least one vertex must be associated to a cluster that passes the trigger, or the event would not pass the full cutflow.) Additionally, the barrel and endcaps must be treated separately both because different triggering technologies are used (RPCs in the barrel and TGCs in the endcaps) with different requirements, and because the vertex reconstruction algorithm differs between the two regions.

As stated above, the probability of reconstructing one vertex in an event is uncorrelated to the probability of reconstructing a second. Therefore, the expected number of events with two vertices can be calculated as the number of events with one vertex ($N_{1\text{vx}}$) multiplied by the probability of reconstructing a vertex ($P_{1\text{vx}}$):

$$N_{2\text{vx}} = N_{1\text{vx}} \cdot P_{1\text{vx}} \ . \tag{7.1}$$

To pass the two vertex signal selection, an event is required to have at least one cluster present, and one of the vertices must be matched to it within $\Delta R = 0.4$. This is referred to in the following paragraphs as a vertex-cluster pair, and its frequency is encompassed in the value of $N_{1\text{vx}}$. Then the probability of finding a second vertex, $P_{1\text{vx}}$, depends on if there is a second muon RoI cluster in the event, since a vertex is more likely to be reconstructed when a cluster is present. Equation (7.1) must be split into two terms, then:

$$N_{2\text{vx}} = N_{1\text{vx}}^{1\text{cl}} \cdot P_{1\text{vx}}^{0\text{cl}} + N_{1\text{vx}}^{2\text{cl},1\text{UM}} \cdot P_{1\text{vx}}^{1\text{cl}} \tag{7.2}$$

where the first term estimates the number of background events with two vertices and one cluster, and the second term estimates the number with two vertices and two clusters. In the calculation, $N_{1\text{vx}}^{1\text{cl}}$ is the number of events with a vertex-cluster pair, and $P_{1\text{vx}}^{0\text{cl}}$ is the probability of reconstructing a vertex in an event without a cluster present. $N_{1\text{vx}}^{2\text{cl},1\text{UM}}$ is the number of events with a vertex-cluster pair and a second, unmatched cluster. Finally, $P_{1\text{vx}}^{1\text{cl}}$

is the probability of reconstructing a vertex in an event with a cluster present.

The second term in eq. (7.2) must be further expanded because the barrel and endcaps must be treated differently; the probability of reconstructing a vertex is different for events with a cluster in the barrel versus the endcaps. So, the full equation to estimate expected background with two isolated MS vertices is calculated as:

$$N_{\text{2vx}} = \left(N_{\text{1vx}}^{\text{1cl}} \cdot P_{\text{1vx}}^{\text{0cl}}\right) + \left(N_{\text{1vx}}^{\text{2cl,1UMBcl}} \cdot P_{\text{1vx}}^{\text{1Bcl}}\right) + \left(N_{\text{1vx}}^{\text{2cl,1UMEcl}} \cdot P_{\text{1vx}}^{\text{1Ecl}}\right) \ . \tag{7.3}$$

where $N_{\text{1vx}}^{\text{2cl,1UMBcl(Ecl)}}$ is the number of events with a vertex-cluster pair and a second, unmatched cluster in the barrel (endcaps) and $P_{\text{1vx}}^{\text{1Bcl(Ecl)}}$ is the probability of reconstructing a vertex in an event with a cluster present in the barrel (endcaps).

All quantities used in the calculation of eq. (7.3) are reported in table 7.2. The numbers $N_{\text{1vx}}^{\text{1cl}}$, $N_{\text{1vx}}^{\text{2cl,1UMBcl}}$, and $N_{\text{1vx}}^{\text{2cl,1UMEcl}}$ are counted in events that pass the Muon RoI Cluster trigger in the main stream. The probability $P_{\text{1vx}}^{\text{1Bcl}}$ ($P_{\text{1vx}}^{\text{1Ecl}}$) is also evaluated with events passing the Muon RoI Cluster trigger in the main stream, where the number of events with a vertex-cluster pair in the barrel (endcaps), $N[\text{1BClVx}]$ ($N[\text{1EClVx}]$), is divided by the total number of events containing a barrel (endcaps) cluster, $N[\text{1BCl}]$ ($N[\text{1ECl}]$).

The probability $P_{\text{1vx}}^{\text{0cl}}$ cannot be calculated using events passing the Muon RoI Cluster trigger, since by definition no cluster can be present in the event. Instead it is calculated by dividing the number of good, isolated MS vertices found in zero-bias events not passing the Muon RoI Cluster trigger, $N[\text{1Vx}]$, by the total number of zero-bias events that satisfy standard event quality criteria, $N[\text{Events}]$. However, to use $P_{\text{1vx}}^{\text{0cl}}$ appropriately when it is calculated from a different stream than the other terms, a rescaling factor must be applied. This is because the zero-bias data is collected at a fixed rate of 7 Hz, unlike data collected by the Muon RoI Cluster trigger, whose rate is not fixed and is therefore collected at a rate generally proportional to luminosity. As a result, runs with higher instantaneous luminosity are undersampled by zero-bias data as compared to runs with lower instantaneous luminosity.

The rescaling factor is defined as the ratio of the pileup profile of the zero-bias data and the main stream data (where data passing the Muon RoI Cluster trigger is collected) as a function of pileup μ. The ratio is calculated separately for each data-taking year, and is shown in fig. 7.2. The rescaling factor is then applied as an event weight onto the zero-bias data. The effect of applying the rescaling factor can be seen in table 7.3, and the values reported in table 7.2 already have the reweighting applied.

Table 7.2: Numbers of events in the 13 TeV dataset passing the Muon RoI Cluster trigger (in the main stream) and the zero-bias trigger (in the zero-bias stream). Vertices are required to pass the GVC described in Section 5.4.3. Uncertainties are statistical only. The probabilities needed to compute the background from events containing MS vertices from non-signal processes are also reported. Uncertainties on the probabilities are propagated from the Poisson uncertainty associated with the event counts that produce them. Uncertainties on values less than 500 are the bounds of the Poisson CI at 68%.

Stream	Quantity	Value
Zero-bias	N[Events]	115709381 ± 10757
	N[1Vx]	53 ± 7
	$\rightarrow P_{\mathrm{1vx}}^{\mathrm{0cl}}$	$(4.61 \pm 0.63) \times 10^{-7}$
Main	$N_{\mathrm{1vx}}^{\mathrm{1cl}}$	674775 ± 821
	$N_{\mathrm{1vx}}^{\mathrm{2cl,1UMBcl}}$	$3_{-1.17}^{+2.43}$
	$N_{\mathrm{1vx}}^{\mathrm{2cl,1UMEcl}}$	$0_{-0.00}^{+1.35}$
	N[1BCl]	38509130 ± 6206
	N[1BClVx]	124648 ± 353
	$\rightarrow P_{\mathrm{1vx}}^{\mathrm{1Bcl}}$	$(3.24 \pm 0.009) \times 10^{-3}$
	N[1ECl]	15598939 ± 3950
	N[1EClVx]	550127 ± 742
	$\rightarrow P_{\mathrm{1vx}}^{\mathrm{1Ecl}}$	$(3.53 \pm 0.005) \times 10^{-2}$

Table 7.3: Numbers of events in the 13 TeV dataset passing the `HLT_zb_noalg_L1ZB` trigger (zero-bias stream) before and after adjusting zero-bias event weights to account for the difference in pileup profile with the main stream. An updated calculation for the probability, $P_{\mathrm{1vx}}^{\mathrm{0cl}}$, is also shown.

Quantity	Value	Reweighted Value
N[Events]	115707416	115709381
N[1Vx]	46	53.3
$\rightarrow P_{\mathrm{1vx}}^{\mathrm{0cl}}$	$(4.06 \pm 0.59) \times 10^{-7}$	$(4.61 \pm 0.63) \times 10^{-7}$

The final background estimation and the number of observed events in 2015-2018 data are summarized in table 7.4, where all uncertainties shown are purely statistical. Following the validation of the background estimation that is described in section 7.3, no systematic uncertainty is assigned to the background estimation procedure.

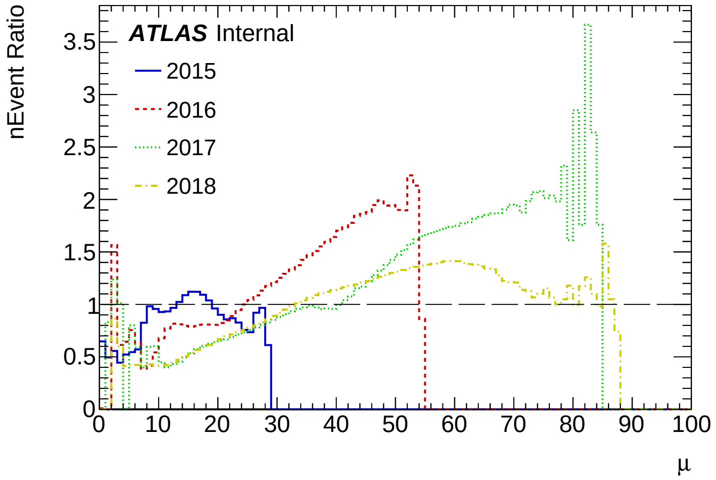

Figure 7.2: Ratio of the number of events occuring in the main stream data, at a given pileup, μ, divided by the number of events occuring in the zero-bias data at the same pileup, μ. This ratio of events defines a per-μ rescaling factor between the main stream and zero-bias data. By applying this rescaling factor as a pileup dependent weight on each zero-bias event, the zero-bias data is scaled to match the main stream pileup profile.

Table 7.4: Total background estimation and observed events in the full Run 2 data. The total background estimation is calculated from eq. (7.3), and the value of each term is shown separately. The value given for $N^{1\text{cl}}_{1\text{vx}} \cdot P^{0\text{cl}}_{1\text{vx}}$ uses the reweighted probability in table 7.3. Uncertainties are statistical only.

Background estimation	
$N^{1\text{cl}}_{1\text{vx}} \cdot P^{0\text{cl}}_{1\text{vx}}$	0.311 ± 0.043
$N^{2\text{cl},1\text{UMBcl}}_{1\text{vx}} \cdot P^{1\text{Bcl}}_{1\text{vx}}$	$0.010^{+0.008}_{-0.004}$
$N^{2\text{cl},1\text{UMEcl}}_{1\text{vx}} \cdot P^{1\text{Ecl}}_{1\text{vx}}$	$0.000^{+0.048}_{-0.000}$
Total estimated events	0.32 ± 0.05
Total observed events	0

Figure 7.3 depicts the background estimation per data-taking year rescaled by the integrated luminosity and the average pileup, and shows that the number of expected events per year is consistent within the different run conditions. The integrated luminosity in 2015 was significantly smaller than in other years, leading to smaller statistics and a higher uncertainty associated with the background estimation.

A previous version of the two-vertex search, performed only on 2015 and 2016 data using a previous ATLAS software release, R20.7, predicted a background of 0.027 ± 0.011 events.

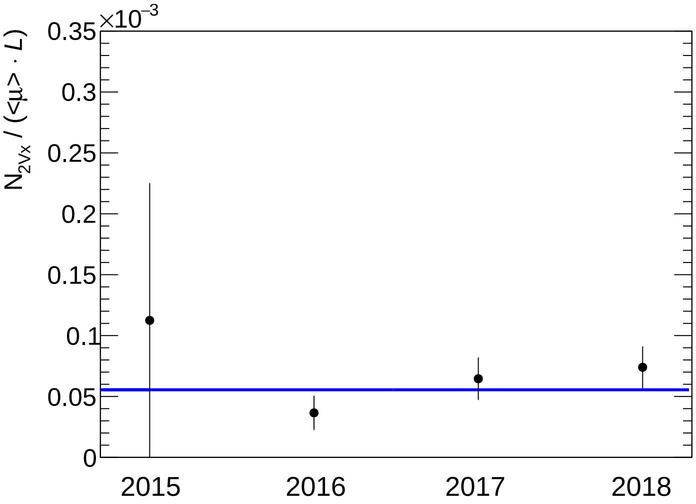

Figure 7.3: Number of background events per data-taking year rescaled by luminosity and average pileup. Probabilities associated with background estimation are recalculated for each data-taking year separately.

The version described in this thesis, which used software release R21, estimated $0.034^{+0.045}_{-0.011}$ for 2015 and 2016 data, which is a bit too high to be compatible with the previous estimation. The difference originates in the change in software release. In R20.7, the values of $N_{\text{1vx}}^{\text{2cl,1UMBcl}}$ and $N_{\text{1vx}}^{\text{2cl,1UMEcl}}$ were both 0. However, in R21 there were small changes as to which events passed the standard ATLAS event cleaning. As a result, one event with two clusters (one of which was unmatched in the barrel) was present in the calculation. If this event is ignored, then the R21 background estimation with 2015 and 2016 data is 0.031 ± 0.011, which is compatible with the R20.7 version.

As an additional note, the increased upper uncertainty primarily comes from the large upper uncertainty on 0 $N_{\text{1vx}}^{\text{2cl,1UMEcl}}$ events, which was not included in the R20.7 analysis.

7.3 Validation of the background estimation

To validate the background estimation, the isolation criteria applied to the MS vertices was inverted and decreased as shown in table 7.5, in a study led by University of Arizona collaborators Michael Schott and Simon Berlendis. The inversion of the isolation defines a background-dominated region orthogonal to the signal region.

The number of background events with two muon RoI clusters was estimated using data

Table 7.5: Inverted isolation criteria applied to MS vertices. All other criteria remained the same.

Requirement	Barrel	Endcaps
$>$ 5 GeV track isolation	$\Delta R < 0.2$	$\Delta R < 0.3$
Track $\lvert\Sigma\vec{p_T}\rvert$ in 0.2 cone	$>$ 10 GeV	$>$ 10 GeV
$>$ 30 GeV jet isolation	$\Delta R < 0.2$	$\Delta R < 0.3$

from the main stream only. To validate this estimation, a check was performed to verify that the number of events with two non-isolated vertices, each matched to a muon RoI cluster, could be accurately predicted. This prediction is given by

$$N^{\mathrm{2cl}}_{2\overline{\mathrm{vx}}} = N^{\mathrm{2cl,1UMBcl}}_{1\overline{\mathrm{vx}}} \cdot P^{\mathrm{1Bcl}}_{1\overline{\mathrm{vx}}} + N^{\mathrm{2cl,1UMEcl}}_{1\overline{\mathrm{vx}}} \cdot P^{\mathrm{1Ecl}}_{1\overline{\mathrm{vx}}} \quad , \tag{7.4}$$

where the "barred" vertex label $\overline{\mathrm{vx}}$ indicates that non-isolated vertices fulfilling the inverted vertex isolation criteria in table 7.5 were used in the computation. Using the values summarized in table 7.6, the total number of expected events with two non-isolated vertex-cluster pairs in the full Run 2 dataset was calculated to be $1.561^{+0.289}_{-0.241}$, and 1 event was observed.

Table 7.6: Validation of the two-cluster term in the background estimation method.

Estimation term	Value	Background contribution
$N^{\mathrm{2cl,1UMBcl}}_{1\overline{\mathrm{vx}}}$	35	$1.561^{+0.289}_{-0.241}$
$P^{\mathrm{1Bcl}}_{1\overline{\mathrm{vx}}}$	$(4460 \pm 6.07) \times 10^{-5}$	
$N^{\mathrm{2cl,1UMEcl}}_{1\overline{\mathrm{vx}}}$	0	0
$P^{\mathrm{1Ecl}}_{1\overline{\mathrm{vx}}}$	$(39414 \pm 34.11) \times 10^{-5}$	
$N^{\mathrm{2cl}}_{1\overline{\mathrm{vx}}}$ (Exp.)		$1.561^{+0.289}_{-0.241}$
$N^{\mathrm{2cl}}_{1\overline{\mathrm{vx}}}$ (Obs.)		1

Validation of the single muon RoI cluster term faced an additional challenge, because the probability to reconstruct a non-isolated vertex without a triggering muon RoI cluster, $P^{\mathrm{0cl}}_{1\overline{\mathrm{vx}}}$, could not be properly estimated in the zero-bias stream. This is due to the fact that events passing the Muon RoI Cluster trigger in the main stream tend to have higher activity in the ID and calorimeters than events passing the zero-bias trigger. As such, a calculation based on zero-bias data would result in a significantly underestimation. Instead, a partial inversion of the isolation criteria was implemented:

$$N^{\mathrm{1cl}}_{1\overline{\mathrm{vx}}1\mathrm{vx}} = N^{\mathrm{1cl}}_{1\overline{\mathrm{vx}}} \cdot P^{\mathrm{0cl}}_{1\mathrm{vx}} \quad . \tag{7.5}$$

By inverting the isolation criteria only on the vertex in the number of cluster-vertex pairs $N^{\mathrm{1cl}}_{1\overline{\mathrm{vx}}}$, the orthogonal validation region being investigated contained one non-isolated vertex-cluster pair and one *isolated* vertex. This strategy validated that the probability of reconstructing an *isolated* vertex, calculated using events from the zero-bias stream, was still valid when applied to the events in the main stream.

Table 7.7: Validation of the single-cluster term in the background estimation method.

Estimation term	Value	Background contribution
$N^{\mathrm{1cl}}_{1\overline{\mathrm{vx}}}$	2426325	0.99 ± 0.20
$P^{\mathrm{0cl}}_{1\mathrm{vx}}$	$(4.09 \pm 0.58) \times 10^{-7}$	
$N^{\mathrm{1cl}}_{1\overline{\mathrm{vx}}1\mathrm{vx}}$ (Obs.)		0

Using the values from table 7.7 in eq. (7.5), the expected background contribution was 0.99 ± 0.20 events containing one non-isolated vertex-cluster pair and one isolated vertex in the full Run 2 data. No events were observed.

Both terms have a consistent background estimation between expected and observed events in the validation region, with a slight overestimation in the expected events. Therefore, no systematic uncertainty is assigned to the background estimation procedure.

7.4 Lifetime extrapolation

The fully simulated signal benchmark MC samples were only generated for a single proper lifetime. However, the analysis is sensitive to a wide range of proper lifetimes. Instead of generating MC events at many lifetimes, the results from the simulated MC sample were extrapolated to larger and smaller lifetimes. A toy MC using only the long-lived particle 4-momenta and reconstruction efficiencies was used to perform this extrapolation the expected number of signal events for each sample, for a range of proper lifetimes between 0 m and 300 m (this is the range between which a useful limit is set). This work was led by University of Arizona collaborator Hao Zhou.

The extrapolation procedures involves the application of several efficiencies, primarily trigger and vertexing efficiencies. In order to determine if a criterion is passed based on an efficiency (*e.g.* applying the probability that an LLP decay fires a trigger or leaves a good reconstructed vertex), a random probability between 0 and 1 is generated. If that probability is less than the efficiency being considered, then the criterion is considered passed. If it is failed, the rest of the criteria are skipped and the toy moves onto the next event.

In principle, the trigger and vertex efficiencies at a certain detector position will be different between signal MC samples with different proper lifetimes because the LLP kinematic distributions are different within the fiducial region of the detector. In order to make the efficiencies lifetime independent and thus get a correct extrapolation result, the trigger and vertex efficiencies need to be calculated as functions of both the LLP decay position and a LLP kinematic variable, which is chosen to be boost β.

Naively calculating trigger efficiency in the two vertex analysis leads to large statistical uncertainties in each bin since there are very few events containing two vertices. To avoid this, trigger efficiency is calculated with events containing one vertex and the result is extrapolated into the two-vertex topology. Assuming that the two LLPs fire triggers independently, the trigger efficiency for the two vertex topology $\epsilon_{\text{trigger, 2LLP}}$ can be estimated by

$$\epsilon_{\text{trigger, 2LLP}}(\text{LLP}_1, \text{LLP}_2) = 1 - (1 - P_{\text{trigger, 1LLP}}(\text{LLP}_1))(1 - P_{\text{trigger, 1LLP}}(\text{LLP}_2)), \qquad (7.6)$$

where $P_{\text{trigger, 1LLP}}$ is the trigger probability calculated in the one vertex region. An example of $P_{\text{trigger, 1LLP}}$ is shown in fig. 7.4 for the signal MC sample with $m_{\Phi} = 125$ GeV, $m_s = 35$ GeV, and low lifetime.

In order to ensure that $P_{\text{trigger, 1vtx}}$ is calculated based on the activity from a single LLP, and not affected by the second LLP in the event, a ΔR cut is applied. Without this cut, the decay products from one LLP can overlap with decay products from another, leading the trigger probability to be artificially inflated. As the ΔR cut increases, however, the trigger probability decreases and statistical uncertainty increases. Several values of ΔR were tested, and the final value was chosen where the estimated trigger efficiency and the trigger efficiency calculated from the signal MC sample is within 1σ uncertainty and the statistical uncertainty is controlled. This value is different for different MC samples, as the kinematics vary. The final ΔR values and the corresponding trigger efficiency results are shown in table 7.8.

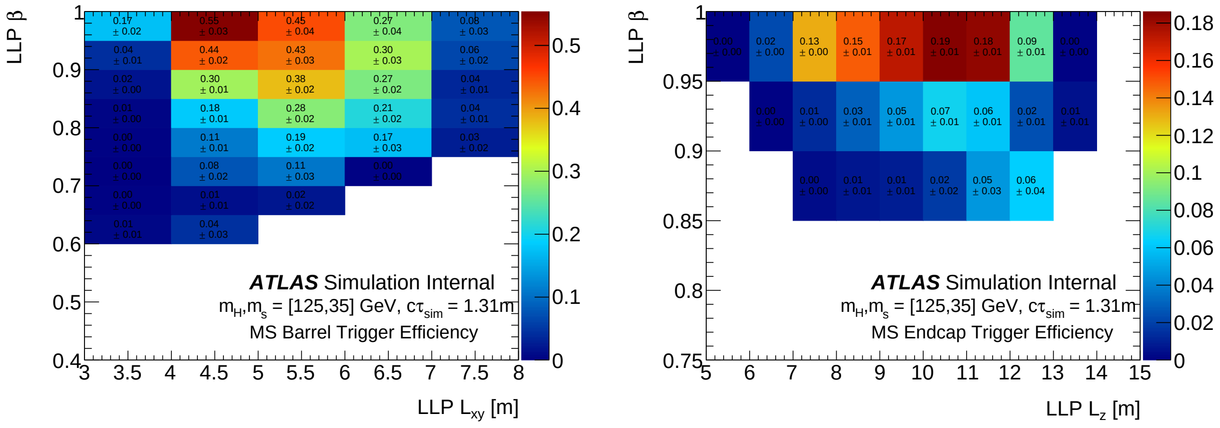

(a) (b)

Figure 7.4: Trigger efficiency for the one vertex topology in the (a) barrel and (b) endcaps.

m_Φ	m_s	Lifetime [m]	ΔR	$f_{trig}^{toy\ estimation}$	$f_{trig}^{fullsim}$	% difference (median)
125	5	0.127	3.0	$0.00183^{+0.00018}_{-0.00017}$	0.00173 ± 0.00011	5.8%
125	5	0.411	3.0	$0.00459^{+0.00030}_{-0.00030}$	0.00434 ± 0.00009	5.7%
125	15	0.580	3.0	$0.00590^{+0.00022}_{-0.00021}$	0.00505 ± 0.00014	16.8%
125	35	1.31	3.0	$0.00386^{+0.00018}_{-0.00017}$	0.00385 ± 0.00008	0.3%
125	55	5.32	2.0	$0.00143^{+0.00013}_{-0.00013}$	0.00141 ± 0.00006	1.4%
60	5	0.217	3.0	$0.000492^{+0.000034}_{-0.000039}$	0.000501 ± 0.000032	1.8%
60	15	0.661	3.0	$0.000482^{+0.000049}_{-0.000050}$	0.000585 ± 0.000048	17.6%
200	50	1.255	3.0	$0.00713^{+0.00034}_{-0.00035}$	0.00666 ± 0.00020	7.1%
400	100	1.608	3.0	$0.01704^{+0.00048}_{-0.00048}$	0.01481 ± 0.00030	15.1%
600	50	0.590	3.0	$0.02487^{+0.00038}_{-0.00040}$	0.02634 ± 0.00039	5.6%
600	150	1.840	3.0	$0.02318^{+0.00042}_{-0.00042}$	0.02176 ± 0.00029	6.5%
600	275	4.288	2.0	$0.00533^{+0.00014}_{-0.00015}$	0.00480 ± 0.00008	11.0%
1000	50	0.406	3.0	$0.03181^{+0.00031}_{-0.00032}$	0.02935 ± 0.00034	8.4%
1000	275	2.399	3.0	$0.02952^{+0.00048}_{-0.00048}$	0.02762 ± 0.00033	6.9%
1000	475	6.039	2.0	$0.00552^{+0.00016}_{-0.00016}$	0.00529 ± 0.00008	4.3%

Table 7.8: The fraction of toy events that pass the trigger selection criteria, the fraction passing the same selection in the full-sim signal samples, and the % difference between them. ΔR shows the minimum separation required between the LLPs, which is tuned to each sample.

Due to the low statistics in the two vertex region, the vertex reconstruction efficiency calculated in the one vertex region, $\epsilon_{\text{vtx reco, 1vtx}}$ is used in the extrapolation procedure. Thus, the vertex reconstruction efficiency for the two vertex topology $\epsilon_{\text{vtx reco, 2vtx}}$ is

$$\epsilon_{\text{vtx reco, 2vtx}}(\text{LLP}_1, \text{LLP}_2) = \epsilon_{\text{vtx reco, 1vtx}}(\text{LLP}_1) \cdot \epsilon_{\text{vtx reco, 1vtx}}(\text{LLP}_2). \tag{7.7}$$

An example of $\epsilon_{\text{vtx reco, 1vtx}}$ is shown in fig. 7.5, again for the signal MC sample with $m_\Phi = 125$ GeV, $m_s = 35$ GeV, and low lifetime.

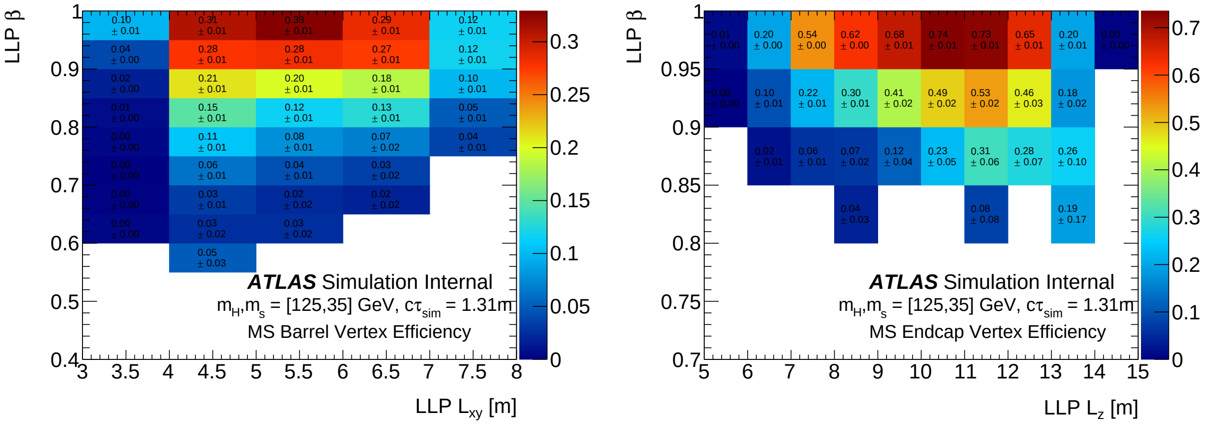

(a) (b)

Figure 7.5: MS vertex reconstruction efficiency calculated in the one MS vertex region in the (a) barrel and (b) endcaps.

The extrapolation procedure is as follows:

1. Starting with $c\tau = 0.0001$ m, a random decay position is generated for each of the two LLPs, sampled from the exponential distribution $f(t) = \exp\{-t/\beta\gamma c\tau\}$.
2. The physical decay position is calculated in the detector for each of the particles, using their stored 4-momenta.
3. The events is deemed worth keeping if the LLP decay positions are within the fiducial volume of the MS. These are classified into three categories based on topology: barrel - barrel, barrel - endcaps, or endcaps - endcaps.
4. It is determined if the LLP decay with the smaller Δt value is "in time". In the endcaps, a decay is in time if $\Delta t < 25$ ns since bunch crossings are 25 ns apart. In the barrel, a decay is in time if its randomly generated probability is greater than the efficiency for the RPC response at the particle's Δt.

5. If the event is in time, it is determined if it passes the RoI cluster trigger by using the estimated efficiency for the trigger $\epsilon_{\text{trigger, 2LLP}}$. The trigger efficiency applied to each LLP depends on the region in which it decayed.

6. If the event passes the trigger, the MS vertex reconstruction efficiency $\epsilon_{\text{vtx reco, 2vtx}}$ is applied to determine if a vertex was reconstructed. The efficiency applied to each LLP depends on the region in which it decayed. If both decays "reconstruct" vertices, the event is counted as a good two vertex event.

7. Steps 2 through 6 are repeated in proper lifetime increments of 0.05 m until $c\tau = 10.0001$ m, and then in 0.5 m increments until $c\tau = 300.0001$ m. The step size is changed because the scale on which the expected signal changes between $c\tau$ values becomes larger and a step size of 0.05 m is unnecessary.

8. Expected signal events are plotted as a function of proper lifetime. These distributions are then rescaled by (production cross-section)x(integrated luminosity)/(number of toy events) to obtain the number of expected signal events in 139 fb^{-1} of data.

9. Each distribution of expected signal events as a function of proper lifetime is divided by the distribution of truth LLP decay position, resulting in global signal efficiency.

Finally, the estimated global signal efficiency is compared with the global signal efficiency directly calculated from the benchmark signal MC sample. The results of the comparison for various signal MC samples are summarized in table 7.9. The percent difference is considered as a systematic uncertainty on the signal. The difference in efficiency depends on the kinematics of the sample, where samples with a low boost tend to show a greater discrepancy in the percent difference.

The toy MC procedure gives an expected number of signal events at each simulated proper lifetime, which is subject to statistical uncertainties from the number of toy events. To present a smooth limit, the global efficiency histograms are fit with a Novosibirsk function [52], which is defined as

$$f(x; x_0, \sigma, \tau) = \exp\left\{ \left[-\frac{1}{2} \left\{ \frac{\ln^2 (1 + \Lambda\tau(x - x_0))}{2\tau^2} + \tau^2 \right\} \right] \right\} \tag{7.8}$$

where $\Lambda = \frac{\sinh(\tau\sqrt{\ln 4})}{\sigma\tau\sqrt{\ln 4}}$.

m_Φ	m_s	Lifetime [m]	$\epsilon_{global}^{toy\ estimation}$	$\epsilon_{global}^{fullsim}$	% diff. (median)	$\frac{\lvert\epsilon_{toy}-\epsilon_{fullsim}\rvert}{\sqrt{\sigma^2_{toy}+\sigma^2_{fullsim}}}$
125	5	0.127	$0.000178^{+0.000021}_{-0.000019}$	0.000155 ± 0.000040	14.8%	0.52
125	15	0.580	$0.000742^{+0.000033}_{-0.000034}$	0.000697 ± 0.000058	6.5%	0.67
125	35	1.31	$0.000552^{+0.000034}_{-0.000032}$	0.000509 ± 0.000029	8.4%	1.00
125	55	5.32	$0.000072^{+0.000009}_{-0.000008}$	0.000065 ± 0.000014	10.8%	0.43
60	5	0.217	$0.000035^{+0.000002}_{-0.000003}$	0.000038 ± 0.000008	7.9%	0.36
60	15	0.661	$0.000054^{+0.000005}_{-0.000006}$	0.000059 ± 0.000015	8.5%	0.32
200	50	1.255	$0.00112^{+0.00008}_{-0.00007}$	0.00101 ± 0.00008	10.9%	1.03
400	100	1.608	$0.00219^{+0.00012}_{-0.00012}$	0.00203 ± 0.00012	7.9%	0.94
600	50	0.590	$0.00268^{+0.00014}_{-0.00014}$	0.00295 ± 0.00013	9.2%	1.41
600	150	1.840	$0.00209^{+0.00011}_{-0.00010}$	0.00231 ± 0.00010	9.5%	1.48
600	275	4.288	$0.000177^{+0.000010}_{-0.000012}$	0.000226 ± 0.000017	21.7%	2.48
1000	50	0.406	$0.00220^{+0.00009}_{-0.00009}$	0.00216 ± 0.00009	1.9%	0.31
1000	275	2.399	$0.00130^{+0.00010}_{-0.00009}$	0.00139 ± 0.00008	6.5%	0.70
1000	475	6.039	$0.000097^{+0.000010}_{-0.000010}$	0.000139 ± 0.000013	30.2%	2.56

Table 7.9: Estimated global signal efficiency from extrapolation method and global signal efficiency from benchmark signal sample. The percent difference is used as systematic uncertainty on the signal.

An example of a fit is shown in fig. 7.6 using the signal sample with $m_\Phi = 125$ GeV, $m_s = 35$ GeV, and low lifetime.

The lifetime extrapolations for all signal MC mass points, after fitting, are shown in figs. 7.7 to 7.10. For the mass points where two samples have been generated, one with a low lifetime and one with a high lifetime, extrapolations from each sample are shown for comparison. In each case, the extrapolation curves are compatible within the statistical uncertainty, so the procedure is considered to have closure.

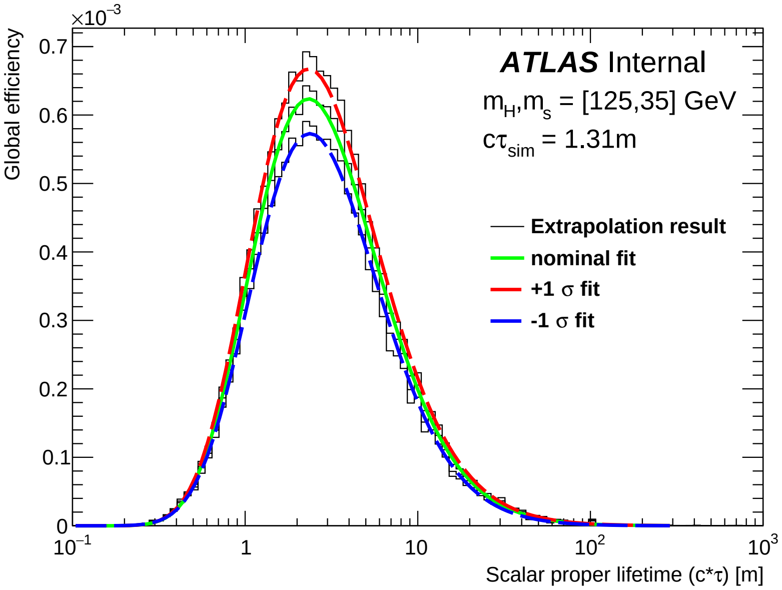

Figure 7.6: The global efficiency is obtained from the extrapolation procedure outlined in section 7.4 and is fit using a Novosibirsk function. The three lines represent the nominal expected events and the variation accounting for all statistical errors.

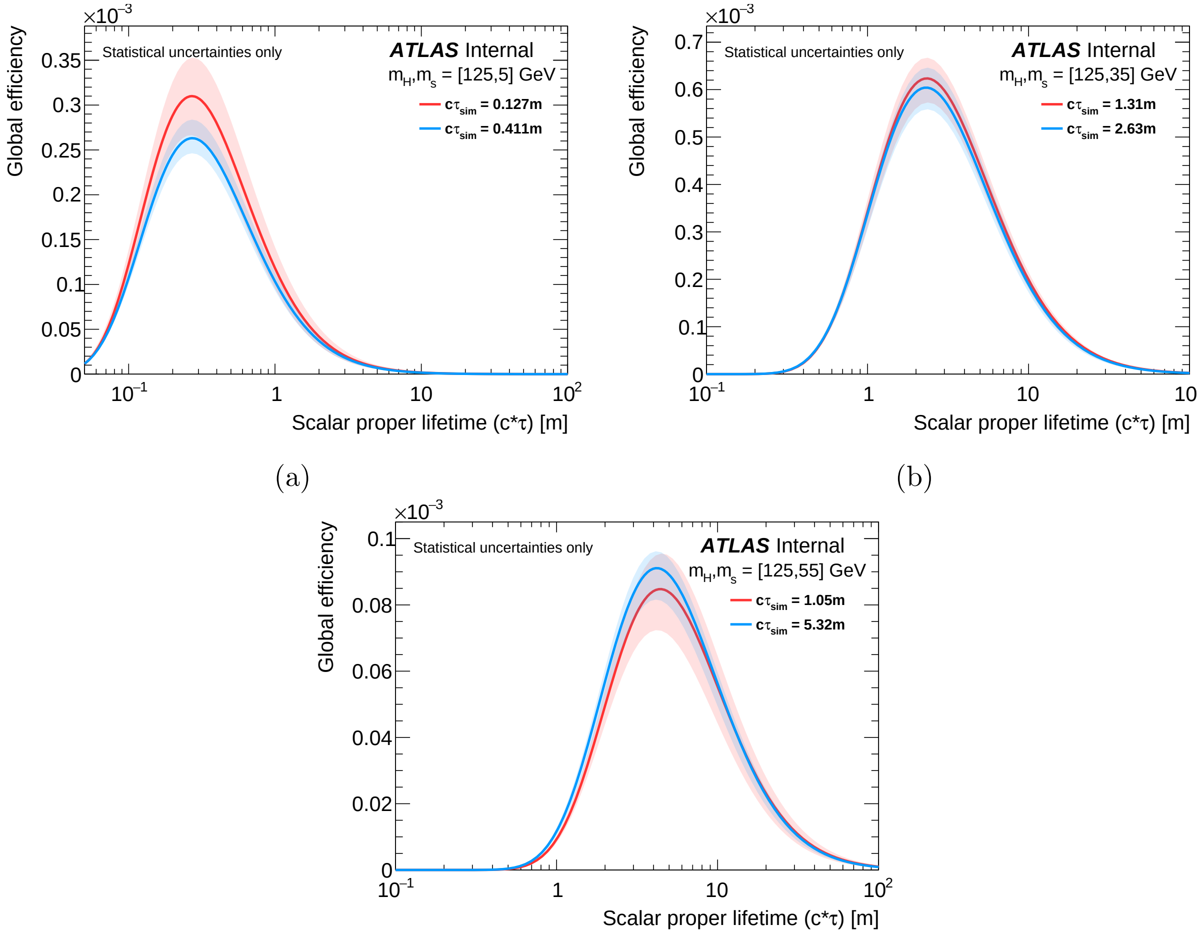

(a) (b)

(c)

Figure 7.7: Extrapolated global signal efficiencies for samples with $m_{\Phi} = 125$ GeV. Uncertainties are statistical, stemming from the efficiencies input into the extrapolation.

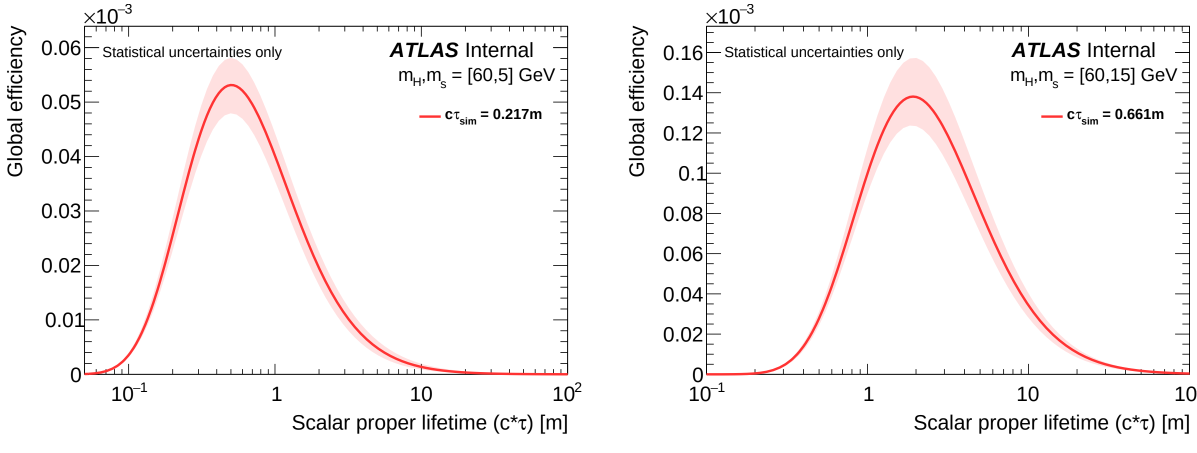

(a) (b)

Figure 7.8: Extrapolated global signal efficiencies for samples with $m_{\Phi} = 60$ GeV. Uncertainties are statistical, stemming from the efficiencies input into the extrapolation

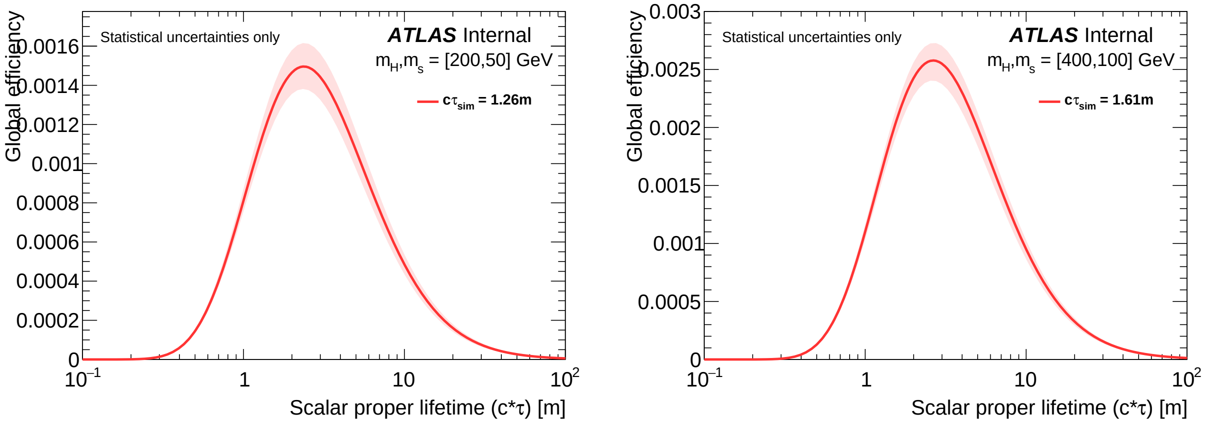

(a) (b)

Figure 7.9: Extrapolated global signal efficiencies for samples with (a) $m_\Phi = 200$ GeV and (b) $m_\Phi = 400$ GeV. Uncertainties are statistical, stemming from the efficiencies input into the extrapolation

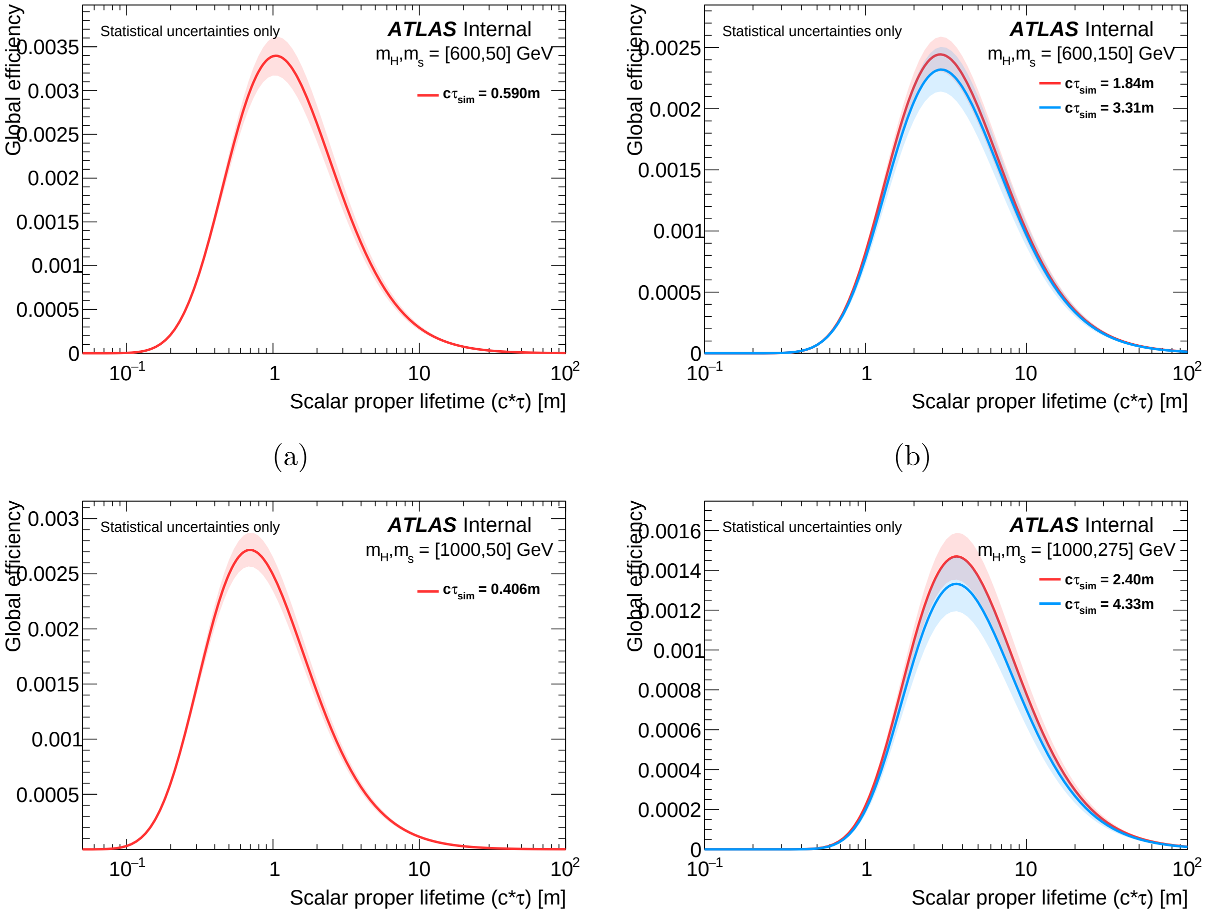

(a) (b)

(c) (d)

Figure 7.10: Extrapolated global signal efficiencies for samples with (a-b) $m_\Phi = 600$ GeV and (c-d) $m_\Phi = 1000$ GeV. Uncertainties are statistical, stemming from the efficiencies input into the extrapolation

Chapter 8

Results

This chapter presents the expected and observed limits for the two MS vertex search for scalar bosons to displaced hadronic jets in section 8.1, and summarizes the results of the analysis in section 8.2.

8.1 Limit setting

Upper limits on the production cross section times branching fraction were derived using the CL_s prescription [53, 54], which quantifies the compatibility of the data with a given theory. It is a modified frequentist approach wherein the confidence level observed for the signal+background hypothesis, $CL_s + b$, is normalized to the confidence level observed for the background-only hypothesis, CL_b:

$$CL_s \equiv \frac{CL_{s+b}}{CL_b}. \tag{8.1}$$

The signal hypothesis is then considered excluded at confidence level CL when $1 - CL_s \leq CL$. This method is implemented with the pyhf package [55, 56] using a profile likelihood function [57].

For benchmark samples with $m_\Phi \neq 125$ GeV, upper limits – that is, exclusion limits at 95% confidence level – were set on $\sigma \times B$, where B represents the branching fraction for $\Phi \to ss$ assuming 100% branching fraction of s decays into fermion pairs. For scalar boson benchmark samples with $m_\Phi = 125$ GeV, upper limits were set on $\sigma/\sigma_\mathrm{SM} \times B$, where σ_SM is the SM Higgs boson production cross section for pp collisions at $\sqrt{s} = 13$ TeV, 48.61 pb [58].

The sources of systematic uncertainty are listed in table 8.1. The uncertainties associated with lifetime extrapolation are different for each signal mass point, the details of which are shown in table 8.2. Two other sources were considered: one from the simulation of pileup interactions and another from the PDF used to generate signal MC events. These were evaluated by varying the pileup/PDF weights by their respective $\pm 1\sigma$ systematic uncertainties and calculating the resultant change in trigger efficiency. Both were determined to be negligible.

All systematic uncertainties were taken into account as nuisance parameters.

Source	Systematic uncertainty		Details
	Barrel	Endcaps	
Trigger mismodelling	20%	24%	Section 6.1
Vertex mismodelling	11%	13%	Section 6.3
Luminosity measurement	1.7%		Section 4.2
Lifetime extrapolation	See table 8.2		Section 7.4

Table 8.1: Summary of systematic uncertainties considered in the two vertex search.

m_Φ	m_s	Systematic uncertainty
125	5	14.8%
125	15	6.5%
125	35	8.4%
125	55	10.8%
60	5	7.9%
60	15	8.5%
200	50	10.9%
400	100	7.9%
600	50	9.2%
600	150	9.5%
600	275	21.7%
1000	50	1.9%
1000	275	6.5%
1000	475	30.2%

Table 8.2: Summary of systematic uncertainties associated with the lifetime extrapolation procedure.

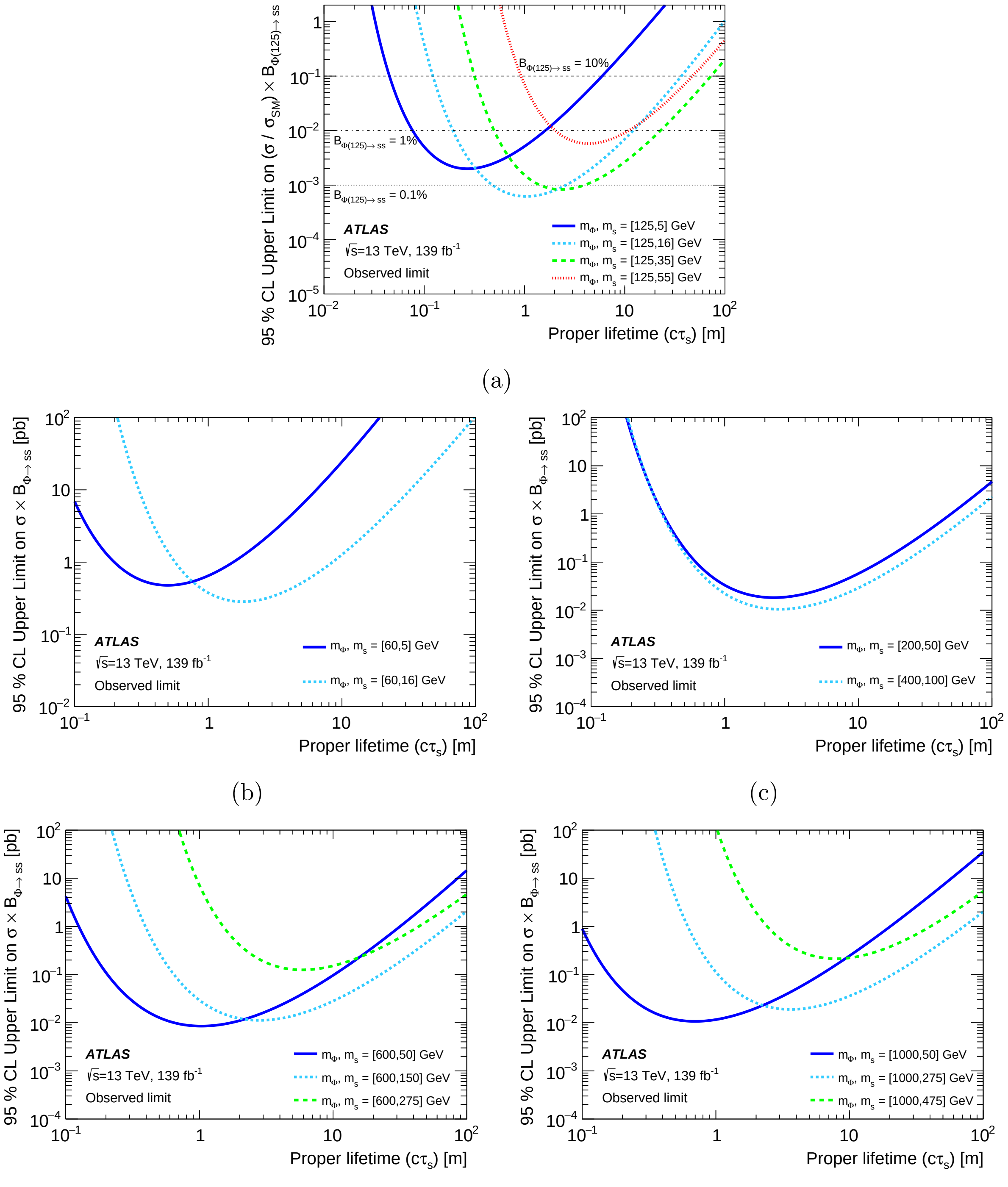

(a)

(b) (c)

(d) (e)

Figure 8.1: Observed 95% CL exclusion limits for all HSS MC mass points.

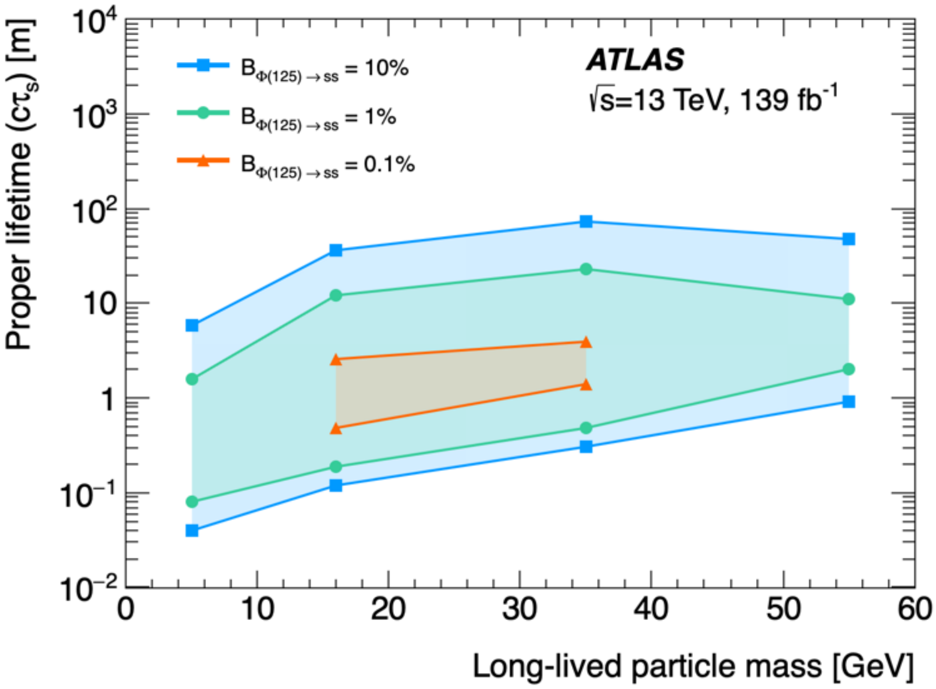

Figure 8.2: A 2D limit plot showing the exclusion ranges at 95% CL with a production cross-section times branching fraction equal to 10%, 1%, and 0.1% as a function of scalar mediator mass and mean proper lifetime.

Figure 8.1 presents the observed 95% CL exclusion limits for all HSS samples. Figure 8.2 summarizes the 95% CL exclusion ranges for all HSS mass points where the production cross-section times branching fraction is equal to 10%, 1%, and 0.1%, with interpolation between the mass points. The scalar LLP mass is given on the x-axis, and the LLP mean proper lifetime is given on the y-axis.

The exclusion limits on LLP mean proper lifetime for the HSS mass points with $m_{\Phi} = 125$ GeV are summarized in table 8.3 for the branching fractions $B(\Phi(125) \rightarrow ss) = 10\%$, 1%, and 0.1 %.

8.2 Summary

This thesis details the search for events with two displaced vertices from pair-produced long-lived particles decaying into hadronic jets in the ATLAS muon spectrometer. The search used 139 fb^{-1} of pp collision data at $\sqrt{s} = 13$ TeV, collected during 2015–2018, which is the full Run 2 data-taking period at the LHC. The expected background, estimated with a

Table 8.3: Ranges of mean proper lifetime excluded at 95% CL for scalar boson benchmark models with $m_{\Phi} = 125$ GeV, assuming a production cross-section times branching fraction equal to 10%, 1% and 0.1% of the SM Higgs boson production cross-section [58].

$\Phi(125) \to ss$	Excluded $c\tau_s$ range for s [m]		
m_s [GeV]	$B = 0.1\%$	$B = 1\%$	$B = 10\%$
5	–	0.08–1.6	0.04–5.9
15	0.49–2.1	0.18–10.8	0.11–32.9
35	1.4–3.9	0.48–22.6	0.30–71.3
55	–	2.1–7.8	0.84–40.2

data-driven method, was 0.32 ± 0.05 events and 0 events were observed in the signal region. Therefore, exclusion limits were set on the LLP production cross-section as a function of its proper lifetime for a benchmark model where a scalar mediator, which can be either SM Higgs-like with a mass of 125 GeV or another short-lived scalar with higher or lower mass, can decay to two long-lived scalars. For the 125 GeV Higgs boson, branching fractions above 10% are excluded at 95% confidence level for LLP lifetimes ranging from 4 cm to 71.3 m. This analysis also offers the first exclusion limits for branching fractions below 0.1% and for the decay of LLPs into $t\bar{t}$ in the ATLAS muon spectrometer.

Chapter 9

Future work

While this analysis yielded no discovery, the search for LLPs is far from over. The exploration of the lifetime frontier is just beginning and gaining community interest, and plenty of parameter space remains unconstrained. As the LHC prepares for Run 3, existing LLP search teams are refining their strategies and techniques in order to handle higher luminosity and pileup and maximize their sensitivity. At the same time, community members are brainstorming new searches and new models to work on. For the search for displaced hadronic jets in the ATLAS muon spectrometer, some next steps are clear and already underway while others need further consideration and development.

9.1 Next steps in Run 2

While the two vertex search has been completed with full Run 2 data, the one vertex search remains in progress. In that search, exactly one displaced vertex is required to be reconstructed in the muon spectrometer rather than two. When interpreting in terms of the benchmark model described in section 2.3.1, or any other model with pair-produced LLPs, this selects events where either the second LLP decays in the HCal, or it escapes the ATLAS detector completely before it decays. While this greatly increases the number of background events that pass the signal selection, it also significantly increases the search's sensitivity to higher LLP lifetimes. It also has the advantage that it can be interpreted in terms of benchmark models with a single LLP, without pair-production. The one-vertex search was introduced in Run 2 and performed with 2015-2016 data.

Given the higher background, the one vertex search requires a more sophisticated background estimation method. The method employed is called the ABCD method, which uses two uncorrelated variables to form a plane as in fig. 9.1. Both of the variables chosen should have good separation of signal and background, so that the signal events end up clustered into one area of the plane. The plane is divided into four regions such that one region contains the majority of the signal events, and is then labeled region A while the background-dominated regions are labeled B, C, and D. Since the variables forming the plane are uncorrelated, the expected number of background events entering into region A is given by

$$N_A^{\text{expected}} = N_B \times \frac{N_C}{N_D}. \tag{9.1}$$

If the method is working, the observed number of events in region A matches that expected within statistical uncertainty. The ABCD plane is tested in a validation region, where no signal events are present, to make sure that the method works as expected and eq. (9.1) gives an accurate prediction of events in region A. Once the method is validated, it is repeated in the signal region. Region A in the signal region remains blinded until all calculations and uncertainties are completed and trusted.

For the one vertex search using the full Run 2 dataset, a BDT is being introduced into the analysis. The BDT classifies displaced vertices in the muon spectrometer as signal- or background-like, and the BDT output score is used as one of the variables defining the ABCD plane. The validation region is defined by events with missing energy less than 40 GeV, since signal events are expected to have MET $>$ 40 GeV.

9.2 Next steps in Run 3

Run 3 is projected to record 160 fb^{-1} of pp collision data from 2022 to 2025. Higher statistics naturally leads to higher sensitivity, but there is also an opportunity to increase sensitivity through modifications to the analysis strategy. The transition to Run 3 is also an ideal moment to implement changes to the vertex reconstruction algorithm to optimize its performance.

Since the MS vertex reconstruction algorithm uses the MS in a way that it was not designed for, the efficiency of reconstructing vertices from hadronic activity is quite low.

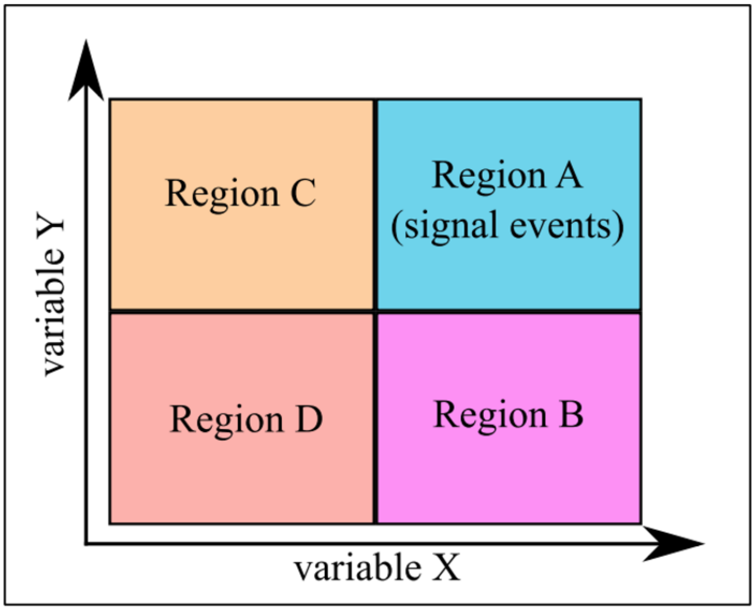

Figure 9.1: Basic layout of an ABCD plane.

Moreover as luminosity and pileup increase, the number of background vertices from pileup will increase as well. It is crucial, then, to ensure that the GVC remain optimized for future run conditions. In particular, the ΔR values used when applying isolation cuts should be revisited.

The reconstruction algorithm counts and saves the number of MDT, RPC, and TGC hits that are within a $\Delta R = 0.4$ cone around the vertex. It would be beneficial to also count and save how many of those hits are *before* the vertex – meaning $R_{hit} < R_{vtx}$ in the barrel and $|z_{hit}| < |z_{vtx}|$ in the endcaps – and how many are *after* the vertex – meaning $R_{hit} > R_{vtx}$ in the barrel and $|z_{hit}| > |z_{vtx}|$ in the endcaps. Most hits are expected to be after the vertex for signal vertices, while punch-through vertices should have a more equal distribution of hits before and after. The lack of precision in the reconstructed vertices' R and z values mean these variables may not offer perfect discrimination between signal and background, but it is likely to give some separation and should be studied.

9.3 Additional considerations

The search should also be reinterpreted in terms of other benchmark models. For models with the same basic signature in the detector (pair-produced LLPs decaying to hadronic jets with no other associated activity), for example the baryogenesis model described in [59], this reinterpretation should be quite easy because the analysis code has been preserved in the RECAST (Request Efficiency Computation for Alternative Signal Theories) framework [60]. This infrastructure is designed to capture not only the analysis code itself, but also the environment in which it is run, and the included workflow definition ensures that reinterpretation with any new signal model is an automated process. A lot of work has already been done with the baryogenesis model, including the generation of MC samples for select mass points and decay modes. However, it was discovered that the predicted global efficiency derived from toy MC samples did not match the efficiency extracted from the signal MC samples. This needs to be understood before proceeding; it is possible that there is a correlation present, invalidating the assumption that the two vertices can be treated independently, but further study is needed.

Modifications to the existing signal selection would extend sensitivity to models with other signatures. One of the most interesting models to consider in future features a long-lived Heavy Neutral Lepton (HNL) as seen in fig. 9.2. HNL theories propose the existence of at least two new right-handed neutrinos, and can simultaneously address the problems of neutrino mass, matter-antimatter asymmetry, and dark matter [61]. With minor modifications, the analysis described in this thesis would have sensitivity to a displaced HNL semileptonic decay in the muon spectrometer. Primarily, this signal model would feature only one displaced vertex, so the one vertex search described in section 9.1 should be used. The model also has a prompt lepton, which could be used for triggering as well as to reduce background.

9.4 Dedicated detectors

There are several limitations to the LLP searches that are currently being performed at the LHC. First, the detectors currently in operation at the LHC, like the ATLAS detector, were not designed with LLP searches in mind. As a natural consequence, their fundamental sensitivity to LLP models is limited. First, the detector surrounds the interaction point closely in order to capture as much information from the output of the pp collision as possible, which entails an incredible amount of QCD activity. Studying that activity is of course interesting, and accounts for a significant portion of the ATLAS physics program – however, it represents the primary background in a LLP search. LLP searches benefit when the QCD

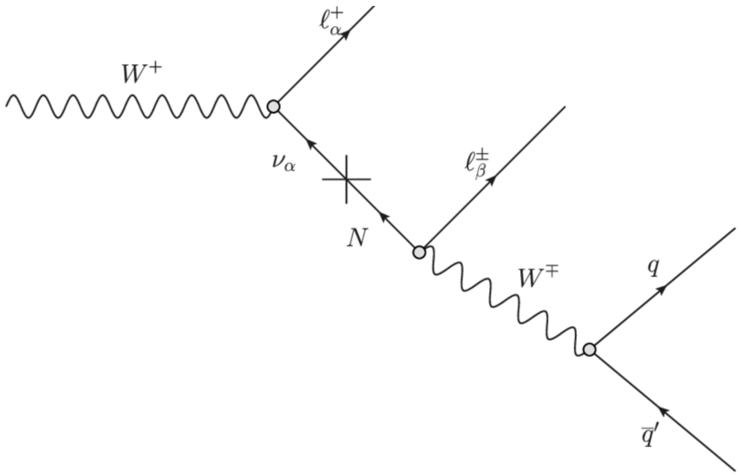

Figure 9.2: A model where a W boson decays into a long-lived HNL N by mixing with a neutrino. The HNL decay can then be leptonic (two charged leptons and a nuetrino) or semileptonic (a charged lepton and two quarks) [61].

backgrounds can be suppressed as much as possible. Second, the physical size of the detector is limiting. Any neutral LLP that decays outside of the ATLAS detector will not be seen at all. Its energy may contribute to the event's MET calculation, but the particle and its decay cannot be discovered or characterized unless it is observed within the detector. This is a problem since the detector is on the order of 10 m in radius, while the upper limit on LLP lifetime is 10^7 as mentioned in section 2.3. If there are LLPs with average mean lifetimes lurking around that 10^7 m limit, it is unlikely that an ATLAS-based analysis would ever have the sensitivity to see the few decays that would occur within the detector above the large QCD background rate.

Additionally, the standard triggers and reconstruction algorithms within the ATLAS hardware and software frameworks are developed with SM signals in mind, and often have pointing requirements that ensure the activity originates directly from the interaction point. Since LLP signatures, i.e. displaced decays, do not fulfill this requirement by definition, activity from LLP decays has a higher probability of being deemed uninteresting and not being recorded than SM-based activity. However it is not simple to remove the pointing requirement, as this would accept too much background and create an issue for the volume of data to be stored and analyzed. (Note, however, that in Run 3 additional Large Radius Tracks (LRT) will be reconstructed and stored in order to study displaced activity in the ID.) Reconstruction algorithms for displaced activity often need to save non-standard objects or use the standard objects in an unconventional way, and this lack of optimization results in a significant loss of efficiency for these analyses.

As more attention and interest turns toward exploration of the lifetime frontier, it has become clear that a thorough investigation of the parameter space necessitates one or more detectors dedicated specifically to LLP searches. There are currently many proposals for dedicated LLP detectors based at CERN: MATHUSLA [62], SHiP [63], CODEX-b [64], AL3X [65], and ANUBIS [66] to name just a few. Some, like MilliQan [67] and FASER [68], have already received funding and are being built. The details of the experimental setups differ, but there are some commonalities between them that address the limitations of current searches as described above. The detectors search for LLPs produced in pp collisions, but they are placed some distance away from the interaction points. This has two advantages: the experiment has sensitivity to longer LLP lifetimes, and the intervening material provides shielding from the QCD backgrounds emanating from the collision point. Of course, the design needs to maximize its angular acceptance for LLPs produced at the interaction point, which means that when a detector is located farther away from that point it needs to be larger. The exact size varies between detectors depending on location and expected background rate.

Details for the proposed MATHUSLA detector and its test stand are found in appendix B.

Appendix A

MDT hit selection in the MS vertex reconstruction algorithm

The MS vertex reconstruction algorithm was developed in Run 1 and has undergone few changes since. In her thesis, Heather Russell identified a potential bug in the selection of MDT hits as tracklet seeds [29]. This stage of the reconstruction, described fully in section 5.4.1, proceeds as follows.

The MDT tubes are uniquely numbered within the multilayer as illustrated in fig. A.1. MDT hits are sorted in order of increasing tube number. Three hits within the multilayer form a seed when they fulfill the following criteria, where $R = \sqrt{x^2 + y^2}$:

- Hits 1 and 2 are in the same or sequential layers
- Hit 3 is in the same layer or one higher than hit 2, but not in the same layer as hit 1
- In the barrel, $|z_1 - z_2| < 50$ mm and $|z_1 - z_3| < 80$ mm
- In the endcaps, $|R_1 - R_2| < 50$ mm and $|R_1 - R_3| < 80$ mm

To understand the potential bug, consider fig. A.3. This hit pattern can successfully form a tracklet seed, as it fulfills all criteria listed above. In particular, $|z_1 - z_2| = 30 < 50$ mm and $|z_1 - z_3| = 45 < 80$ mm. (This is assuming the MDT chamber is located in the barrel. The argument is exactly the same for any hit pattern in the endcaps except that $z_i \to R_i$). It is logical, then, that any reflection of this same pattern, as shown in fig. A.3, should also form an acceptable hit pattern. This is not the case, however – the hit pattern in

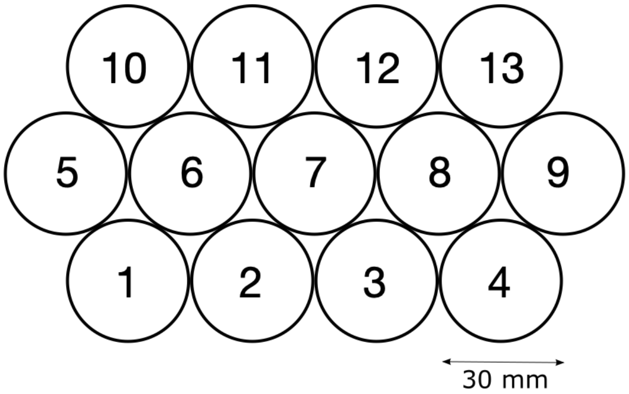

Figure A.1: Illustration of the MDT tube numbering scheme within a single multilayer.

fig. A.3c has $|z_1 - z_2| = 75 > 50$ mm and fails the criteria. This is a consequence of the fact that the MDT tube numbering is chosen to be in a specific direction, and hits are labelled sequentially by tube number rather than being ordered by distance from hit 1.

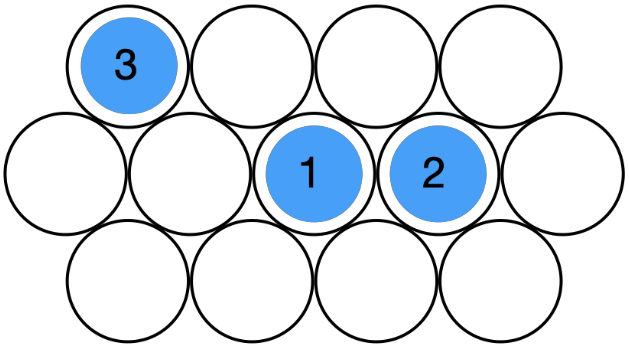

Figure A.2: A hit pattern that fulfills all criteria to form a tracklet seed.

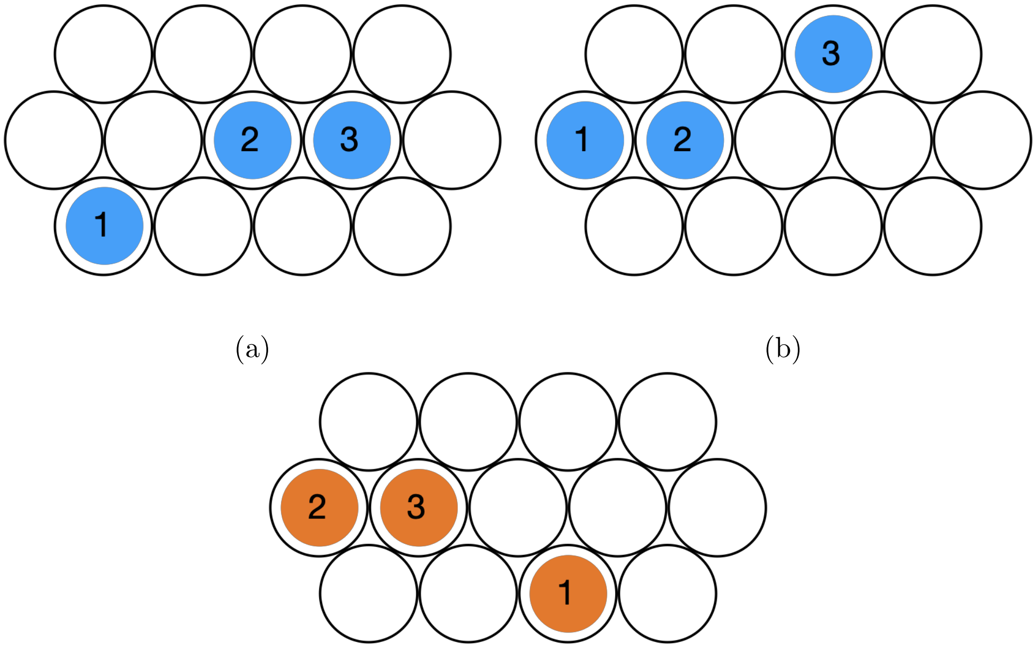

(a)

(b)

(c)

Figure A.3: Hit patterns that are reflections of the pattern in fig. A.2. The patterns in appendix A fulfill the criteria to form a tracklet seed, but the pattern in fig. A.3c does not.

Some hit patterns are far more likely to occur than others, however, so the fact that some patterns are not selected as seeds does not necessarily translate to a significant loss in reconstruction efficiency. A careful study of the seeds that *are* selected in the algorithm gives insight into the seed selection process, which can then be extrapolated to calculate a rough estimation of how many “good” seeds are not being selected due to this labeling bug.

To begin, it is crucial to note that the direction in which MDT tubes are labeled depends on the location of the MDT chamber within the detector. In the barrel, tube number increases as $|z|$ increases, while in the endcaps, tube number increases as R increases. This means that a certain set of combinations will be selected in the endcaps and the $+\eta$ half of the barrel, where tube numbering increases as the z/R coordinate becomes more positive, and a slightly different set of combinations will be selected in the $-\eta$ half of the barrel, where tube numbering increases as the z coordinate becomes more negative.

Since any LLP that decays in the MS will have been produced at the IP, its decay products will also have a preferential direction. Specifically, they will usually leave a hit pattern where MDT hits 2 and 3 have larger $|z|$ or R values than hit 1. This is illustrated in fig. A.4.

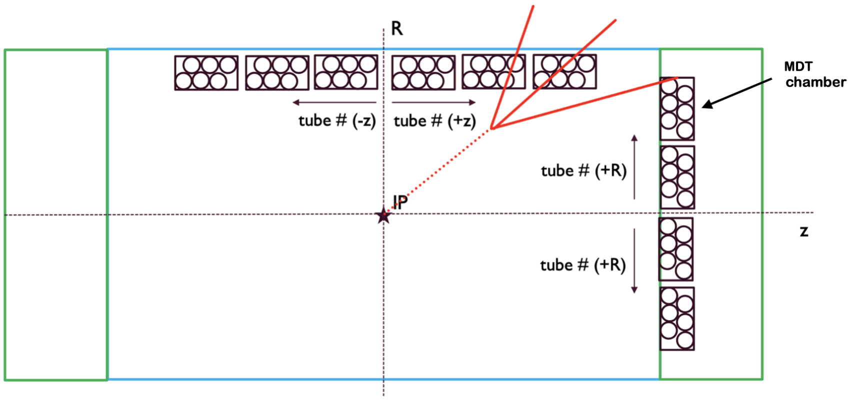

Figure A.4: Illustration of how the direction of increasing MDT tube number varies depending on the location the MDT chamber in the ATLAS detector. A LLP decay is also depicted in red to show the preferential direction of its decay products.

In order to quantify how often hit patterns occur, the values (d_{12}, d_{13}) are studied where $d_{1j} = z_j - z_1$ in the barrel and $R_j - R_1$ in the endcaps for $j \in \{2, 3\}$. If the hit pattern has three hits in three layers, then the labeling of the hits is unique and only one (d_{12}, d_{13}) will be associated with that pattern. If the pattern has three hits in only two layers, then it will have one value of (d_{12}, d_{13}) when it occurs in the $+\eta$ barrel or endcaps and a different value when it occurs in the $-\eta$ barrel. This is illustrated in fig. A.5. In either case, however, any given (d_{12}, d_{13}) corresponds to exactly one pattern. Therefore, if a hit pattern has been accepted as a potential seed, i.e. it has passed all the criteria listed above, then (d_{12}, d_{13}) is enough to uniquely identify it.

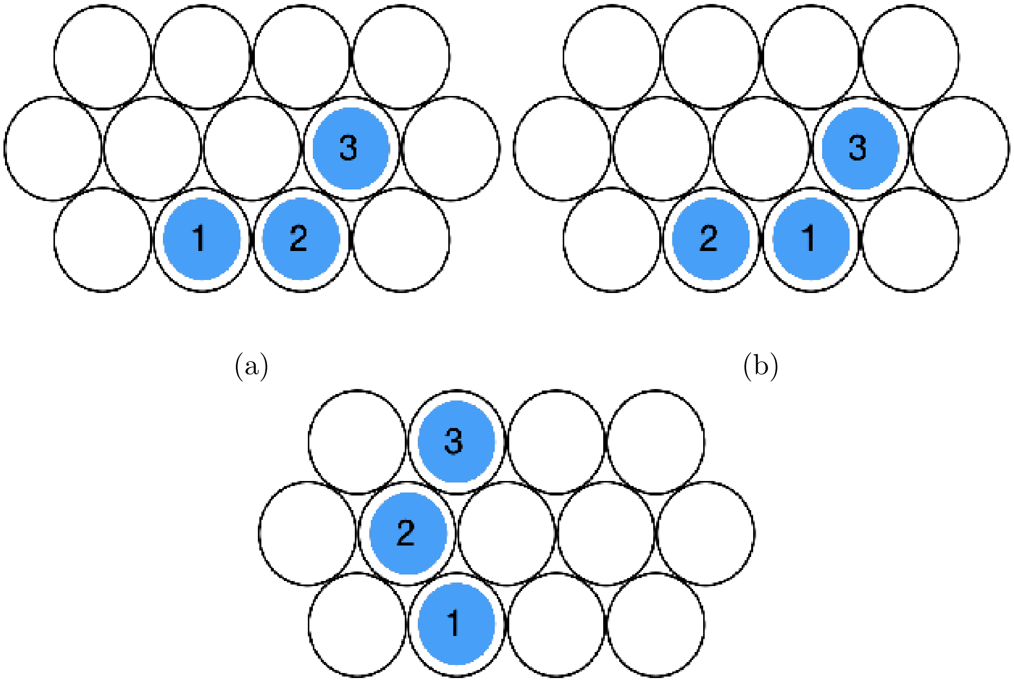

(a) (b)

(c)

Figure A.5: (a) shows the hit labels for a hit pattern in the $+\eta$ barrel or endcaps, where $(d_{12}, d_{13}) = (30, 45)$. (b) shows the hit labels for the same hit pattern in the $-\eta$ region of the barrel, where $(d_{12}, d_{13}) = (-30, 15)$. (c) shows a hit pattern with three hits in three layers, where$(d_{12}, d_{13}) = (-15, 0)$ in all regions.

As a consequence, some hit patterns that are rejected as tracklet seeds in the $+\eta$ region of the barrel or in the endcaps are accepted in the $-\eta$ region of the barrel, and vice versa. Moreover, in these cases, the hit patterns are always accepted in the region where the hits are arranged in the preferential direction according to LLP decay products. When a particular hit pattern that appears logically "good" is rejected in all regions, a similar pattern that is selected by the algorithm can be used to estimate its frequency of occurrence. By creating a list of patterns that are not accepted in a certain region, and by noting that hit patterns that conform to the decay products' preferential direction are about 10 times more likely to occur than patterns arranged in the opposite direction, it is estimated that 0.03% of seeds are lost in the barrel and 0.01% are lost in the endcaps. This is deemed completely negligible, and similar behavior is seen between data and MC, so the algorithm has not been changed.

Appendix B

MATHUSLA

As explained in section 9.4, many dedicated long-lived particle detectors have recently been proposed and are vying for funding. MATHUSLA, or the MAssive Timing Hodoscope for Ultra-StabLe pArticles, is one such detector. The concept was first proposed in 2016 [69], and work commenced soon after to create a test stand for proof-of-concept while the design for the full detector was developed in parallel. The most updated plans for the full detector are reported in [70], and a summary of the test stand operation and results is given in [71].

B.1 Detector design

The MATHUSLA design has a large detector with an air decay volume and several tracking layers located at the LHC above and slightly offset from the CMS interaction point, as shown in fig. B.1. The structure height approaches 40 m, set with 21 m underground and at least 12 m above ground. There is a set of five tracking layers at the top of the detector, each separated by 1 m, and an additional two layers set 5 m below the uppermost set. Two more tracking layers are located at the floor of the detector, again separated by 1 m. All tracking layers use extruded scintillator technology. The experiment will search for decays that happen inside the detector volume, so the tracking layers in the floor can act as a veto for any SM activity originating from the IP. In total, the LLP decay volume is about 25 m tall. The detector footprint is 100 m × 100 m, composed of 100 9 m × 9 m modules, with an additional 100 m × 30 m assembly area on one side to assist in construction and maintenance.

The projected sensitivity of MATHUSLA for LLPs with mass $m_x = 20$ GeV over the course of the HL-LHC is shown in fig. B.2, where the predicted sensitivity of the one-vertex search in the ATLAS muon spectrometer (described in section 9.1) is included for comparison. This plot assumes both perfect efficiency for reconstructing LLP decays that occur within the MATHUSLA decay volume and zero background (after cuts are applied). These assumptions are not unreasonable for hadronic decays, which is MATHUSLA's primary targeted signal, though the details depend on the final design of the detector. Sensitivity to other final states, for example leptonic decays, are still under study.

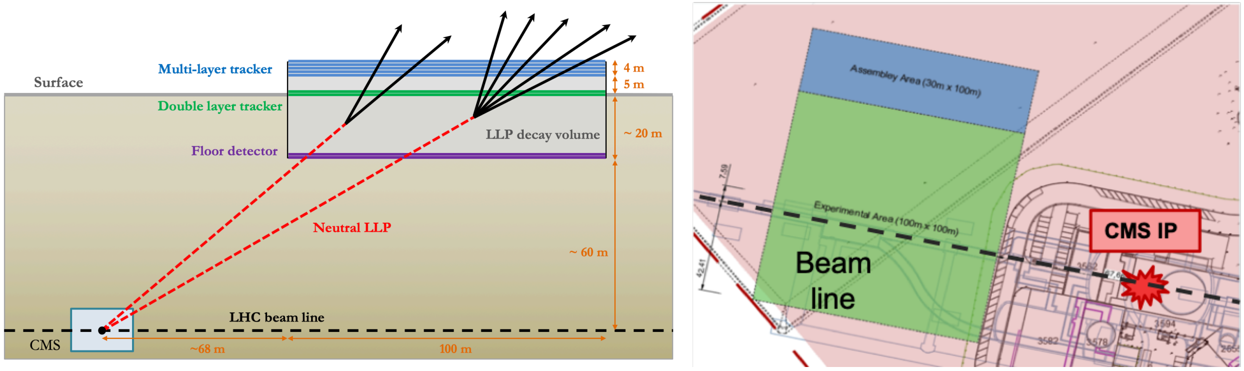

(a) (b)

Figure B.1: (a) Side and (b) aerial view of the proposed location and layout of the MATHUSLA detector.

B.2 Test stand

The MATHUSLA test stand took data in 2018 at P1, on the surface almost directly above the ATLAS interaction point. The test stand, shown in fig. B.3, had a 2.5×2.5 m^2 footprint and a height of 6.5 m. The top and bottom detector layers were made out of scintillators, with 6 layers of RPCs in between. The scintillator layers were used to form two triggers – a "downwards" trigger compatible with a downwards-traveling particle and an "upwards" trigger compatible with an upwards-traveling particle – and the RPCs were used in combination with the scintillators to reconstruct tracks with precision, using both timing and spatial information.

Most tracks reconstructed in the detector came from cosmic rays, which have a flux of approximately 1 per cm^2 per minute at the earth's surface, traveling downwards. Upwards

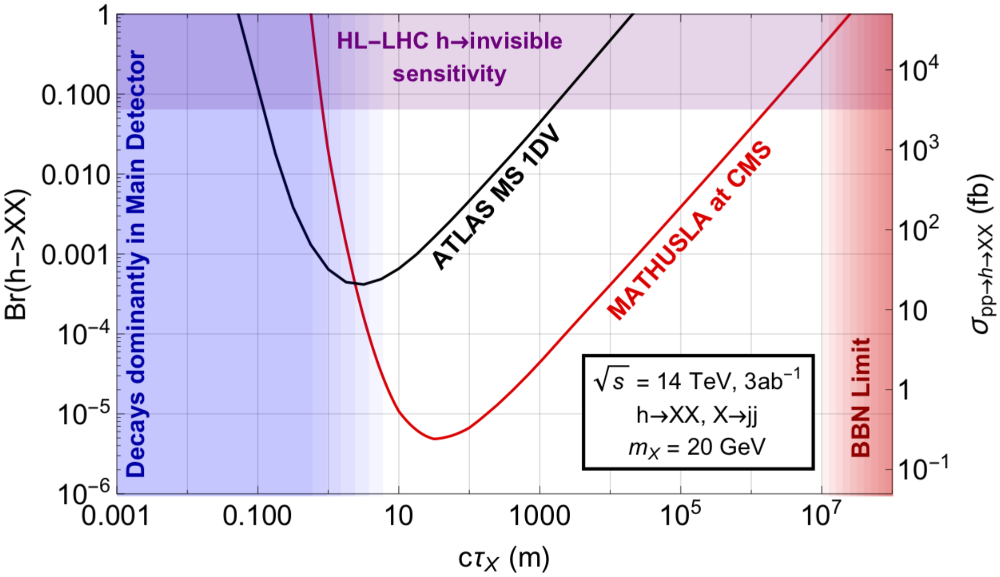

Figure B.2: Projected sensitivity of the MATHUSLA detector for a LLP with mass $m_X = 20$ GeV, with data collected over the course of the HL-LHC. The projected sensitivity of the one-vertex search in the ATLAS muon spectrometer under the same conditions is shown for comparison.

tracks were reconstructed with angles consistent with particles originating from the ATLAS IP. Cosmic rays also contributed to upwards tracks through inelastic backscattering, which came from cosmic muon decays or from interactions with the test stand material and had a more uniform angular distribution. The angular distribution of upwards-going tracks reconstructed in data is shown in fig. B.4, represented with the black markers. For comparison, the simulated angular distributions of particles originating from the ATLAS IP are shown in orange and the predicted distributions of cosmic ray inelastic backscattering are shown in blue.

B.2.1 Implementation of trigger and DAQ system

The implementation of a trigger system is a delicate balance between maximizing signal acceptance and minimizing background acceptance, and making sure that the total rate remains at a reasonable level. In the MATHUSLA test stand, particles that traversed the entirety of the detector can be separated into two categories: upwards-going, and downwards-going. The separation is crucial, as proper identification was necessary in order to define and understand the different kinds of backgrounds that will be present in the full MATHUSLA detector.

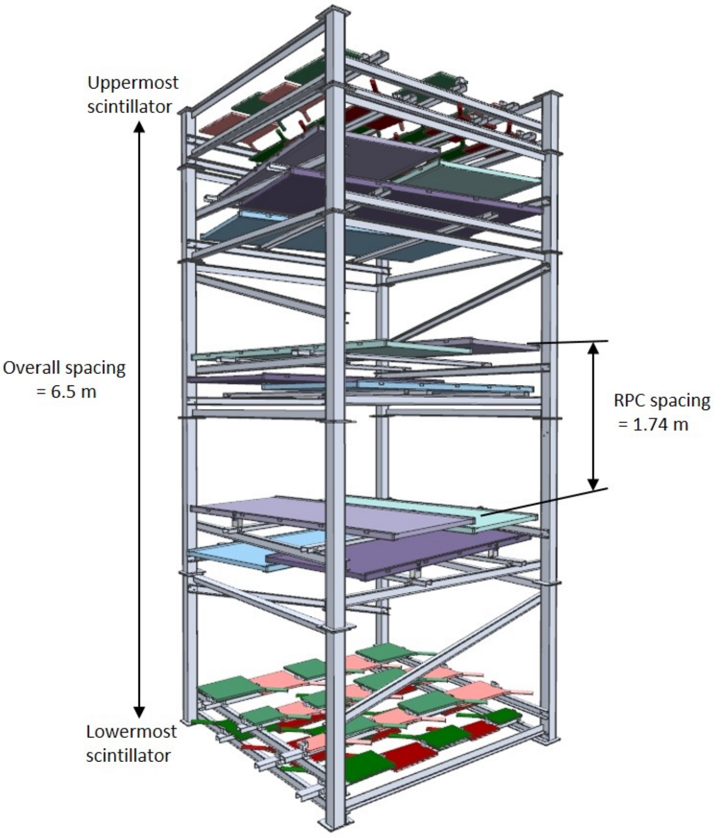

Figure B.3: Layout of the MATHUSLA test stand.

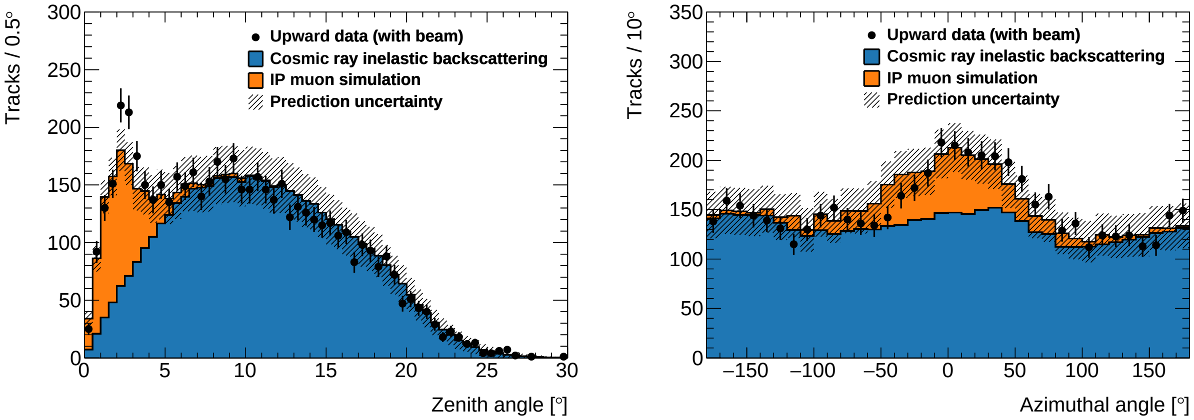

(a) (b)

Figure B.4: Angular distribution of upwards-going tracks as a function of (a) zenith and (b) azimuthal angle in the MATHUSLA test stand, where beam was present in the LHC. Data is represented with black markers, while the simulation of particles originating at the ATLAS IP is shown in orange and the predicted rate of cosmic ray inelastic backscattering is shown in blue.

A particle traveling near the speed of light would traverse the test stand, from the top layer to the bottom or vice versa, in about 18 ns. This time difference was used when creating the upwards- and downwards-going triggers. The bottom layer was composed of 31 individual scintillators, and the top had 28 individual scintillators. The PMT signal from each of the scintillators was split, with one half going to an ADC (Analog to Digital Converter) to read out charge information and the other half entering a discriminator to form a logic pulse. This logic pulse is again split, where one half goes to a TDC (Time to Digital Converter) input to record time information for each scintillator channel. The other half is put into a coincidence unit, where the logical OR of all signals from the upper scintillators result in a single pulse for the upper plane, and the logical OR of all signals from the lower scintillators similarly give a single pulse for the lower plane. The downwards-going trigger is formed by delaying the signal from the upper plane by 18 ns before putting it into a logical AND with the signal from the lower plane. The upwards-going trigger has the opposite procedure; it is formed by delaying the signal from the lower plane by 18 ns before putting it into a logical AND with the signal from the upper plane. The triggers then act as a gate for the ADC, TDC, and Local Station (which controls the RPC readout), allowing their information to be read out when a trigger has fired.

B.2.2 Timing calibration

Use of timing information is crucial in reliably reconstructing good tracks and distinguishing upwards-going tracks from downwards-going. Therefore, it was necessary to ensure that the timing was consistent across all detector elements in the test stand. Two forms of timing calibration were applied; one addressed characteristic timing offsets between detector elements, and one addressed time slewing.

Characteristic offsets

There was a delay from the time that a particle crossed through a detector to the time that the hit was registered in the TDC, and that delay could be different for each detector because of its dependence on factors such as HV setting, drift time within the detector, and cable lengths. To use the timing appropriately, the relative delays between all detectors had to be understood.

This calibration is performed using downwards cosmic rays. For all downwards tracks reconstructed with hits in detectors i and j (where i and j can be scintillators or RPC pads), a histogram is filled with the time difference Δt, defined as:

$$\Delta t = t_i - t_j - t_{\mathrm{TOF},ij} \tag{B.1}$$

where t_i is the time associated with the hit in detector i, t_j is the time associated with the hit in detector j, and $t_{\mathrm{TOF},ij}$ is the expected time of flight between the two detectors, given a particle traveling near the speed of light. Over the course of a data run, a Δt histogram can be filled for each detector pair combination (although some will be empty by geometrical constraints) and fit with a Gaussian. If all delays between detectors were the same, each Gaussian fit should have a mean at $\Delta t = 0$ ns. A shift in the distribution indicates that there is a difference in the timing offsets of detectors i and j.

Since this method only provides information on the relative time differences of the offsets, one scintillator in the top plane was arbitrarily selected to have the "default" time delay, which was defined to be 0 ns. All other delays were then calculated with respect to the default.

To understand how these delays were calculated, consider the simplified system of two scintillator planes (ignoring the RPCs). With 28 scintillators in the upper plane and 31 scintillators in the lower plane, there are $28 \times 31 = 868$ mean time difference measurements and $28 + 31 = 59$ time offsets to calculate, with one of those being defined as 0 ns. This leads to the over-constrained matrix equation

$$A\Delta = b \tag{B.2}$$

where Δ is the vector of 59 time offsets, b is the vector of 868 time difference measurements and A is the 868×59 matrix specifying the counters involved in each measurement. The solution is given by

$$\Delta = \left(A^T E^{-1} A\right)^{-1} \left(A^T E^{-1}\right) b \tag{B.3}$$

where E is the error matrix for the time difference measurements, which can be extracted from the width of the Gaussian fits in the time difference histograms. The numbers presented here refer to the simplified system where only scintillators are considered, but the argument can be naturally extended to include the RPC pads as well.

Time slewing

The timing calibration also included a correction for time slewing. Time slewing refers to the phenomenon where hit time can be affected by the charge of the pulse, as seen in fig. B.5 — the larger the pulse, the more quickly it crosses the discriminator threshold and the sooner that hit registers in the TDC. This calibration could only be applied in the scintillators, as no charge information was available for RPC pads.

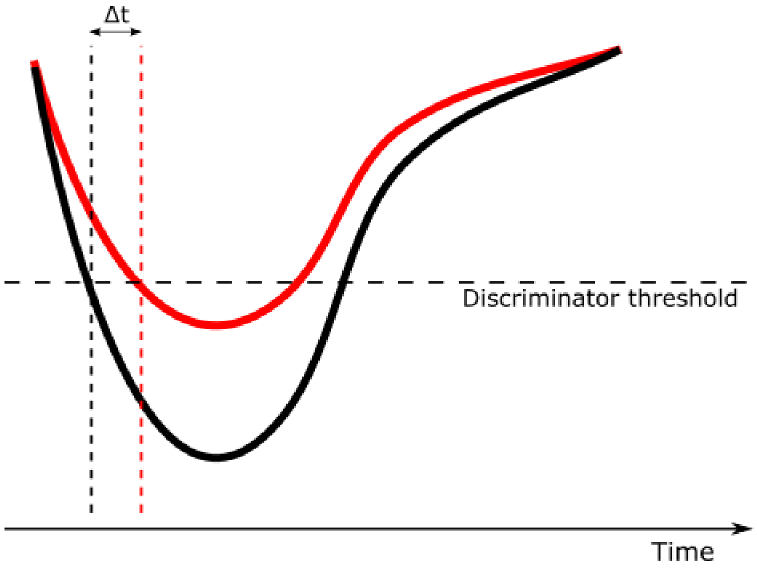

Figure B.5: Schematic illustrating the effect of time slewing.

The time slewing effect is easily seen in fig. B.6, where TDC counts are shown with a strong dependence on ADC counts for hits in a particular scintillator channel. A function of the form

$$f(c) = \frac{[0]}{[1] + x} + [2] \tag{B.4}$$

was fit to this distribution for each scintillator channel, and the parameters of this function were then used to provide a correction based on pulse height.

After both forms of timing calibration were applied, resolutions of 3 ns and 4 ns were achieved for the scintillators and RPCs respectively.

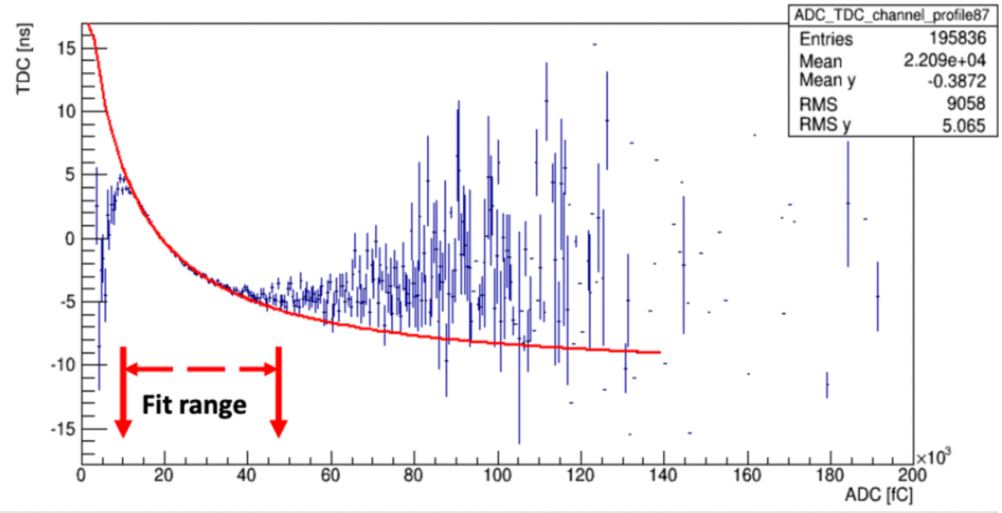

Figure B.6: The TDC counts as a function of ADC counts for hits in a particular scintillator channel in the MATHUSLA test stand. Credit: Yubo Han

B.3 Current and future work

The results of the test stand successfully provided basic proof-of-concept for the full MATHUSLA detector, as all background sources were considered to be well understood with manageable rates. Therefore, a Letter of Intent for the MATHUSLA detector was presented to the LHC Experimental Council in August of 2018 [72]. A theoretical white paper detailing the physics motivation for building MATHUSLA was also provided in 2018 [73]. An updated version of the Letter of Intent was given in 2020 [70].

References

[1] Michael Schwartz. *Quantum Field Theory and the Standard Model*. Cambridge University Press, 2013.

[2] Michael E. Peskin and Daniel V. Schroeder. *An Introduction to Quantum Field Theory*. CRC Press, 2018.

[3] Ivan Melo. "Higgs potential and fundamental physics". In: *European Journal of Physics* 38.6 (Oct. 2017), p. 065404. ISSN: 1361-6404. DOI: `10.1088/1361-6404/aa8c3d`. URL: `http://dx.doi.org/10.1088/1361-6404/aa8c3d`.

[4] Muon $g-2$ Collaboration. "Measurement of the Positive Muon Anomalous Magnetic Moment to 0.46 ppm". In: *Phys. Rev. Lett.* 126 (14 Apr. 2021), p. 141801. DOI: `10.1103/PhysRevLett.126.141801`. URL: `https://link.aps.org/doi/10.1103/PhysRevLett.126.141801`.

[5] LHCb Collaboration. "Measurement of CP-Averaged Observables in the $B^0 \to K^{*0}\mu^+\mu^-$ Decay". In: *Physical Review Letters* 125.1 (July 2020). ISSN: 1079-7114. DOI: `10.1103/physrevlett.125.011802`. URL: `http://dx.doi.org/10.1103/PhysRevLett.125.011802`.

[6] A. D. Sakharov. "Violation of CP invariance, C asymmetry, and baryon asymmetry of the universe". In: *Journal of Experimental and Theoretical Physics Letters* 5 (1967), pp. 24–27.

[7] C. Jarlskog. "Commutator of the Quark Mass Matrices in the Standard Electroweak Model and a Measure of Maximal CP Nonconservation". In: *Phys. Rev. Lett.* 55 (10 Sept. 1985), pp. 1039–1042. DOI: `10.1103/PhysRevLett.55.1039`. URL: `https://link.aps.org/doi/10.1103/PhysRevLett.55.1039`.

[8] Valerii A Rubakov and M E Shaposhnikov. "Electroweak baryon number non-conservation in the early Universe and in high-energy collisions". In: *Physics-Uspekhi* 39.5 (May 1996), pp. 461–502. DOI: `10.1070/pu1996v039n05abeh000145`. URL: `https://doi.org/10.1070/pu1996v039n05abeh000145`.

[9] NASA. *NASA Finds Direct Proof of Dark Matter*. 2006. URL: `https://chandra.harvard.edu/photo/2006/1e0657/`.

[10] Juliette Alimena et al. "Searching for long-lived particles beyond the Standard Model at the Large Hadron Collider". In: *Journal of Physics G: Nuclear and Particle Physics* 47.9 (Sept. 2020), p. 090501. DOI: `10.1088/1361-6471/ab4574`. URL: `https://doi.org/10.1088/1361-6471/ab4574`.

[11] G.F. Giudice and R. Rattazzi. “Theories with gauge-mediated supersymmetry breaking”. In: *Physics Reports* 322.6 (Dec. 1999), pp. 419–499. ISSN: 0370-1573. DOI: 10.1016/s0370-1573(99)00042-3. URL: http://dx.doi.org/10.1016/S0370-1573(99)00042-3.

[12] R. Barbier et al. “R-parity violating supersymmetry”. In: *Phys. Rept.* 420 (2005), p. 1. DOI: 10.1016/j.physrep.2005.08.006. arXiv: hep-ph/0406039.

[13] Csaba Csáki, Eric Kuflik, and Tomer Volansky. “DynamicalR-Parity Violation”. In: *Physical Review Letters* 112.13 (Apr. 2014). ISSN: 1079-7114. DOI: 10.1103/physrevlett.112.131801. URL: http://dx.doi.org/10.1103/PhysRevLett.112.131801.

[14] Z. Chacko, Hock-Seng Goh, and Roni Harnik. “Natural Electroweak Breaking from a Mirror Symmetry”. In: *Phys. Rev. Lett.* 96 (23 June 2006), p. 231802. DOI: 10.1103/PhysRevLett.96.231802. URL: https://link.aps.org/doi/10.1103/PhysRevLett.96.231802.

[15] Zackaria Chacko, David Curtin, and Christopher B. Verhaaren. “A quirky probe of neutral naturalness”. In: *Physical Review D* 94.1 (July 2016). ISSN: 2470-0029. DOI: 10.1103/physrevd.94.011504. URL: http://dx.doi.org/10.1103/PhysRevD.94.011504.

[16] Haiying Cai, Hsin-Chia Cheng, and John Terning. “A quirky little Higgs model”. In: *Journal of High Energy Physics* 2009.05 (May 2009), pp. 045–045. ISSN: 1029-8479. DOI: 10.1088/1126-6708/2009/05/045. URL: http://dx.doi.org/10.1088/1126-6708/2009/05/045.

[17] Matthew J. Strassler and Kathryn M. Zurek. “Echoes of a hidden valley at hadron colliders”. In: *Phys. Lett. B* 651 (2007), p. 374. DOI: 10.1016/j.physletb.2007.06.055. arXiv: hep-ph/0604261.

[18] Bob Holdom. “Two U(1)’s and ϵ charge shifts”. In: *Physics Letters B* 166.2 (1986), pp. 196–198. ISSN: 0370-2693. DOI: https://doi.org/10.1016/0370-2693(86)91377-8. URL: https://www.sciencedirect.com/science/article/pii/0370269386913778.

[19] Paul Langacker. “The physics of heavy Z' gauge bosons”. In: *Rev. Mod. Phys.* 81 (3 Aug. 2009), pp. 1199–1228. DOI: 10.1103/RevModPhys.81.1199. URL: https://link.aps.org/doi/10.1103/RevModPhys.81.1199.

[20] Matthew Baumgart et al. “Non-abelian dark sectors and their collider signatures”. In: *Journal of High Energy Physics* 2009.04 (Apr. 2009), pp. 014–014. ISSN: 1029-8479. DOI: 10.1088/1126-6708/2009/04/014. URL: http://dx.doi.org/10.1088/1126-6708/2009/04/014.

[21] David E. Kaplan, Markus A. Luty, and Kathryn M. Zurek. “Asymmetric dark matter”. In: *Physical Review D* 79.11 (June 2009). ISSN: 1550-2368. DOI: 10.1103/physrevd.79.115016. URL: http://dx.doi.org/10.1103/PhysRevD.79.115016.

[22] J. C. Helo, S. G. Kovalenko, and M. Hirsch. “Heavy neutrino searches at the LHC with displaced vertices”. In: *Physical Review D* 89.7 (Apr. 2014). ISSN: 1550-2368. DOI: 10.1103/physrevd.89.073005. URL: http://dx.doi.org/10.1103/PhysRevD.89.073005.

[23] Brian Batell, Maxim Pospelov, and Brian Shuve. “Shedding light on neutrino masses with dark forces”. In: *Journal of High Energy Physics* 2016.8 (Aug. 2016). ISSN: 1029-8479. DOI: 10.1007/jhep08(2016)052. URL: http://dx.doi.org/10.1007/JHEP08(2016)052.

[24] Matthew J. Strassler and Kathryn M. Zurek. “Discovering the Higgs through highly-displaced vertices”. In: *Phys. Lett. B* 661 (2008), p. 263. DOI: 10.1016/j.physletb.2008.02.008. arXiv: hep-ph/0605193.

[25] Esma Mobs. *The CERN accelerator complex - 2019. Complexe des accélérateurs du CERN - 2019.* General Photo. July 2019. URL: https://cds.cern.ch/record/2684277.

[26] Xabier Cid Vidal and Ramon Cid Manzano. *Buckets and Bunches: Taking a closer look at LHC*. URL: https://www.lhc-closer.es/taking_a_closer_look_at_lhc/0.buckets_and_bunches.

[27] R Bailey and Paul Collier. *Standard Filling Schemes for Various LHC Operation Modes*. Tech. rep. Geneva: CERN, Sept. 2003. URL: https://cds.cern.ch/record/691782.

[28] ATLAS Collaboration. “The ATLAS Experiment at the CERN Large Hadron Collider”. In: *JINST* 3 (2008), S08003. DOI: 10.1088/1748-0221/3/08/S08003.

[29] Heather Russell. “Search for long-lived particles decaying in the muon spectrometer of the ATLAS detector at the LHC”. PhD thesis. University of Washington, 2016.

[30] Lyndon Evans and Lyn Evans. *The Large Hadron Collider: a marvel of technology; 2nd ed.* Physics (EPFL Press). On the cover : Including the discovery of the higgs boson. Lausanne: EPFL Press, 2018. URL: https://cds.cern.ch/record/2645935.

[31] ATLAS Collaboration. “Operation of the ATLAS trigger system in Run 2”. In: *JINST* 15 (2020), P10004. DOI: 10.1088/1748-0221/15/10/P10004. arXiv: 2007.12539 [hep-ex].

[32] ATLAS Collaboration. “Triggers for displaced decays of long-lived neutral particles in the ATLAS detector”. In: *JINST* 8 (2013), P07015. DOI: 10.1088/1748-0221/8/07/P07015. arXiv: 1305.2284.

[33] ATLAS Collaboration. “Search for long-lived neutral particles in pp collisions at $\sqrt{s} =$ 13 TeV that decay into displaced hadronic jets in the ATLAS calorimeter”. In: *The European Physical Journal C* 79.6 (June 2019). ISSN: 1434-6052. DOI: 10.1140/epjc/s10052-019-6962-6. URL: http://dx.doi.org/10.1140/epjc/s10052-019-6962-6.

[34] David Curtin et al. “Exotic decays of the 125 GeV Higgs boson”. In: *Phys. Rev. D* 90.7 (2014), p. 075004. DOI: 10.1103/PhysRevD.90.075004. arXiv: 1312.4992.

[35] J. Alwall and et al. “The automated computation of tree-level and next-to-leading order differential cross sections, and their matching to parton shower simulations”. In: *J. High Energy Phys.* 7 (2014), p. 79. DOI: 10.1007/JHEP07(2014)079. arXiv: 1405.0301.

[36] Torbjorn Sjostrand, Stephen Mrenna, and Peter Z. Skands. “A Brief Introduction to PYTHIA 8.1”. In: *Comput. Phys. Commun.* 178 (2008), p. 852. DOI: `10.1016/j.cpc.2008.01.036`. arXiv: `0710.3820`.

[37] D. J. Lange. “The EvtGen particle decay simulation package”. In: *Nucl. Instr. Meth. A* 462 (2001), p. 152. DOI: `10.1016/S0168-9002(01)00089-4`.

[38] P. Skands, S. Carrazza, and J. Rojo. “Tuning PYTHIA 8.1: the Monash 2013 Tune”. In: *Eur. Phys. J. C* 74 (2014), p. 1. DOI: `10.1140/epjc/s10052-014-3024-y`. arXiv: `1404.5630`.

[39] Torbjörn Sjöstrand et al. “An introduction to PYTHIA 8.2”. In: *Comput. Phys. Commun.* 191 (2015), p. 159. DOI: `10.1016/j.cpc.2015.01.024`. arXiv: `1410.3012 [hep-ph]`.

[40] *Luminosity determination in pp collisions at $\sqrt{s}$ = 13 TeV using the ATLAS detector at the LHC*. Tech. rep. All figures including auxiliary figures are available at https://atlas.web.cern.ch/Atlas/GROUPS/PHYSICS/CONFNOTES/ATLAS-CONF-2019-021. Geneva: CERN, June 2019. URL: `https://cds.cern.ch/record/2677054`.

[41] Joao Pequenao and Paul Schaffner. “How ATLAS detects particles: diagram of particle paths in the detector”. Jan. 2013. URL: `https://cds.cern.ch/record/1505342`.

[42] ATLAS Collaboration. “Performance of the ATLAS track reconstruction algorithms in dense environments in LHC Run 2”. In: *Eur. Phys. J. C* 77 (2017), p. 673. DOI: `10.1140/epjc/s10052-017-5225-7`. arXiv: `1704.07983 [hep-ex]`.

[43] R. Frühwirth. “Application of Kalman filtering to track and vertex fitting”. In: *Nuclear Instruments and Methods in Physics Research Section A: Accelerators, Spectrometers, Detectors and Associated Equipment* 262.2 (1987), pp. 444–450. ISSN: 0168-9002. DOI: `https://doi.org/10.1016/0168-9002(87)90887-4`. URL: `https://www.sciencedirect.com/science/article/pii/0168900287908874`.

[44] F. Meloni. “Primary vertex reconstruction with the ATLAS detector”. In: *Journal of Instrumentation* 11.12 (Dec. 2016), pp. C12060–C12060. DOI: `10.1088/1748-0221/11/12/c12060`. URL: `https://doi.org/10.1088/1748-0221/11/12/c12060`.

[45] Matteo Cacciari, Gavin P. Salam, and Gregory Soyez. “The anti-k_t jet clustering algorithm”. In: *JHEP* 04 (2008), p. 063. DOI: `10.1088/1126-6708/2008/04/063`. arXiv: `0802.1189 [hep-ph]`.

[46] ATLAS Collaboration. “Jet energy measurement with the ATLAS detector in proton–proton collisions at $\sqrt{s} = 7$ TeV”. In: *Eur. Phys. J. C* 73 (2013), p. 2304. DOI: `10.1140/epjc/s10052-013-2304-2`. arXiv: `1112.6426 [hep-ex]`.

[47] ATLAS Collaboration. “Jet energy scale and resolution measured in proton–proton collisions at $\sqrt{s} = 13$ TeV with the ATLAS detector”. In: (2020). arXiv: `2007.02645 [hep-ex]`.

[48] ATLAS Collaboration. “Muon reconstruction and identification efficiency in ATLAS using the full Run 2 *pp* collision data set at $\sqrt{s} = 13$ TeV”. In: (2020). arXiv: `2012.00578 [hep-ex]`.

[49] ATLAS Collaboration. “Muon reconstruction performance of the ATLAS detector in proton–proton collision data at $\sqrt{s} = 13\,\text{TeV}$”. In: *Eur. Phys. J. C* 76 (2016), p. 292. DOI: 10.1140/epjc/s10052-016-4120-y. arXiv: 1603.05598 [hep-ex].

[50] ATLAS Collaboration. “Standalone vertex finding in the ATLAS muon spectrometer”. In: *JINST* 9 (2014), P02001. DOI: 10.1088/1748-0221/9/02/P02001. arXiv: 1311.7070.

[51] *Tagging and suppression of pileup jets with the ATLAS detector*. Tech. rep. Geneva: CERN, May 2014. URL: https://cds.cern.ch/record/1700870.

[52] Belle Collaboration. “A detailed test of the CsI(Tl) calorimeter for BELLE with photon beams of energy between 20-MeV and 5.4-GeV”. In: *Nucl. Instrum. Meth* A441 (2000), pp. 401–426. DOI: 10.1016/S0168-9002(99)00992-4.

[53] Alexander L. Read. “Presentation of search results: The CL(s) technique”. In: *J. Phys. G* 28 (2002), p. 2693. DOI: 10.1088/0954-3899/28/10/313.

[54] Alexander L. Read. “Modified frequentist analysis of search results (The CL(s) method)”. In: *Workshop on Confidence Limits*. Aug. 2000, pp. 81–101.

[55] Lukas Heinrich, Matthew Feickert, and Giordon Stark. *pyhf: v0.6.2*. Version 0.6.2. https://github.com/scikit-hep/pyhf/releases/tag/v0.6.2. DOI: 10.5281/zenodo.1169739. URL: https://doi.org/10.5281/zenodo.1169739.

[56] Lukas Heinrich et al. “pyhf: pure-Python implementation of HistFactory statistical models”. In: *Journal of Open Source Software* 6.58 (2021), p. 2823. DOI: 10.21105/joss.02823. URL: https://doi.org/10.21105/joss.02823.

[57] Glen Cowan et al. “Asymptotic formulae for likelihood-based tests of new physics”. In: *Eur. Phys. J. C* 71 (2011), p. 1554. DOI: 10.1140/epjc/s10052-011-1554-0,10.1140/epjc/s10052-013-2501-z. arXiv: 1007.1727.

[58] Working Group 2 on the Physics of the HL-LHC, and Perspectives at the HE-LHC. “Higgs Physics at the HL-LHC and HE-LHC”. In: (2019). arXiv: 1902.00134.

[59] Yanou Cui and Brian Shuve. “Probing Baryogenesis with Displaced Vertices at the LHC”. In: *J. High Energy Phys.* 02 (2015), p. 049. DOI: 10.1007/J.HighEnergyPhys.02(2015)049. arXiv: 1409.6729.

[60] K. Cranmer and I. Yavin. *RECAST: Extending the Impact of Existing Analyses*. 2010. arXiv: 1901.04468. URL: https://dx.doi.org/10.1007/JHEP04(2011)038.

[61] P. Mermod. *Right-handed neutrinos: the hunt is on!* 2017. arXiv: 1704.08635 [hep-ex].

[62] Cristiano Alpigiani et al. *An Update to the Letter of Intent for MATHUSLA: Search for Long-Lived Particles at the HL-LHC*. 2020. arXiv: 2009.01693 [physics.ins-det].

[63] SHiP Collaboration. *A facility to Search for Hidden Particles (SHiP) at the CERN SPS*. 2015. arXiv: 1504.04956 [physics.ins-det].

[64] Vladimir V. Gligorov et al. “Searching for long-lived particles: A compact detector for exotics at LHCb”. In: *Physical Review D* 97.1 (Jan. 2018). ISSN: 2470-0029. DOI: 10.1103/physrevd.97.015023. URL: http://dx.doi.org/10.1103/PhysRevD.97.015023.

[65] Vladimir V. Gligorov et al. "Leveraging the ALICE/L3 cavern for long-lived particle searches". In: *Physical Review D* 99.1 (Jan. 2019). ISSN: 2470-0029. DOI: 10.1103/physrevd.99.015023. URL: http://dx.doi.org/10.1103/PhysRevD.99.015023.

[66] Martin Bauer et al. *ANUBIS: Proposal to search for long-lived neutral particles in CERN service shafts*. 2019. arXiv: 1909.13022 [physics.ins-det].

[67] Andrew Haas et al. "Looking for milli-charged particles with a new experiment at the LHC". In: *Physics Letters B* 746 (June 2015), pp. 117–120. ISSN: 0370-2693. DOI: 10.1016/j.physletb.2015.04.062. URL: http://dx.doi.org/10.1016/j.physletb.2015.04.062.

[68] FASER Collaboration. *FASER: ForwArd Search ExpeRiment at the LHC*. 2019. arXiv: 1901.04468 [hep-ex].

[69] John Paul Chou, David Curtin, and H.J. Lubatti. "New detectors to explore the lifetime frontier". In: *Physics Letters B* 767 (Apr. 2017), pp. 29–36. ISSN: 0370-2693. DOI: 10.1016/j.physletb.2017.01.043. URL: http://dx.doi.org/10.1016/j.physletb.2017.01.043.

[70] Cristiano Alpigiani et al. *An Update to the Letter of Intent for MATHUSLA: Search for Long-Lived Particles at the HL-LHC*. 2020. arXiv: 2009.01693 [physics.ins-det].

[71] Maf Alidra et al. "The MATHUSLA test stand". In: *Nuclear Instruments and Methods in Physics Research Section A: Accelerators, Spectrometers, Detectors and Associated Equipment* 985 (Jan. 2021), p. 164661. ISSN: 0168-9002. DOI: 10.1016/j.nima.2020.164661. URL: http://dx.doi.org/10.1016/j.nima.2020.164661.

[72] Cristiano Alpigiani et al. *A Letter of Intent for MATHUSLA: a dedicated displaced vertex detector above ATLAS or CMS*. 2018. arXiv: 1811.00927 [physics.ins-det].

[73] David et al. Curtin. "Long-lived particles at the energy frontier: the MATHUSLA physics case". In: *Reports on Progress in Physics* 82.11 (Oct. 2019), p. 116201. ISSN: 1361-6633. DOI: 10.1088/1361-6633/ab28d6. URL: http://dx.doi.org/10.1088/1361-6633/ab28d6.